ALMA MATER STUDIORUM
UNIVERSITA' DI BOLOGNA

Dipartimento di Fisica e Astronomia

Dottorato di ricerca in Astrofisica Ciclo XXX

Tesi di Dottorato

MAORY: wavefront sensor prototype and instrument optical design

Settore Concorsuale di afferenza: 02/C1 – Astronomia, Astrofisica, Fisica della Terra e dei Pianeti

Settore Scientifico disciplinare: FIS/05 – Astronomia e Astrofisica

Candidato

Mauro Patti

Coordinatore Dottorato

Francesco R. Ferraro

Supervisore

Emiliano Diolaiti

Co-Supervisore

Matteo Lombini

Esame finale anno 2018

Abstract

MAORY will be the multi-conjugate adaptive optics module for the ELT first light. Its main goal is to feed the high-resolution NIR imager and spectrograph MICADO.

The present Thesis address the MAORY system at the level of optical design and analysis.

MAORY is a complex science projects whose stakeholder is the scientific community. Its requirements are driven by the science cases which request high resolution and astrometric accuracy.

In an ideal world without atmospheric turbulence, MAORY optics must deliver diffraction-limited images with very low optical distortions.

The tolerance process is one of the most important step in the instrument design since it is intended to ensure that MAORY requested performances are satisfied when the final assembled instrument is operative.

The baseline is to operate wavefront sensing using six sodium Laser Guide Stars and three Natural Guide Stars to solve intrinsic limitations of artificial sources and to mitigate the impact of the sodium layer structure and variability.

The implementation of a laboratory Prototype for Laser Guide Star wavefront sensor at the beginning of the phase study of MAORY has been indispensable to consolidate the choice of the baseline of wavefront sensing technique.

The first part of this Thesis describes the results obtained with the Prototype for Laser Guide Star wavefront sensor under different working conditions.

The second part describes the logic behind the tolerance analysis at the level of MAORY optical design starting from definition of quantitative figures of merit for requirements and ending with estimation of MAORY performances perturbed by opto-mechanical tolerances.

The sensitivity analysis on opto-mechanical tolerance of MAORY is also a crucial step to plan the alignment concept that concludes the arguments addressed by this Thesis.

Contents

Definitions, Acronyms and Abbreviations

AIV Assembly, Integration and Verification
AS Aperture Stop
ELT Extremely Large Telescope
ESO European Southern Observatory
DOF Degree Of Freedom
FoV Field of View
GS Guide Star
HO High Order
LGS Laser Guide Star
LO Low orders
LOR low-order & reference
MAORY Multi conjugate Adaptive Optics RelaY
MCAO Multi-Conjugate Adaptive Optics
MICADO MCAO Imaging Camera for Deep Observations
NCPA Non-Common-Path Aberrations
NGS Natural Guide Star
OPD Optical Path Difference
PS Phase Screen
PSD Power Spectral Density
PSF point spread function
PFR Post Focal Relay
RMS Root Mean Square
RON Read Out Noise
RSS Root Sum Squared
SCAO Single-Conjugate Adaptive Optics
SH Shack-Hartmann
SLM Spatial Light Modulator
SNR Signal-to-Noise Ratio
SVD Singular Value Decomposition
TBD To Be Defined
TBC To Be Confirmed
TS Turbulence Simulator
TT Tip-Tilt
TTF Tip-Tilt and Focus
WF Wavefront
WFE Wavefront Error
WFS Wavefront Sensor

1. Background

Atmospheric turbulence has been, for centuries, the limit of any ground based optical/IR instrument. Turbulent mixing of air (lead by large scale temperature fluctuations) generates spatial and temporal variations in the atmosphere refractive index [1].

One of the model to explain how WF aberration are generated by turbulence was proposed by Kolmogorov [2]. This and many other models [3] [4] are based on statistic approach and describe the distribution of the strength of refractive index variations through atmospheric turbulence as a function of height z. This structure function is known as $C^2_n(z)$ profile and models the atmosphere as a superposition of thin turbulent layers at variable height with different strength [5].

Three are the main parameters that characterize atmospheric turbulence and directly drive the design and performance of AO systems:

- The **Fried parameter**, $r_0 \propto [\lambda^{-2} (\cos \gamma)^{-1} \int C^2_n(z)\, dz]^{-3/5}$, gives the aperture over which there is on average one radian of RMS phase aberration. It could be considered as the spatial scale at which an AO system needs to sample its correction [6].
- The **isoplanatic angle**, $\theta_0 \propto (\cos \gamma)\, r_0/h$, were h is the height of a turbulence. Isoplanatism describes the angular dependence of optical path variations that deviate by less than one radian RMS phase aberration from each other at the isoplanatic angle.
- The **coherence time**, $\tau_0 \propto r_0/v$, where v is the average wind speed, describes the time scale at which optical path variations deviate by less than one radian RMS phase aberration from each other. τ_0 defines the required AO temporal correction bandwidth.

The most basic AO systems is made by one WFS, one DM and a RTC [7]. The AO system tries to correct WF aberrations by measuring the optical path deviations using the WFS. The RTC calculates an appropriate correction, and applies this correction to the DM. This feedback loop runs on frequencies of hundred times a second depending on the requirement set by τ_0. The WF sampling carried out by the WFS and the spatial scale at which the DM applies its correction are set by r_0.

The WFS is an optical device designed to be sensitive to the WF phase and generally works with a high efficiency photon detector (e.g. Charge-Coupled Device or Avalanche Photo Diode).

Three types of WFSs are the most used in AO depending on the performances the system has to achieve in terms of dynamic range and sensitivity. These three class of WFSs are:

- The **Shack-Hartmann WFS** [8] is made by an array of lenslets which define an array of sub-apertures across the pupil and produce an array of spots corresponding to the local WF. The positions of these spots respect to the sub-aperture centre are strictly related to the average WF slope or gradient over the sub-aperture.
- The **Pyramid WFS** [9] is made by a pyramid prism whose tip is placed on a focal plane. A collimator, after the pyramid, generates multiple pupil images. When an aberrated ray hits the prism on either side of its tip, it appears in only one of the multiple pupils. The intensity distributions in the multiple pupil images are a measure for the WF phase (Verinaud et al. 2005). The pyramid prism is often modulated such that a single ray appears in either of the pupil images. The intensity distribution of the pupil images, integrated over a modulation period, is a direct measure of WF slopes in the pupil. The sensitivity of this WFS depends on the modulation amplitude and can be tuned depending on the observing conditions.
- The **curvature WFS** [10] is made by an oscillating membrane in the focal plane. It measures intensity distributions in two different planes on either side of the focus, corresponding to the wavefront's curvature or 2nd derivative (Roddier 1988).

The main role of the RTC is the WF reconstruction from WFS measurements. In practise, RTC deals with the WFS measurement vector v (e.g. all the slopes measured by a Shack-Hartmann sensor) and calculates an appropriate correction vector c in terms of voltages to send to the DM.

The WFS approximately works in linear regime, hence WF reconstruction performed by the RTC can be described by the linear system:

$$Dc = v + n$$

where n is the measurement noise usually assumed to be Gaussian and uncorrelated, and D is the interaction matrix between DM and WFS.

In order to solve for *c*, the RTC derives a reconstruction matrix *R* and multiply it with *v*. Basically, *R* is the Moore-Penrose pseudoinverse of *D*, since *D* is usually degenerate and not directly invertible [5] [11].

The DM is made by an array of actuators which are connected to a thin optical surface that deforms under the expansion of the actuators. Distance between two consecutive actuators is a requirement lead by r_0 while, the number of actuators and hence, the DM diameter depends on the conjugation altitude and the telescope aperture diameter.

Any AO system needs at least a single GS to correct the WF in its direction. Such a setup is known as SCAO and achieved excellent performances on different instruments over the last years [12] [13] [14].

The limit of SCAO is the isoplanatic angle, this implies that the instrument PSF is not uniform across the FoV and it is close to the diffraction limit only at GS position.

AO wavefront sensing requires GSs bright enough to reach a good SNR for the WFS measures [1]. In many cases, a bright NGS is not available in the FoV. The probability to find suitable NGS is called sky coverage and it strongly depends on the observational wavelength. For instance, on 8-10 meters class telescopes, NGS with magnitude $M_v = 14$ is required to compensate images at 2,2µm wavelength [15].

In this context the potential power of LGS AO, proposed by Foy & Labeyrie [16], is clear. The LGSs are introduced in Section 3 along with the issues related to these artificial sources that has been object of study in Section 4 of this Thesis.

The concept behind the use of LGS is to increase the size of the corrected area by using several GSs to measure the turbulence in the complete 3D volume above the telescope. This field adapted correction, accounting for the field dependence nature of the atmospheric turbulence, is called MCAO [17]. It is a concept that consists in using several DM conjugated in altitude to tune the correction depending on the location in the field.

Of course, one also needs measurements of the turbulence volume. This is obtained by using various WFSs pointing at different field positions, either at NGSs, or at LGSs.

The multiple reference sources are in different directions so that the columns of atmospheric turbulence they probe overlap partially at high altitude and fully at low altitude. Separate DMs, conjugated at specific heights, apply the correction as the sensed turbulence is fully projected on the conjugated layer. In practice, the correction given to each DM has to

minimise the uncorrected turbulence, both along the atmosphere altitude and in the scientific FoV.

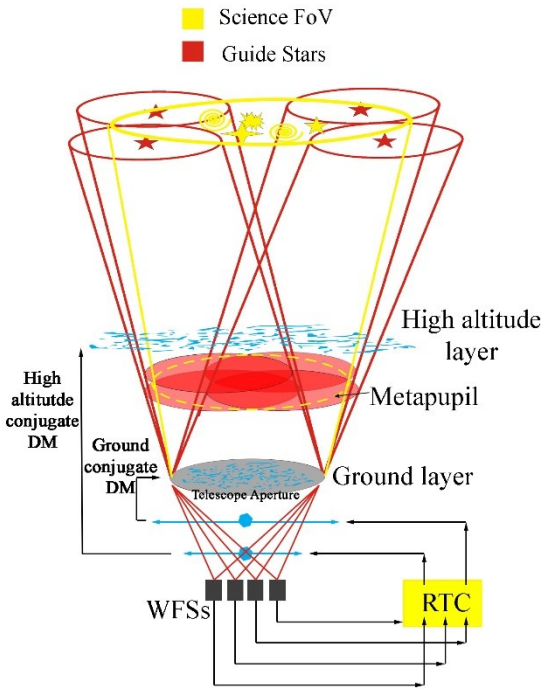

Figure 1 : The MCAO concept. The metapupil is the DM projected diameter to a certain altitude.

The wavefront reconstruction and MCAO control is a complex issue. MCAO correction computation is basically a two-step process:

1. a tomographic reconstruction giving an estimation of the turbulent phase in the volume from multi-channel WFS data. This estimation part depends on GS characteristics (e.g. geometry, flux) and it uses priors on turbulence statistics and its distribution in altitude.
2. a projection of the estimated phase (in the atmospheric volume) onto the DM subspace, accounting for DM characteristics (e.g. number/pitch/altitude). The projection is optimized on a specific FoV.

To improve sky-coverage, sodium LGS constellations are used to measure high orders, with HO WFSs. But since LGSs do not measure tip-tilt, and potentially have difficulties giving an absolute defocus because of sodium profile fluctuations (See Section 3), one also makes use of few NGS to estimate low orders, with LO WFSs.

2. MAORY. The Multi-conjugate Adaptive Optics RelaY for ELT

MAORY [18] is the MCAO post-focal module of the ELT [19].

The ELT will use a novel design with a total of five mirrors. The first three aspheric mirrors (M1, M2, M3) form a TMA design [20] for diffraction-limit image quality over the 10 arcminute FoV. The diameter of the segmented primary mirror is approximately 39 metres. The fourth and fifth mirrors (M4, M5) provide AO correction for atmospheric aberrations (M4), and tip-tilt correction for image stabilisation (M5) [21]. These two mirrors can reflect the light toward two Nasmyth platforms at either side of the rotatable telescope

MAORY is designed and built by a Consortium including INAF (Italy) and INSU IPAG (France). ESO is the customer and is also actively involved in the project. It supports the MICADO near-infrared camera by offering two adaptive optics modes: MCAO and SCAO. MAORY and MICADO [22] are placed on the Nasmyth platform A.

MICADO, in imaging, will have two options for the plate/pixel scale: one with ~1.5 mas/px and FoV diameter ~ 20arcsec, and one with ~3-4 mas/px and full 53" x 53" FoV. It will be equipped with a large set of broad (I, Z, Y, J, H, K) and narrow band filters. MICADO will also have a coronographic mode and it will allow long-slit spectroscopy (slit orientation along the parallactic angle) with spectral resolution R ~ 4000 - 8000.

The MCAO mode is based on up to six LGSs and three NGSs for WF sensing. In particular, HO WF sensing is performed by using LGSs while LO WF sensing is performed by using NGSs to measure the modes which cannot be accurately sensed by the LGSs. The six LGSs are produced by excitation of the atmospheric sodium with six laser beacons propagated from the edges of ELT pupil. The laser beacons work at wavelength of 589.2 nm and excite the sodium layer by optical pumping of the mesospheric sodium atoms.

At first light, MAORY will contain a single DM with provision for a second DM as an upgrade.

In the MCAO mode, at least one DM within MAORY works together with the telescope M4 while M5 is used to perform only the TT wavefront correction.

The two or more DMs are conjugated to different altitudes to provide a wide FoV with high Strehl ratio and uniformity of the PSF.

The current baseline optical design of MAORY is based on six mirrors (including one or two DMs) and a dichroic beam-splitter. This dichroic beam-splitter is used to split the science

light from the LGS light that is transmitted to the LGS WFSs by means of a focusable objective [5]. MAORY optics are optimized for the spectral band between 0.8 µm and 2.4 µm and the current optical design is shown in Figure 25.

In MCAO mode, MAORY is required to provide an unvignetted corrected field of diameter D ≈ 75 arcsec for MICADO and an unvignetted field of diameter D ≤ 200 arcsec for the second instrument. The AO correction will be performed over the whole D ≤ 200 arcsec FoV, although the performance is expected to decrease at the edge of the field.

The NGS patrol field may be approximately depicted as the annulus enclosed between D ≈ 75 arcsec and D ≤ 200 arcsec.

The size of outer diameter of NGS patrol field is currently under study and will depend by the sky coverage.

Within this patrol field, three probes (small movable pick-off mirrors) will pick the light from three suitable NGSs to perform LO WF sensing in MCAO mode. In principle MAORY can work with less than three NGSs, with lower performances.

The post focal DMs optical conjugates, inside MAORY, are planned to be at 4km and 15.5km altitude. The LGSs are used for HO wavefront sensing and they are projected from the telescope side on a circle not greater than 2 arcmin angular diameter. The dichroic beam-splitter response curve may be a low-pass filter, with cut-off at about 600 nm, or a notch filter centred at the LGS wavelength. The light reflected by the beam-splitter propagates through the last segment of the main path optics (science path) to the exit port. At the exit port, the MAORY exit focal plane is delivered to MICADO through the so-called Green Doughnut [23].

The Green Doughnut is the interface between MICADO cryostat and MAORY exit focal plane. It's a cylinder of 800 mm high and 2.6 m in diameter and hosts the SCAO and MCAO subsystems that works with NGSs.

The light picked up by the NGS probes will be split by a dichroic into two beams:

- Beam with wavelengths approximately spanning the R and I bands
- Beam with wavelengths approximately spanning the H band

Each beam feeds an independent set of WFSs:

- Three NGS WFS approximately spanning the R and I bands
- Three NGS WFS approximately spanning the H band

These two WFS channels will take care of different components of the low order aberrations. NGS WFSs, working in the H band, are used for fast TT and focus corrections with frequencies ~500Hz while the so called LOR WFSs, working in the R and I bands, operate at frequencies in the range 0.1-1 Hz and monitor the LGS NCPA not sensed by the LGS WFS and discussed in the next Chapter.

A single NGS wavefront sensor is deployed in the SCAO mode where wavefront aberrations are compensated by the telescope M4 and M5 mirrors. In this case, the DMs inside MAORY are kept at their reference shape. The SCAO mode is expected to provide a better AO correction than MCAO in a small FoV ($D \approx 10$ arcsec) surrounding a bright star that will serve as a single NGS. AO simulations shown that NGS at magnitude $M_V \leq 12$ allow to obtain an on-axis Strehl Ratio > 0.6 at $\lambda = 2.2$ μm [24].

MAORY also offers provision for a second port for a future instrument which is still undefined.

The instrument project entered its phase B in February 2016 and, at the time of writing, the trade-off studies, in preparation to the last phase of the preliminary system requirement review, are approaching the end of the analysis.

The opto-mechanical design of MAORY has to take care of the tolerance budget described in Section 6.7. The design will be consolidated through an iterative process that will also consider the thermoelastic model and a defined assembly/alignment procedure. A sketch of MAORY-MICADO on the Nasmyth platform is shown in Figure 3.

The MAORY product tree is shown in Figure 2. The instrument is divided into two main parts:

1. **Instrument**. It is the principal system divided into other sub-systems permanently installed on the Nasmyth platform. It is composed by opto-mechanical components, software and electronics.
2. **Auxiliary equipment**. It is composed by tools used during the AIT phase and instrument transport.

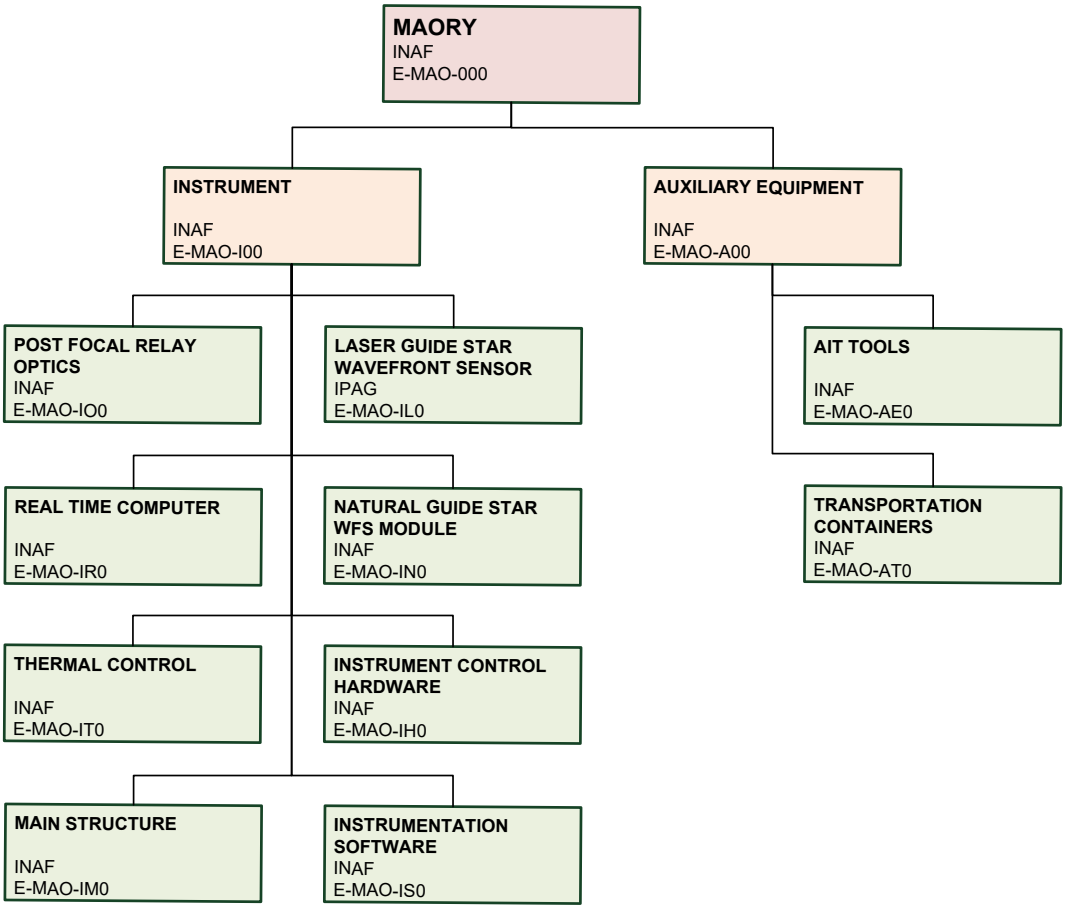

Figure 2 : MAORY product tree

The Post-Focal Relay Optics product in the system-level product tree (Figure 2) is further split into two main sub-products:

- **Main Path Optics**, which relay the telescope focal plane to the science instrument(s) fed by MAORY;
- **LGS Objective**, which creates an image of the LGSs, which are used by the MAORY MCAO system for high-order wavefront sensing.

These two sub-products are addressed in this Thesis at the level of optical design and analysis.

The Main Path Optics also include one or two post-focal DMs, which are regarded in the studies of this Thesis as plain rigid mirrors. The full design and analysis report of these mirrors is beyond the scope of the Thesis.

The PFR Optics product in the system-level product tree also include the optics mounts and their interfaces to the MAORY Bench. The design and analysis report of these components is beyond the scope of the Thesis.

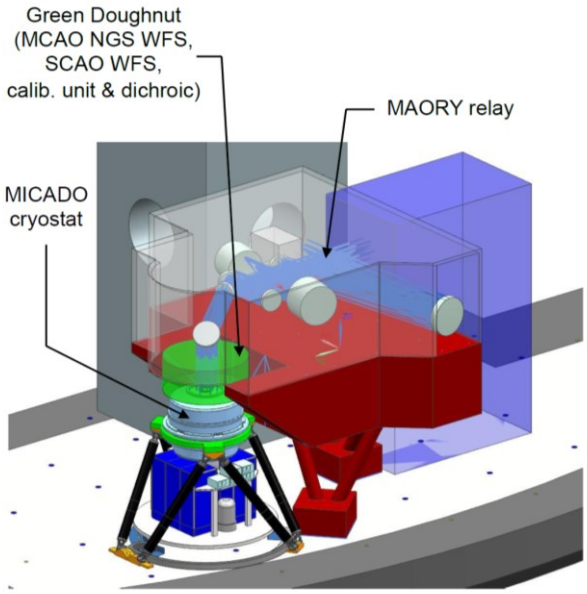

Figure 3: Concept of MAORY-MICADO mechanical structure on the Nasmyth platform

2.1 Scientific performance requirements

In MCAO mode, MAORY will have to provide Strehl Ratio SR ≥ 0.3 at λ = 2.2 µm under median atmospheric conditions. This requirement is intended as average value over the MICADO field for observations close to zenith. The requirement has to be achieved over at least 50% of the observable sky at the telescope. The performance goal is SR = 0.5 at λ = 2.2 µm: this performance level may be achievable with a second deformable mirror inside MAORY.

Relative astrometric accuracy is one of the science drivers of the MCAO mode. MAORY will have to permit observations with MICADO such that the relative position on the sky of an unresolved, unconfused source of optimal brightness w.r.t. an optimal set of reference sources is reproducible to within 50 µas (goal 10 µas) over a central field of 20 arcsec diameter (across the entire MICADO field as a goal) over timescales in the range of 1 hour to 5 years.

Concerning relative photometric accuracy, MAORY will have to permit observations with MICADO such that the relative flux of an unresolved, unconfused source of optimal brightness w.r.t an optimal set of reference sources is reproducible to within 0.02 mag (goal: 0.01 mag) across the MICADO field of view over timescales in the range of 1 hour to 5 years.

3. LGS WF sensing in the ELT era

Wavefront sensing assisted by LGSs is considered essential for the AO systems of future ELTs to achieve the required performance with high sky coverage.

The fraction of the sky where an efficient AO correction can be achieved is limited by two requirements:

1. GS within the isoplanatic angle of the science target
2. GS bright enough to provide a sufficient SNR for the WFS

In this context, the concept of LGS [16] is a solution to the lack of sky coverage. The use of LGSs, in principle, could substitute bright NGSs, but other difficulties arise. These are linked to the finite distance of LGS from the telescope, its vertical extension and lower atmosphere effects in the upward path of the laser beam.

Roughly speaking, LGS are artificial sources created by the back-scattering of laser light by sodium atoms in the high mesosphere or by molecules and atoms located in the low stratosphere. In the first case, the laser wavelength is tuned to one of the sodium D spectral line and able to excite the sodium layer in the atmosphere at an altitude of about 90km. Sodium atoms are pumped from the ground state into an excited state from which their natural decay produces the desired back-scattered radiation. The second case, the Rayleigh scattering, exploits the elastic scatter of the particles and depends on the atmospheric density which drastically drops with altitude. Rayleigh beacons are less efficient to sample the atmospheric turbulence because they suffer most of the so-called cone-effect, especially for large telescope as ELT. That's the main reason why the AO correction provided by MAORY LGS WFS is based sodium laser beacon.

The mesosphere contains a build-up of neutral sodium atoms located at a mean height of 90 km (see Figure 5). An ideal LGS should be a point source, but the depth of the sodium layer and its density variability forms an oblate three-dimensional scattering volume with slow variable shape when excited by the laser.

TT are the two lowest order wavefront distortion components which cause the overall image motion in single-aperture AO. To stabilize an image, it is necessary to use a separate reference source that is not twice perturbed by the atmosphere as the LGS case. If the laser is projected and viewed by the full telescope aperture, its motions due to atmospheric turbulence on the upward beam, is added to the same effect resulting in the downward beam. This is valid assuming the wavefront does not change within the propagation time and the result is no

overall tilt error is detected by a WFS using the same aperture. Besides, as shown in Figure 4, the TT contributions of the upward laser beam and its downward cone are not separable since the latter samples a wider atmospheric area [25].

The current solution to overcome this problem consists in using an additional NGS for TT compensation whose requested magnitude is much higher respect to the pure NGS WF sensing case. For only TT measures, the pupil image can be considered like a SHWFS with only one sub-aperture equal to the telescope aperture increasing the detectable number of photons and thus, the sky coverage.

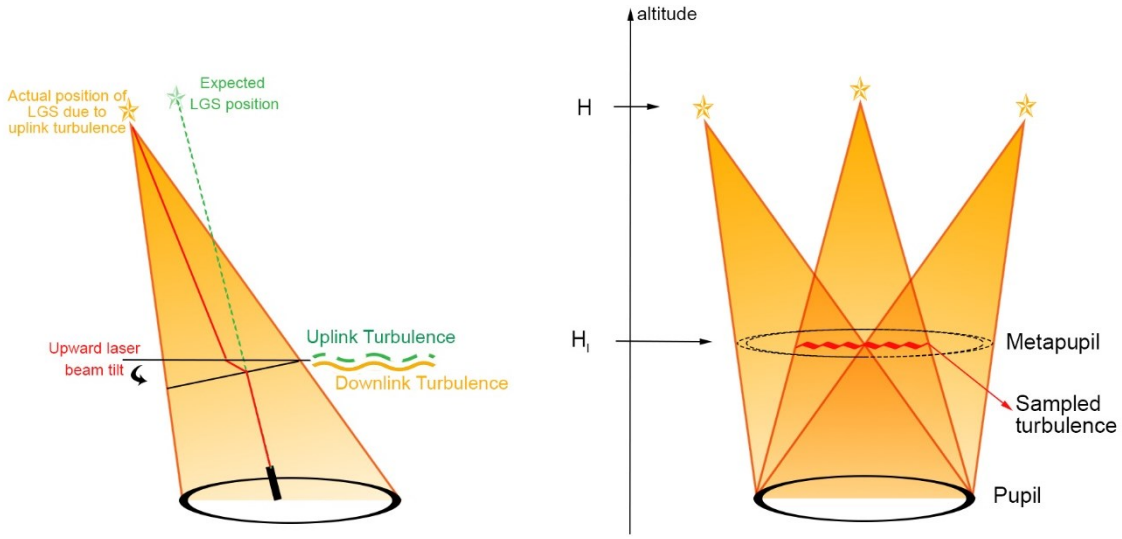

Figure 4: (Left) Tip-tilt indetermination: when the laser is launched behind the secondary obstruction (or at the side of the primary mirror). The Tip-tilt contributions from the LGS actual position and the atmospheric turbulence cannot be disentangled. (Right) cone effect and MCAO solution to the angular anisoplanatism. At the altitude H_l several LGSs achieve a better coverage of the metapupil, the region at a given altitude inside the scientific FoV.

A LGS is at finite altitude and its light return samples a cone-shaped volume of the turbulence instead of a cylindric-shaped volume of a source at infinity. For the same reason, the telescope aperture receives a spherical wavefront instead of flat. The laser spot is formed at some finite altitude H above the telescope and a turbulent layer at altitude H_l is sampled differently by the laser and stellar beams. Besides, the turbulence above H is not sensed by the LGS.

The footprint diameter D_f for a telescope pupil D is:

$$D_f = D\,(1-H_l/H)$$

and the differential extension in the overlap between the LGS and scientific FoV implies that part of the turbulence volume is not sensed.

The best solution for the cone effect leads to the AO configuration with multiple LGSs.

To describe this concept, a metapupil has to be consider as the DM projected diameters:

$$d = D + 2\beta H_l \qquad (\beta \text{ is the angular radius of the FoV})$$

The beams from scientific objects and guide stars do not sample the whole metapupil, but have smaller footprints. Considering the cone effect, at a defined layer of altitude H_l, the reconstruction of the turbulence requires more LGSs to sample the same metapupil area respect to the NGS case (Figure 4). It is possible to achieve the same NGS sampling only in the areas where two or more conical beams intersect each other. But, in practice, the WFS measures coming from the LGSs are averaged over the metapupil.

The depth of the sodium layer can vary from 5-20 km depending on location, season, and even time of day [26]. While the origins of sodium atom buildup in the mesosphere is unknown, it has been hypothesized that it was formed from the ablation of meteors [27]. Various groups interested in atmospheric physics have studied this layer, revealing that it is variable in structure and thickness, and occasionally exhibits a multi-modal density in height [28]. (See Figure 5)

This spurious defocus term, due to sodium mean altitude fluctuation, propagates through the AO loop introducing an RMS WFE:

$$\sigma_{def}^2 = \frac{1}{16\sqrt{3}} \frac{D^2}{H^2} \Delta H$$

With D telescope diameter and H altitude of sodium layer. Even if this term is induced at a much lower temporal frequency than the atmospheric turbulence defocus, its dependence with the square of the telescope diameter makes critical the possibility to separate the two (e.g. for the ELT). Again, the use of NGS to measure defocus errors, in addition to TT motions, is therefore necessary in the AO systems. For MAORY the reference WFS that will measure the first tens modes of the wavefront, will use the visible light of three NGSs whose near infrared light is instead used to measure the TT and defocus terms (as described in the previous Section).

During the observation, the sky tracking changes the telescope zenith angle γ increasing or decreasing the sodium layer mean distance to the aperture by a factor cos γ. This effect leads

the focal plane of the LGS to move with time and thus, the AO design must provide the use of a stage that carries the WFS to follow the image position.

3.1 LGS WFS Concept

On the ELT, six sodium LGSs are planned. These are generated by projecting powerful laser beams (589 nm wavelength) from the edge of the telescope aperture up to the natural sodium layer in the mesosphere at about 90 km height. The return light samples the turbulent atmosphere and is collected by a set of WFSs, which measure in real-time the wavefront perturbations due to the atmospheric turbulence.

MAORY contains a PFR, which creates an image of the telescope focal plane (entrance optical interface of MAORY) for the science instrument located on the MAORY exit port. The LGS light is propagated through this relay up to a dichroic beam-splitter, which is located after the deformable mirrors in order to let the LGS WFSs operate in close loop regime. The dichroic lets the light of 6 LGSs, arranged on a circle of about 90" diameter, pass through and reflects science beam and NGS light. Behind the dichroic an objective creates the LGS image plane for the WFSs channel. The LGS WFS will be based on the SH WFS concept.

The current choice of the LGS WFS FoV is 15 arcsec. The detector size is 800x800 pixels, the pixel size is 24µm, the number of sub-apertures is 80x80, the number of pixels per sub-aperture is 10x10 and the ELT sub-aperture size is 0.482m. The choice of LGS WFS FoV greater than 10 arcsec has been done to avoid a large spot truncation (see Section 3.2). This technical requirement implies the need of sub-sampling the LGS image and so to foresee some calibrations to recover a good spot resolution for slope measurement. This is an aspect that has been investigated through a laboratory experiment and discussed in Section 4.

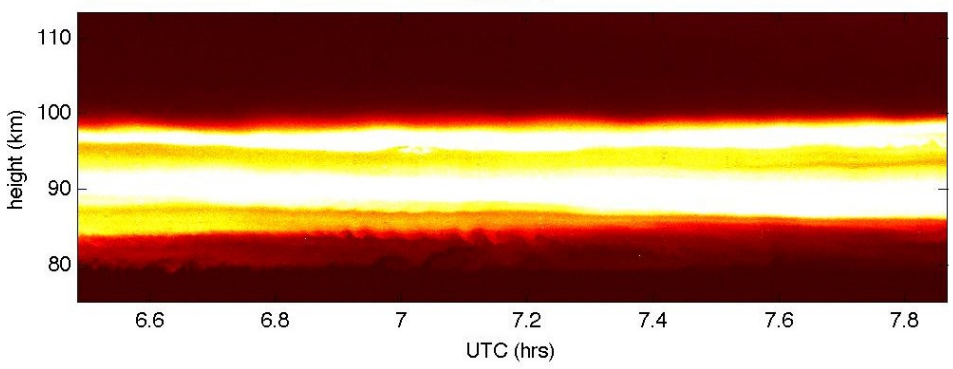

Figure 5: Sodium layer density profile in function of time. (credit: Paul Hickson, Department of Physics and Astronomy, University of British Columbia.)

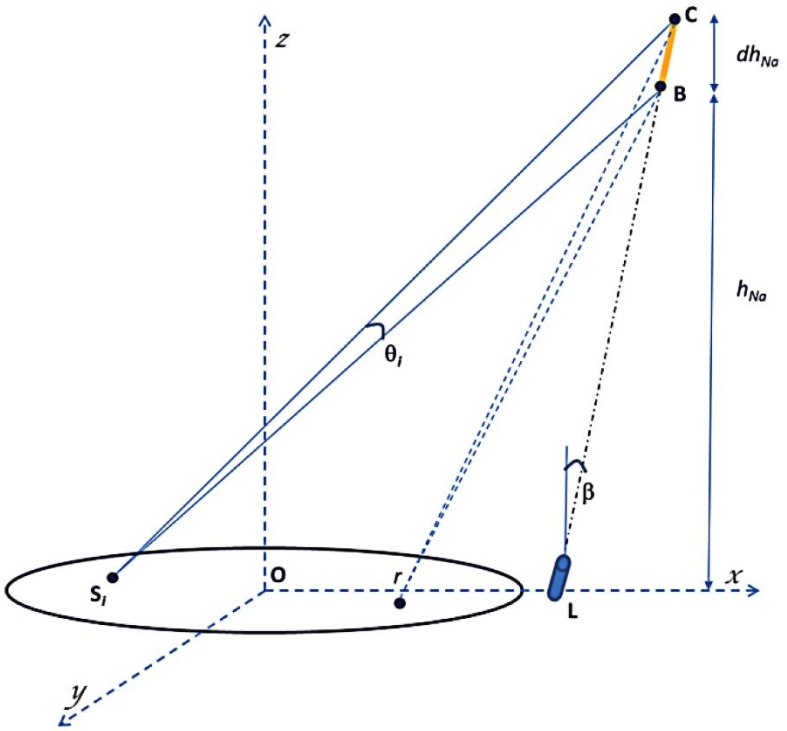

Figure 6 : Geometrical representation of the LGS view from the LGS SH sub-apertures.

.

In Figure 6, **O** is the origin of the *xyz* reference frame and it is located in the centre of the telescope pupil having diameter = $2r$. **B** and **C** define the extremities of the LGS region of interest (e.g sodium density profile FWHM when a single Gaussian density profile is considered) and have coordinates in the *xyz* space respectively:

$$\mathbf{B} = [h_{Na} \cdot \tan \beta_x + X_{LT} \; ; \; h_{Na} \cdot \tan \beta_y + Y_{LT} \; ; \; h_{Na}];$$

$$\mathbf{C} = [(h_{Na} + dh_{Na}) \cdot \tan \beta_x + X_{LT} \; ; \; (h_{Na} + dh_{Na}) \cdot \tan \beta_y + Y_{LT} \; ; \; (h_{Na} + dh_{Na})];$$

where the coordinates of the Laser Launching Facility are $[X_{LT} \; ; \; Y_{LT} \; ; \; 0]$ and β is the Laser launching angle.

A generic sub-aperture Si having centre coordinates [Si_x ; Si_y ; 0] sees the LGS under an angle:

$$\theta_i = \cos^{-1} \frac{\overrightarrow{S_iB} \cdot \overrightarrow{S_iC}}{\|\overrightarrow{S_iB}\| \, \|\overrightarrow{S_iC}\|}$$

Considering a circular aperture of diameter $D = 38.542m$ and a SH WFS having 80 sub-apertures across the diameter, the worst case in terms of elongation is represented by the sub-aperture at the opposite side of laser launcher position.

3.2 Spot truncation

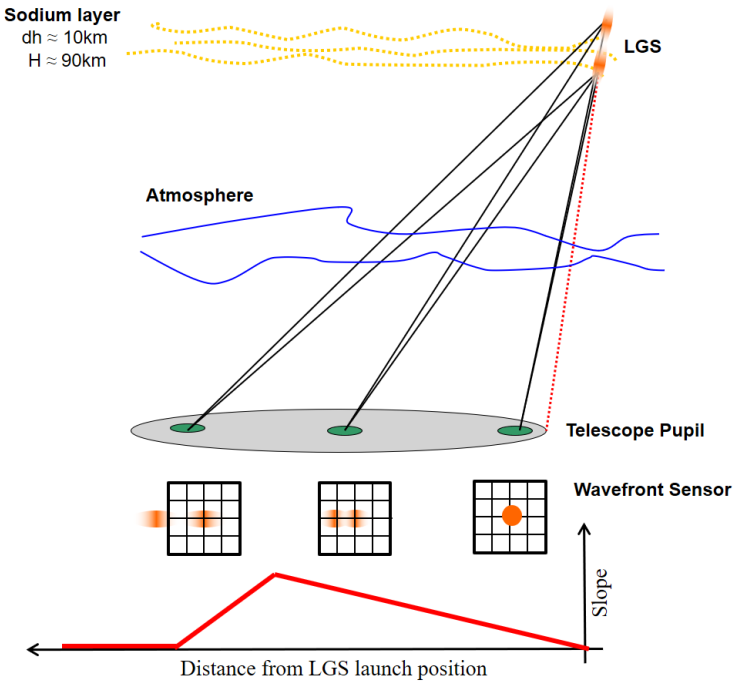

Figure 7 : LGS Spot truncation. Increasing the distance from the laser launcher position, the sub-apertur see two distinct images. There is a certain position where the finite sub-aperture FoV produces a truncation of the second spot and creates a discontinuity in the slope measurements.

Two sub-apertures placed at different distances from the laser launcher have the same FoV centered at the altitude H but see different segments of the LGS vertical extension. Hence, only the on axis sub-aperture detects the light from any altitude of the LGS. Moving towards the side of the lenslet array, the elongated spot could overflow into the adjacent sub-apertures and thus, it is necessary the use of a field stop whose purpose is to truncate the image of the LGS so that its real vertical extension corresponds to that re-imaged by the most elongated sub-apertures.

An interesting effect arises in the LGS WFS from the combination of the finite WFS FoV and of the sodium profile features. Consider Figure 7 where the sodium density profile has an ideal bi-modal distribution consisting only of two distinct spots separated by a certain altitude

range. In the LGS WFS sub-apertures close to the laser projection point, the perspective elongation effect is negligible and the two spots are essentially superimposed. If the LGS WFS is focused on one of these two spots, as the distance of the sub-aperture from the laser projection point increases, the two spots produce two distinct images. The one in focus at the centre of the sub-aperture FoV and the other closer to the sub-aperture FoV edge. The centroid therefore shifts away from the sub-aperture FoV centre, in a linear fashion with the distance from the laser projection point, out to a certain sub-aperture where the finite FoV produces a truncation of the second spot. A kind of discontinuity is produced in the centroid measurements (and hence the slopes) across the pupil, translating into more complex wavefront aberrations than pure tip-tilt and defocus. In fact, under the assumption of arbitrarily large LGS WFS FoV, the only wavefront terms related to the sodium layer profile structure and variation would be defocus and, in the case of edge projection, tip-tilt. Because of truncation effects due to the finite LGS WFS FoV, other wavefront aberrations are generated: these are only due to the sodium layer and have no relation with the wavefront aberrations due to atmospheric turbulence that AO system should compensate.

The sodium layer is also characterised by structured and time-variable density profile. Besides, any LGS WFS has finite field of view, typically because of the limited number of pixels of the detector which imposes a trade-off between sampling (i.e. spatial resolution of the imaged LGS spots) and field of view (i.e. extension which can be imaged on the WFS focal plane). The coupled effect of LGS spot truncation and sodium profile temporal variations are spurious and variable wavefront modes, which are only seen by the LGS WFS: their injection into the AO correction loop is detrimental to image quality and therefore an external reference – typically a WFS working on natural stars – is needed for keeping these modes under control. This external reference, independent from sodium layer issues, in MAORY is the so-called Reference WFS provided by an additional channel of the NGS WFS. The preliminary Reference WFS requirements in terms of number of sub-apertures, related to the number of Zernike [29] modes to be monitored, and the sampling time, have been derived using the simplified simulation tool described in [30].

Spot truncation and other LGS issues previously described, have been observed in numerical simulations, but their experimental verification is also deemed essential.

4. Laboratory experiment

The experimental work has been conducted by means of a laboratory prototype of a LGS WFS developed at INAF-OAS. The prototype reproduces the expected conditions, in the ELT case, when measuring the wavefront of LGS by means of a SH-WFS.

The laboratory experiment described here has been designed to achieve two main objectives:

- Experimental verification of LGS WFS performance under representative conditions for an ELT
- Supporting the design of the wavefront sensing system of the MAORY instrument for the ELT.

The prototype reproduces the expected conditions, in the ELT case, when measuring the wavefront of LGS by means of a SH-WFS. A simplified version of the prototype was successfully integrated and tested in 2010 [31]. It was able to generate realistic WFS data, including LGS spot perspective elongation and sodium profile features. The prototype has been upgraded [32] [33] to improve the accuracy on the generation of the desired sodium layer and to simulate, not simultaneously, a multiple LGS launching system.

The prototype SH has 40×40 illuminated sub-apertures and the array of spots is re-imaged onto a CCD camera. This WFS order is representative of the E-ELT, considering that the LGS WFS on the E-ELT will have typically 80×80 sub-apertures.

The equivalent sodium layer extension which can be imaged by the prototype is about 20 km in the most elongated sub-apertures, corresponding to about 20 arcsec on the ELT. The conceptual scheme and the experimental setup is shown in Figure 8. The main Prototype SH specifications are listed in Table 1. The light source in the prototype is the output end of an optical fibre, which is fed by an intensity-modulated light pencil: the intensity modulation is applied by a remotely-controlled spatial light modulator (HOLOEYE LC 2002 Transmissive SLM). The SLM is placed between a polarizer and an analyser in the so-called amplitude modulation transmissive mode. This configuration permits the arbitrary choice of transmittance set through 256 values for each SLM pixel (0 = no light ; 255 = full light) in order to simulate a realistic sodium density profile. The output end of the optical fibre and the SLM are both mounted on a motorised linear stage, while the input end of the optical fibre and the optics producing the light pencil feeding the fibre are fixed. The range of motion of the linear stage (about 10 mm) corresponds to the sodium layer extension which can be imaged on the camera. Along the linear stage motion, the output end of the fibre spans the

full sodium layer extension while the input light pencil crosses different portions of the SLM surface. The axial motion of the source is a variable defocus that translates into a lateral motion of the spots in the WFS sub-apertures. The camera exposure time is set to a few seconds, corresponding to the time necessary for a full span through the sodium layer drawn on the SLM. A tilt of the linear stage travel axis with respect to the prototype optical axis, produces the typical elongation pattern, which is not radial, of a side-launch geometry of the LGS.

The light source module in the prototype includes a Dove prism mounted on a motorised rotation stage whose axis is co-aligned with the optical axis. By changing the position angle of the prism, it is possible to change configuration as if the LGS was launched from a different position around the edge of the telescope which is emulated by the prototype.

Atmospheric-like turbulence may be optionally generated by two plastic screens placed at the aperture stop of the prototype. The screens are mounted on X-Y linear stages to possibly apply temporal evolution.

A field stop is placed at an intermediate focal plane: its diameter can be manually adjusted to introduce different truncations on the LGS images produced by the WFS.

The prototype includes a low-order deformable mirror (ALPAO DM52 with 52 actuators). The purpose of the DM is to introduce low-order and static wavefront aberrations for the test described in Section 4.5. In the remaining test cases, there is no voltage applied to the actuators and the DM surface can be approximated to a flat rigid mirror.

The core of the Shack-Hartmann WFS is a lenslet array, characterised by square geometry, pitch size 300 µm, focal length 3.82 mm.

The array of Shack-Hartmann images is recorded by a scientific-grade CCD camera (pixel size 13 µm, 1k×1k pixels). Each WFS sub-aperture is mapped onto 24×24 pixels of the CCD camera. A re-imager module is necessary to fit the lenslet array pitch with an integer and even number of detector pixels per sub-aperture.

The LGS spots are sampled by 2 pixels per FWHM along the non-elongated axis. Analogue on-chip binning or numerical binning may be used to reduce the sampling to only 1 pixel per FWHM and emulate severe under-sampling conditions.

All the prototype functions are controlled by custom control software coded in C/C++. The software controls all devices (motorised stages, SLM, DM, camera) and manages the

prototype configuration setup and the acquisition cycles. Data reduction is performed by specific software coded in high-level language IDL®.

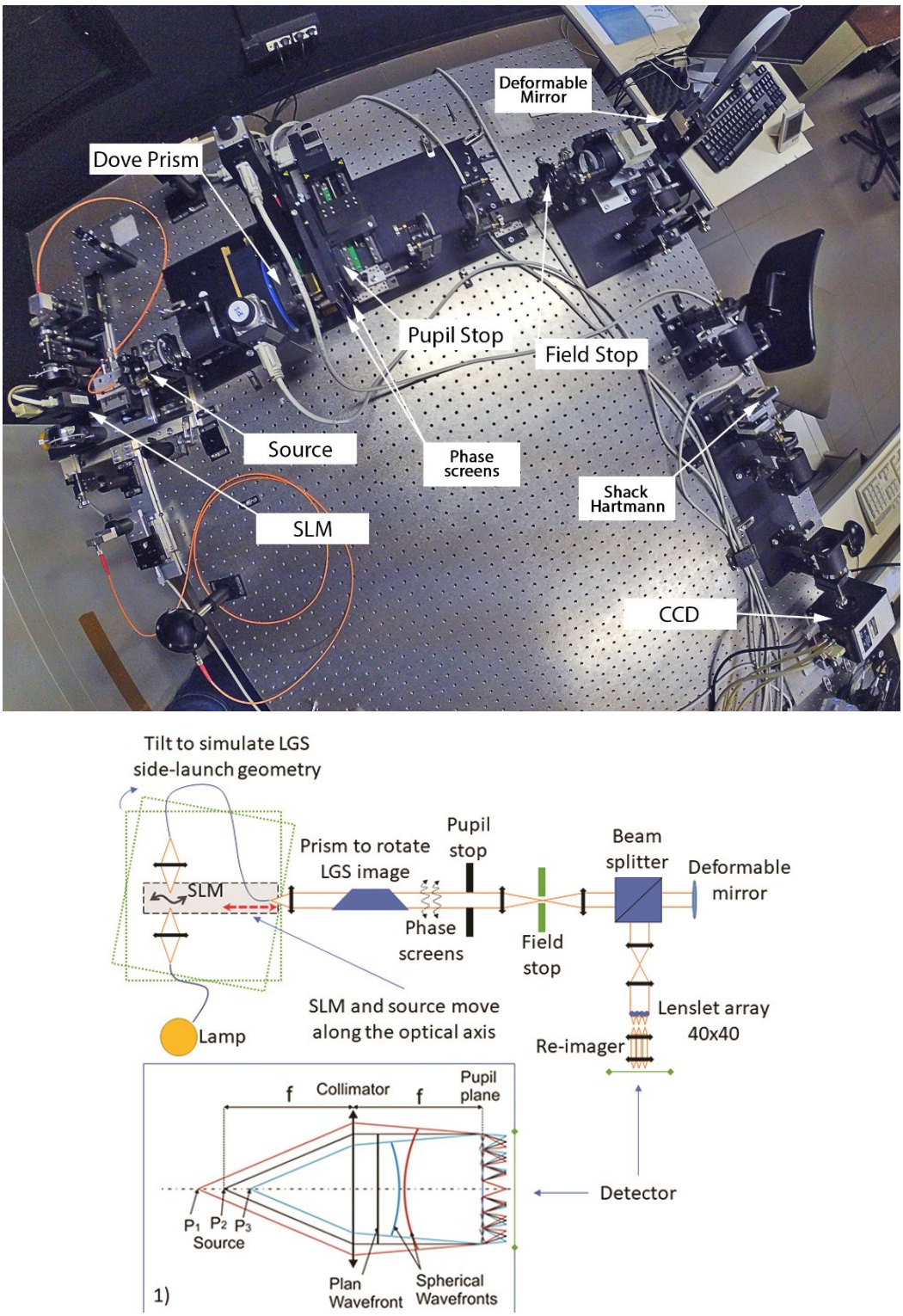

Figure 8: Prototype integrated on the optical bench and Prototype conceptual scheme. The axial motion of the source is a variable defocus that translates into a lateral motion of the spots in the WFS sub-apertures. The light intensity modulation is applied by a transmissive SLM. A tilt, respect to the optical axis, simulates the LGS side launch configuration. The prism, rotating around the optical axis, changes the LGS launcher position around the pupil. Phase screens can be placed before the pupil stop. After the DM, conjugated to the pupil, a re-imager module is necessary to fit the lenslet array pitch with an integer and even number of detector pixels per sub-aperture.

Table 1 : Prototype built-in SH, main specifications

Shack-Hartmann specifications	
Fully illuminated Sub-apertures	1264
Sub-aperture diameter	300 µm
Sub-aperture focal length	3.82 mm
Sub-aperture number of pixels	24x24
Pixel size	13µm
CCD camera Read-Out-Noise	$11e^-$

4.1 Common test conditions, limits and calibrations

The Prototype was integrated under a controlled room temperature to reduce thermal fluctuations that effect the system performance. Fixing the temperature at 23ºC, the air conditioning system generates a periodic variation within 1 ºC. This introduces a systematic error in the measures that is translated in global X-Y centroids offset in function of the temperature. The effect is a loss of precision, i.e. a dispersion of a set of WFS images. In terms of RMS WFE, ≈100nm of differential Tip and Tilt terms are introduced while the root sum of squared higher order terms is below 12nm.

Every test was performed in a regime of SNR where the number of photons per sub-aperture (n) stay within 500 and 5000. The laboratory CCD camera has a RON of $15e^-$ /pixel. In a CCD RON-dominated:

$$\text{SNR} = \frac{n}{\sqrt{n+RON^2}}$$

Scaling the SNR to a typical AO CCD RON of $4e^-$ /pixel, the equivalent number of detected photon per sub-aperture stay within 360 and 4800.

In SH WFS, at linear regime, centroid coordinates are a direct measure of the local wavefront slope. The Center of Gravity (CoG) is a simple algorithm to estimate the spot position but it is very sensitive to noise. A solution to reduce the noise is to apply a threshold.

The threshold value T_h is determined as follows:

$$T_h = T_{\%} \cdot \max(I)$$

Where $T_{\%}$ is the percentage relative to the maximum intensity (max(I)). The threshold modifies the intensity distribution as follows:

$$I_t = \begin{cases} I - T_h & \text{for } I \geq T_h \\ 0 & \text{for } I < T_h \end{cases}$$

The CoG with a threshold reduces the noise but is still sensitive to the LGS density profile shape and temporal variation. A solution to mitigate these effects is to use the Weighted Center of Gravity (WCoG) [34] algorithm which uses a “reference image" to evaluate the spot position and it is less sensitive to noise and LGS image intensity variations.

The “reference image" can be assumed equal to the mean LGS image inside each sub-aperture within a given timescale [35]. The reference acts as a weighted function which reduces the noise effects but introduces an error on the centroid estimation that is proportional to the distance of the actual centroid from the centre of the weighting function. To compensate this error, a calibration curve is empirically derived in each sub-aperture [35].

The prototype experiments didn't consider the temporal aspects of atmospheric turbulence and the LGS image, inside each sub-aperture, has a fixed position. This condition makes negligible any biasing effects due to the weighting function which are not considered. The experimental results, described in this paper, refer only to WFS performance using WCoG centroiding.

Centroid measures were translated in Optical-Path-Difference (OPD) as follows:

$$\begin{cases} OPD_x = \dfrac{d}{f}\,\Delta x \\ OPD_y = \dfrac{d}{f}\,\Delta y \end{cases}$$

Where d is the lenslet diameter and f its focal length. Δx and Δy are centroid coordinates respect to the sub-aperture centre.

Test results that consider the distribution of sub-aperture OPD are always corrected for the median RMS offset introduced by temperature variations.

Test results that consider the distribution of RMS WFE are always corrected for prototype static aberrations that are measured by taking as reference a top-hat sodium profile that does not extend outside the field stop. These corrections on OPD and WFE are a kind of bias subtraction in the resulting data.

To retrieve a wavefront from centroid measures, the followed approach is a modal reconstruction method with Zernike polynomials. The numbers of modes used to fit the wavefront aberrations are 252 Zernike. Further increment on the number of modes results negligible in terms of fit residuals which are within numerical accuracy. Everytime a total RMS WFE is computed, Tip-Tilt and defocus are excluded (Z_2 to Z_4). MAORY is designed to work with a reference WFS based on NGSs to monitor low-order wavefront aberrations. Thus, some tests also considered the total RMS WFE for Zernike modes above 54 (Z_{54}) as a relevant information to support the definition of the requirements of the NGS wavefront sensing sub-system.

The SLM displays a chosen sodium density profile on a grayscale from 0 to 255 levels that is not linear. Any chosen sodium density profile has to be calibrated by the SLM curve response (see Section 4.2).

The Prototype light source, a multimode optical fibre, delivers an output beam whose intensity distribution is approximately Gaussian in shape, involving a gradual drop of the pupil image intensity at its borders. The multimode optical fibre allows the propagation of different light modes whose superposition, at the output end of the fibre, generates lighting inhomogeneities at the pupil stop (see Section 4.2).

Simulated LGS launcher position is on the edge of telescope primary mirror and each sample of images does not consider the temporal aspects of atmospheric turbulence. Given a static sodium density profile, the smallest sample of images, used for the test statistic, contains 100 images. Data reduction takes care of background subtraction, hot pixels, bad lines and cosmic rays. Corrupted pixels values were replaced by the mean of adjacent pixels. Extensive test campaigns have been carried out with the experimental setup. Selected results are shown here.

4.2 End-to-end code verification

The same sodium profiles have been injected into the prototype and, for comparison, into the AO end-to-end simulation code developed for the MAORY instrument project. The MAORY end-to-end simulation code [36] [37] has been designed to accurately model the LGS image

in the Shack-Hartmann (SH) WFS sub-apertures and to allow sodium profile temporal evolution. The code allows also the simulation of transverse structures, possibly leading to differential effects among the LGSs. The fidelity with which the simulation code translates the sodium profiles in LGS images at the WFS focal plane has been verified using the laboratory Prototype. This test has allowed to verify and to refine the LGS image modelling method implemented in the end-to-end code.

The LGS is an extended light source at a finite distance from the telescope. The LGS image is strongly dependent to perspective elongation given by the laser launcher position relative to the optical axis of a sub-aperture and the longitudinal distance between the LGS and the sub-aperture. We numerically treat the extended LGS as the superposition of portions sliced into planes which are perpendicular to the telescope optical axis. One of the consequences of the cone effect or focus anisoplanatism is that the LGS section at lower layers is nearer the telescope than that at the upper layers and this would cause a stronger intensity at the image plane. Because of geometric optics, the LGS lower layer portions undergo an increase in both magnification and angular deviation of their image positions. On the contrary, for unit increment of LGS altitude, the peak intensity of its image, which undergoes a demagnification, decreases as well as the angular deviation of its image position. After superposing all the LGS portion images, the intensity distribution of a perspective image is determined.

The laboratory prototype requires a calibration procedure to retrieve a correct image from a realistic sodium density profile. Since we use a SLM which displays the density profile in terms of grayscale values, the required process is the follow (see Figure 13):

1. Chose a sodium density profile
2. Calibrate for the SLM curve response. Variations of light intensity are on the grayscale from 0 to 255 levels.
3. Associate the SLM pixels to layer altitudes according to perspective elongation. Since, in the real case, the angular deviation of the image position as a function of a layer altitude is not linear, we have to convert the linear relation between the SLM pixels and the perspective elongation of the SH sub-images peculiar to the Prototype.

The differences from simulation are shown in Figure 14 where the relative maximum intensity of each sub-aperture along the pupil diameter (that means with the elongated spot aligned with the pixel grid) are plotted in the case of a LGS image. Due to elongation, we expect that the image peak intensities reach their maximum close to the laser launcher position but, for

the reasons discussed in Section 0, the Prototype behaves differently. Even if this effect influences the absolute image shapes, it is not important for the scope of every tests since we are interested in relative measures to be cross-checked with the simulations.

The simulated MAORY control scheme is based on three nested AO loops with a different temporal rate [38]. The fasters are for the LGS WFS and a Tip-Tilt Focus Astigmatism (TTFA) NGS WFS which computes the first 5 Zernike modes. The slower is for the Reference WFS. The number and type of WFSs and of DMs can be set as an input of the simulation. In the case of LGS, it is possible to vary the sodium density profile for each simulation step and from one LGS to another.

The flow diagram of the code is shown in Figure 9 where the green box indicates the process that run in open loop (wavefronts generation, including telescope aberrations) and whose outputs, together with the blue box outputs, are used to run the closed loop simulation. The cone effect and the laser up-link propagation are taken into account. The phase screens are computed from the phase (Kolmogorov or Von Karman) Power Spectrum.

An accurate description of the code is reported in [36].

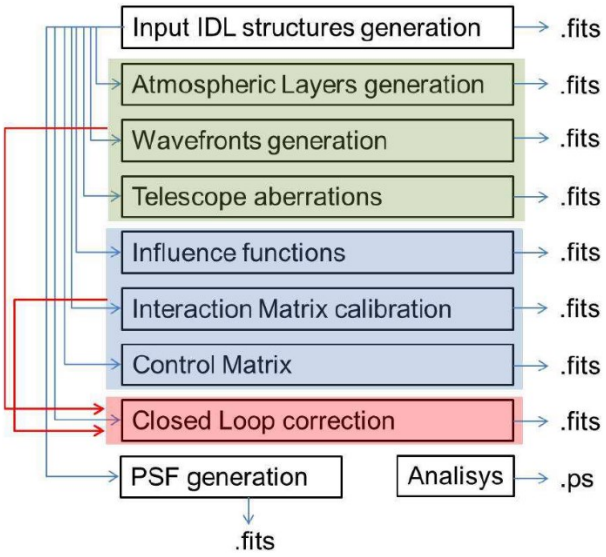

Figure 9 : The simulation code main modules and their interactions. The input parameters are used to build IDL data structures that feed the single modules. The coloured boxes highlight the dependency between the modules. In the first block (green) the wavefronts are generated in open loop and stored; in the second block (blue) mainly the control matrix is computed; then the closed loop takes place (red block); finally, the PSF is computed.

The LGS SH-WFSs are simulated in order to accurately reproduce the projected LGS image in each sub-aperture. It is foreseen the possibility to divide the sodium layer in an arbitrary

number of sub-layers, in order to take into account for different wavefronts related to different sodium layer slices. For each sodium sublayer the step through which each SH sub-aperture is simulated follows this process:

1. The sodium profile portion is projected onto a 2D array having a pixel size that matches one-half of the sub-aperture diffraction limit PSF. This transformation takes into account for the exact geometry of the laser launching system. A 1:1 correspondence between points in the sub-aperture space and points in the sodium profile space is ensured by analytical formulas, starting from a reference altitude that refers to the sub-aperture centre. This reference altitude can change during the simulation according to changes in laser focusing due to zenith angle or to sodium layer variations. Once the pixels that are crossed by the projection of the sodium profile in the sub-aperture are individuated, they are translated into angles under which the profile is seen from each pixel in that specific sub-aperture. Note that the projected profile will intersect the pixel grid defining an irregular grid that depends on the projected profile inclination with respect to the pixel grid, according to the relative position of the sub-aperture respect to the launching laser position.

The value of the pixel that is crossed by the projected profile between two points of intersection is set to the value of the integral of the profile between the altitudes that correspond to the intersection points. This operation is repeated for each of the pixels along the projected profile portion. This computation is done for each considered profile, for all the stars, in open loop and stored in an IDL structure for the closed loop operations. Only the value of the interested pixels is kept in memory.

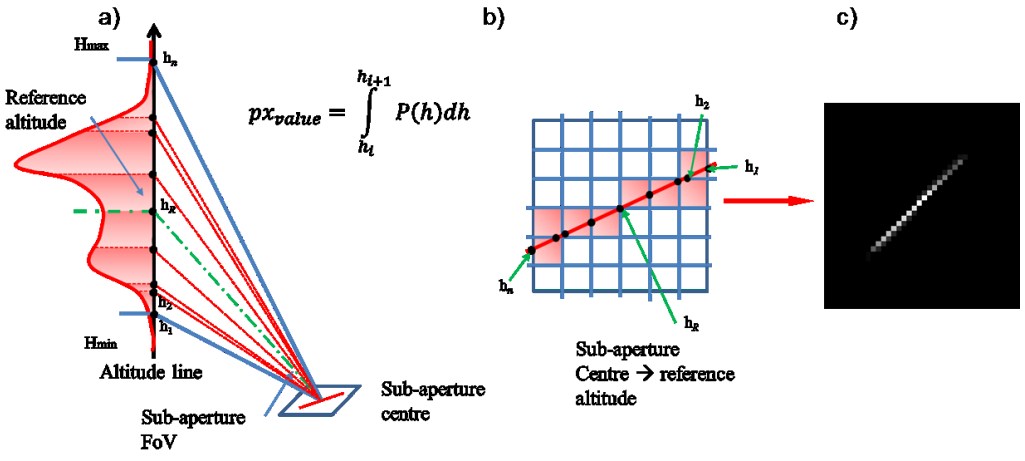

Figure 10 : The process of sodium profile projection in each sub-aperture is illustrated. a) H_{min} and H_{max} represent the altitudes that limit the sub-aperture FoV; the green dashed-dotted line highlights the reference

altitude h_R centered in the sub-aperture FoV; the black dots along the altitude line represent the altitudes corresponding to the projection of the points of intersection between the detector pixel grid and the projected profile in the sub-aperture (b). c) shows an example of projected profile in a simulated sub-aperture.

The array size is grater-equal than the sub-aperture FoV multiplied for an integer number given by the final WFS pixel-scale divided by the actual oversampled pixel-scale. The WFS pixel scale is slightly modified in order to be an exact multiple of the diffraction limit pixel size (in the case of MAORY, the diffraction limit pixel size is always smaller than the WFS pixel size). The enhanced FoV is given by the sub-aperture FoV + the size of the long exposure laser image FWHM, in order to avoid the introduction of spurious effects due to truncation.

2. The projected sodium profile portion is then convolved for the long exposure laser PSF. The long exposure laser PSF (that can be either a 2D Gaussian with a given FWHM, or an arbitrary image) is shifted in X and Y by an integer number of pixels corresponding to the integer part of the shift due to the local wavefront tilt (if any). Consequently, the tilt contribution corresponding to that integer shift, is subtracted by the local wavefront. This operation is necessary to avoid the introduction of spurious effects due to the simulation.
3. Now the Field stop can be applied, simply nulling the value of the pixels that fall outside the Field Stop FoV. The Field stop can be set different from the sub-aperture FoV (i.e. smaller).
4. The Diffraction Limited PSF is computed through sub-residual WF Fast Fourier Transform and used as a kernel for the convolution of the array previously computed.
5. This operation is repeated for each profile portion and summed up.
6. The resulting image is re-binned to the final WFS pixel scale.
7. The resulting sub-aperture image is summed up to the total WFS image. Note that the sub-aperture image size remains bigger than the size given by the sub-aperture FoV, in order to not cut the image blur due to sub-aperture diffraction.
8. The photon and readout noise are added.

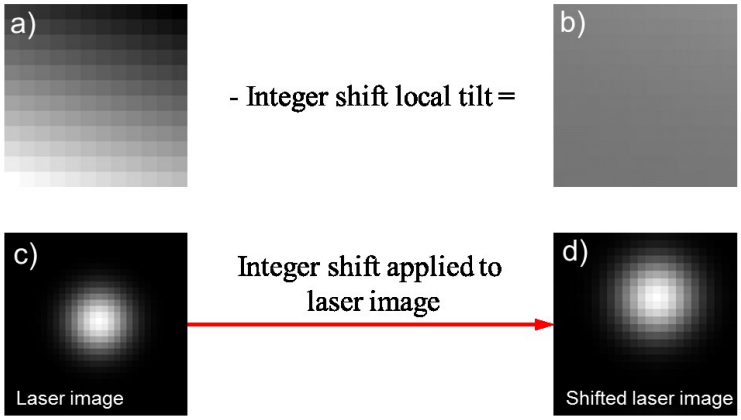

Figure 11 : The long exposure laser PSF is shifted in X and Y by an integer number of pixels corresponding to the integer part of the shift due to the local wavefront tilt.

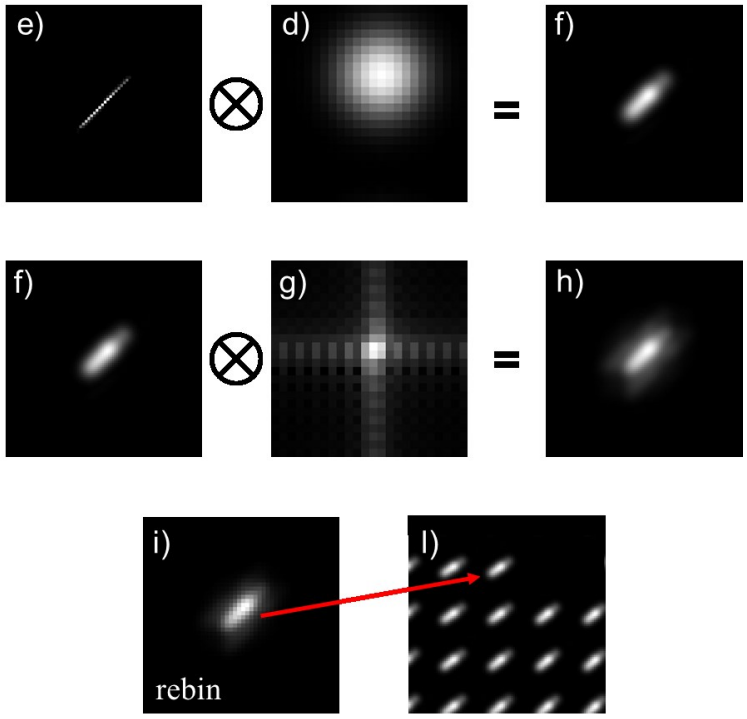

Figure 12 : Simulated LGS WFS image process: the projected sodium profile (e) is convolved for the shifted laser image (d) and then convolved for the sub-aperture diffraction PSF (g). The image (h) is re-binned to the final WFS pixel scale (i) and summed up to the global image (l).

The sodium profile can be changed from one simulation step to the next and from one star to another. For the SH WFS optimization, different algorithms for centroid computation have been implemented (simple center of gravity, center of gravity with a given threshold, weighted center of gravity and correlation). Even the pupil can be updated in order to study effects of mis-registration.

To compare the LGS images, we used one of the on-sky sodium density profile data from Lick Observatory [39] and run the simulation excluding the atmospheric turbulence and additional sources of noise (i.e. detector noise, background light, photon noise, etc.). In the case of Prototype data, we acquired the images in very high SNR regime so that they are almost noise free. As reference for the comparison, we show in Figure 15 the image of the real sodium density profile as seen by the most elongated sub-aperture along the pupil diameter. The image was converted to one dimensional profile by summing up the pixel values perpendicular to the elongated direction. At this point, the linear Pearson correlation coefficient was used, as parameter, to compare the two profiles resulting from simulation and prototype images. The computed coefficient was equal to 0.97 implying a very high correlation between the two reproduced profiles.

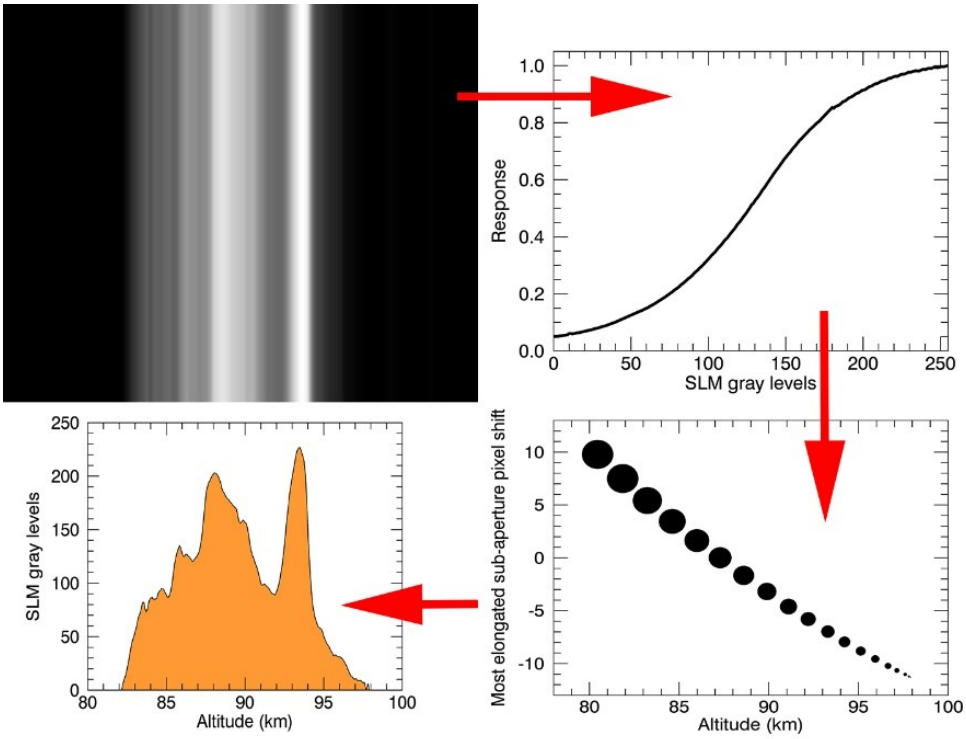

Figure 13 : SLM calibration procedure. To reproduce a realistic sodium density profile in terms of grayscale levels (up-left Figure), the profile has to be calibrated for the SLM curve response (up-right Figure) and finally, the SLM pixels have to be associated to layer altitudes according to perspective elongation (bottom-right Figure). Here the symbols (black circles) follow the image demagnification as the altitude of a LGS portion increases.

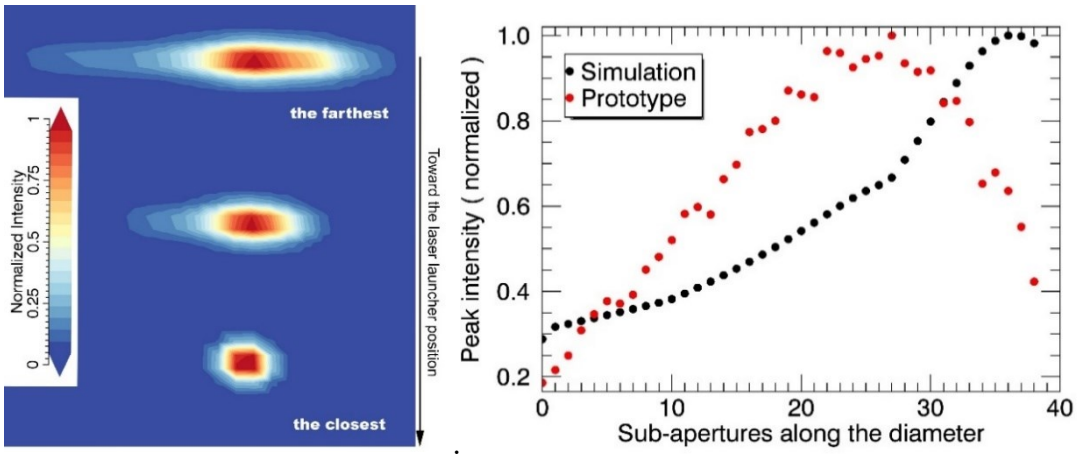

Figure 14 : Left: WFS Image of three representative sub-apertures in the pupil. Right: relative maximum intensity of each sub-aperture along the pupil diameter in the case of a LGS image with a side-launch configuration. The Prototype suffers from not uniform pupil illumination.

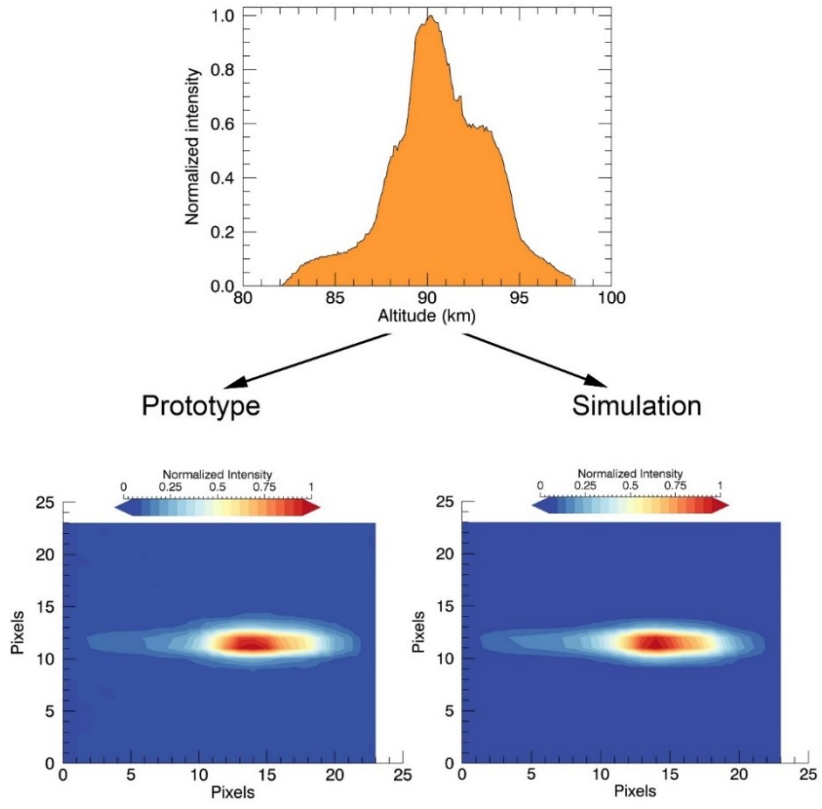

Figure 15 : Real sodium density profile in function of altitude. This profile is equally seen by the most elongated sub-aperture on the pupil diameter in both cases of Simulation and Prototype data.

4.3 Wavefront sensor measurement errors

The measurement error at WFS sub-aperture level has been studied for different conditions of SNR, sodium profile and centroid algorithm. In all the cases very good match has been found between experimental results and theoretical expectations derived from numerical simulations. In this subsection, the experimental results refer to a Gaussian sodium profile for three conditions of SNR.

Any centroid algorithms performance is mainly affected by the following sources of error:

- Photon noise which follows a Poisson distribution and starts to be significant when the light intensity is low.
- Background noise which includes hot pixels, bad lines and cosmic rays.
- Sampling error which is related to the detector pixels size.
- Fixed pattern noise which is related to the digitization of light intensity by pixels.
- Sidelobes of the spot irradiance distribution which depends not only on diffraction but also on optical surface imperfection (i.e. scratches, dig, bubbles). If the sidelobes symmetry was broken within the centroid searching area, it could cause centroid errors.

In typical LGS images delivered by the prototype is not possible to distinguish these error sources one from the other. For these reasons and many other aspects described in the previous Section, the simulation and prototype data will always be different.

Figure 16 shows the prototype WFS measurement errors in terms of RMS OPDs compared to the theoretical behaviour. Given a sample of images, the RMS OPD of each sub-aperture is the RMS position difference of centroid measurements with respect to the mean.

To assess the performances of WGoC for different levels of SNR, the mean photon counts per sub-aperture is considered as indicator of noise and the distribution of RMS OPD values of the sub-apertures is the performance measure. Figure 16 considers three levels of SNR increasing from SNR-3 to SNR-1. The equivalent number of photon counts per sub-aperture is ≈ 1800 for SNR-3, ≈ 2700 for SNR-2 and ≈ 4700 for SNR-1. Considering a sub-pupil of 0.5m and the LGS WFS operating at 700Hz, these numbers are representative of expected LGS return flux per sub-aperture at ELT site. The three distributions are RMS OPD values of 40x40 sub-apertures. As expected, more photon counts per sub-aperture means a better centroiding accuracy.

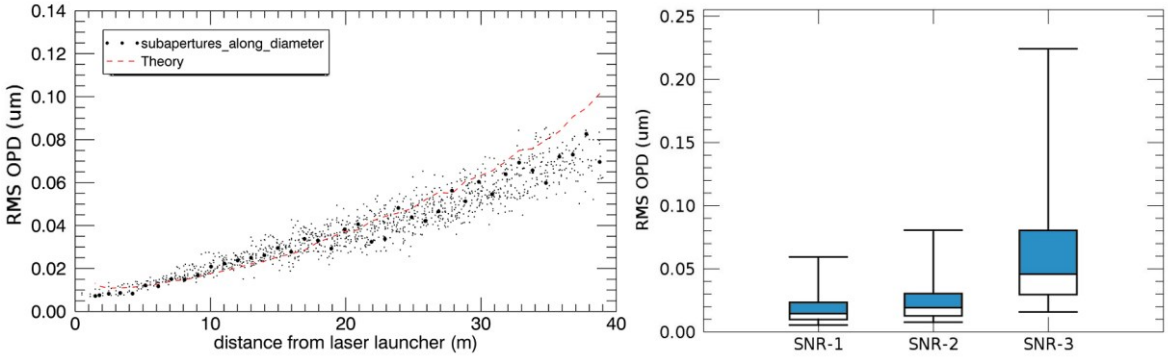

Figure 16 : Measurements performed by WCoG algorithm with a Gaussian sodium density profile. Left: The RMS OPD values of each sub-aperture are the black dots. The theoretical behaviour in function of the distance from laser launcher is the dashed line. Bigger black dots are RMS OPD values of the sub-apertures where the LGS elongation is parallel to the lenslet side. Right: RMS OPD distributions for three levels of SNR. Each box plot is the distribution of RMS OPD values of the sub-apertures. Number of photons per sub-aperture is ≈1800 for SNR-3, ≈2700 for SNR-2 and ≈4700 for SNR-1. Box plots show minimum and maximum values and quartiles.

4.4 Effect of image truncation

Sodium profiles have been injected into the prototype and wavefront sensing has been performed without and with truncation effects. Truncation effects make the WFS detect additional spurious aberrations, especially affecting the first few tens of Zernike modes, which would require a kind of on-line calibration of the LGS WFS measurements by additional reference measurements (e.g. to be performed on NGS).

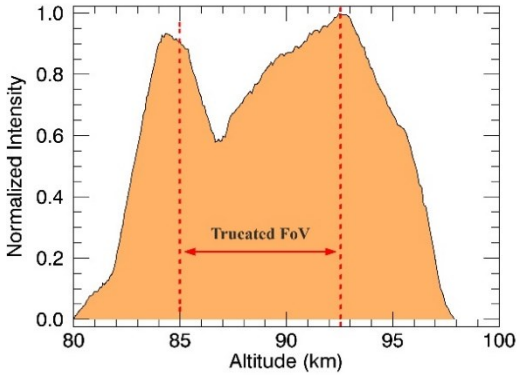

Figure 17 : Realistic sodium density profile used to evaluate the effect of LGS image truncation. Altitude range (20Km) refers to the maximum sub-aperture FoV (about 20 arcsec).

For comparison, we selected a sodium density profile entirely contained in the maximum sub-aperture FoV which is varied by means of a field stop. The following results are related to the sodium density profile shown in Figure 17. The image truncation is symmetric respect the two density peaks. Figure 18 shows the difference in terms of total RMS WFE for sub-

aperture FoV of 18 arcsec and 7.5 arcsec. Each boxplot is the RMS WFE distribution of all images for a given test condition. Given a sample of WFS images at the same test conditions, each box plot is the RMS WFE distribution of the sample. These results are not influenced by data calibrations described in Section 4.1 since, as already mentioned, the calibration procedure is a kind of bias sustraction of resulting data as shown in Figure 19. The measured wavefronts, with and without image truncation, are not corrected for prototype static aberrations and lead to the same conclusions. The LGS truncation introduces hundreds of nanometers of low-order WFE and it is less significant for modes above Z_{54}.

It has to be considered a loss of photons of about 10% on the entire pupil due to the field stop. The effect of different SNR combined to a fixed level of truncation is the subject of next session.

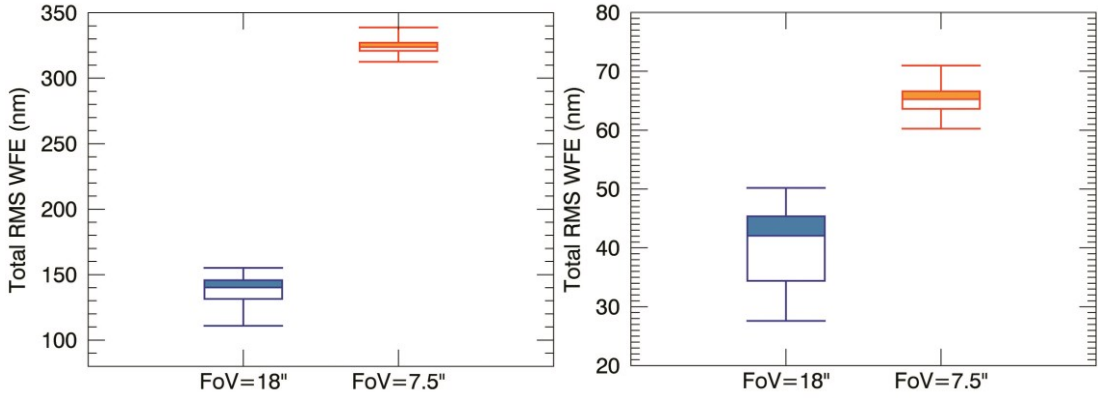

Figure 18 : WCoG algorithm results described in Section 4.4.. Upper plot: Total RMS WFE above Z_4; Lower plot: Total RMS WFE above Z_{54}. Given a sample of WFS images, these are the distributions of the total RMS WFE (in nanometers) introduced by the static sodium density profile of Figure 17 for two different FoV. Box plots show minimum and maximum values and quartiles.

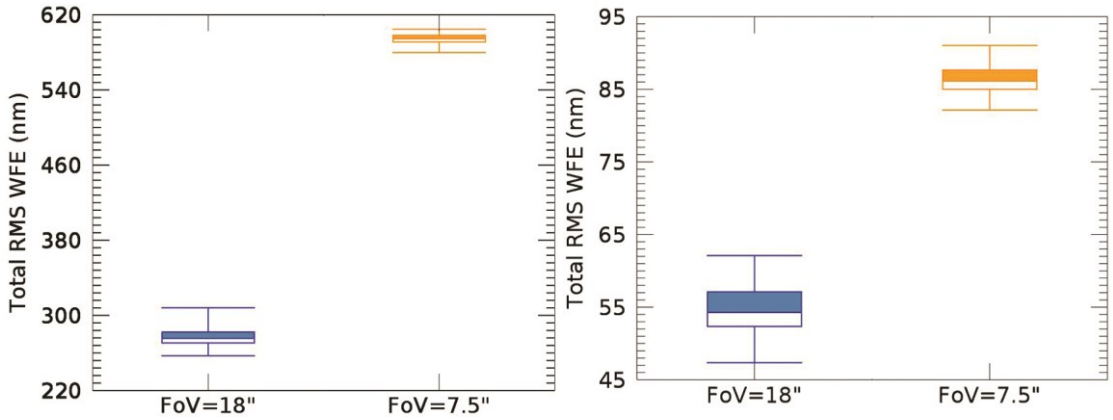

Figure 19 : Same of Figure 18 but without calibration for prototype static aberrations.

It has to be considered a loss of photons of about 10% on the entire pupil due to the field stop. The effect of different SNR combined to a fixed level of truncation is the subject of next session.

4.4.1 Truncation vs SNR

This section evaluates the effect of LGS image truncation compared to different levels of SNR. The selected sodium density profile is entirely contained in the maximum sub-aperture FoV which is varied by means of a filed stop.

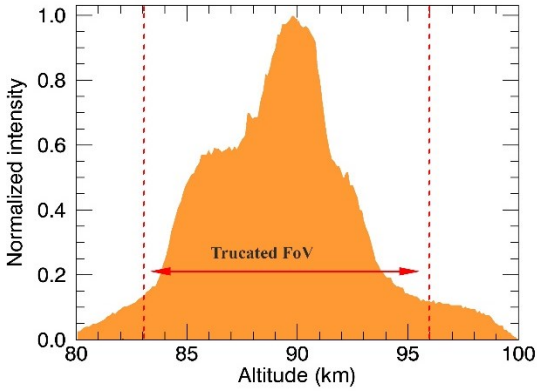

Figure 20 : Realistic sodium density profile used to evaluate the effect of LGS image truncation vs SNR. Altitude range (20Km) refers to the maximum sub-aperture FoV (about 20 arcsec).

The following results are related to the sodium density profile showed on the right of Figure 20. The image truncation regards the low end of density distribution. The number of photons per sub-aperture are regulated by changing the source light intensity. Two levels of SNR have been set when there is no truncation while a fixed SNR, that falls between the other two, has been set when truncation occurs.

Figure 21 shows the difference in terms of total RMS WFE for a sub-aperture FoV of 19 arcsec and 13 arcsec. Given a sample of WFS images at the same test conditions, each box plot is the RMS WFE distribution of the sample. Blue boxes refer to no-truncated profile whose SNR decreases going from left to right. Orange boxes refer to truncated profile whose SNR is fixed. The effect of reduced SNR translates to greater RMS WFE as well as a wider distribution due to noise. However, the medians of RMS WFE distributions of not truncated cases (blue), are lower than the truncated case (orange).

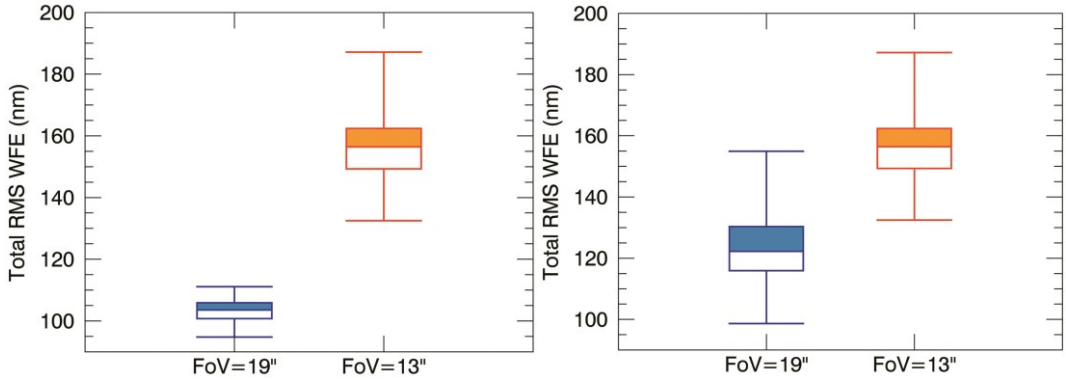

Figure 21 : WCoG algorithm results described in Section 4.4.1. Statistical distribution of the total RMS WFE (in nanometer) introduced by the static sodium density profile of Figure 20 for two different FoV. Truncated LGS image is the orange boxplot. Upper plot: Comparison with higher level of SNR of not truncated case (blue); Lower plot: Comparison with lower level of SNR of not truncated case (blue). The box has lines at the lower-quartile, median, and upper-quartile values.

To avoid LGS truncation, for a given number of pixels, the sub-aperture FoV may be increased by under-sampling. However, in this case the WFS loses linearity. Two different approaches are under investigation:

- To calibrate the gain of the centroid algorithm for non-linearity effects introducing a known periodic tilt signal on both axes via a LGS WFS jitter compensation mirrors;
- To introduce a blur in the LGS image in order to re-cover Nyquist sampling in the non-elongated axis, with a negligible effect on the elongated axis.

In the next section, the first approach is explained.

4.5 Effect of image under-sampling

Under-sampled WFS data have been produced by numerical binning of Nyquist-sampled data. Wavefront measurements have been performed on both data sets, using the Nyquist-sampled data as a reference. A centroid gain calibration method has been implemented, based on spot dithering. Under-sampling degrades wavefront measurement performance by up to 25% under the adopted test conditions; the calibration method brings the error down to about 5%.

To retrieve the wavefront from centroids measurements, the followed approach is a modal reconstruction with Zernike polynomials. Offsets in terms of centroids translates into residual WFE RMS. To mitigate the effect of under-sampling, the implemented gain centroid calibration procedure is based on spots modulation (i.e. “dithering”) by numerically shifting

the Nyquist sampled LGS images by an integer amounts of pixels (before applying the 2x2 numerical binning), in order to avoid errors due to numerical interpolation (±1 pixels). The modulated images are then binned and a calibration curve is derived for each sub-aperture. The calibration curve links the detected centroids to the true amount of image shifts.

The calibrated centroids are defined as follows:

$$C(x, y) = \sum_n a_n(x, y) \cdot C_o(x, y)^n$$

Where $a_n(x, y)$ are the coefficients of the calibration curve, $C_o(x, y)$ are the x and y measured centroids and n is the polynomial degree used to fit the curve. As a first approximation, first degree polynomial was used.

The sodium profile of Figure 20 has been used without truncation in order to disentangle non-linearity effects due to under-sampling and non-linearity effects due to LGS image truncation. The test has been conducted in very high SNR condition to avoid centroid errors due to noise. Through the DM integrated in the prototype, a certain amount of low-order aberrations can be introduced for the purpose of shift the LGS spots within the sub-apertures and therefore force the WFS to work in a non-linear regime (in case of under-sampling condition).

A single “noise free" and Nyquist sampled LGS image has been acquired with the SH-WFS. The measured spot centroids are used as reference. Applying the 2x2 numerical binning on the image, new centroids coordinates are detected and their offset from the Nyquist case is the performance measure. After the calibration procedure, the spot centroids offset due to under-sampling was again evaluated using the same reference.

To retrieve the wavefront from centroids measurements, the followed approach is a modal reconstruction with Zernike polynomials. Offsets in terms of spot centroids translate into residual WFE.

The results, in terms of OPD, are shown in Figure 22. Each dot is a single sub-aperture offset from the Nyquist case. They have been computed by subtracting the centroid values in the case of 2x2 image binning from the corresponding centroid values in the case of Nyquist sampling and summing in quadrature the x and y OPD. Black dots correspond to OPDs offsets due to the absence of a gain calibration procedure, while red dots correspond to OPD offsets when the calibration procedure is applied. It is clear that sub-apertures near the laser launcher position strongly suffer the under-sampling effect because in that region of the pupil, where there is a moderate LGS elongation, the spots are severely under-sampled in both axes. The wavefront maps of Figure 22 refer to residual aberrations (Z_2 to Z_4 excluded) introduced by

the effect of under-sampling in the cases where a centroid calibration procedure does (left panel) and does not (right panel) occur.

A centroid calibration, based on spot modulation, mitigates the effect of under-sampling reducing the residual RMS WFE from ≈ 103nm to ≈ 26nm. This means that the deviation from a Nyquist detector is reduced by a factor of ≈ 4 when using spot modulation.

Of course, these results were obtained on a scaled model (40x40 sub-apertures instead of 80x80) and under simplified experimental conditions.

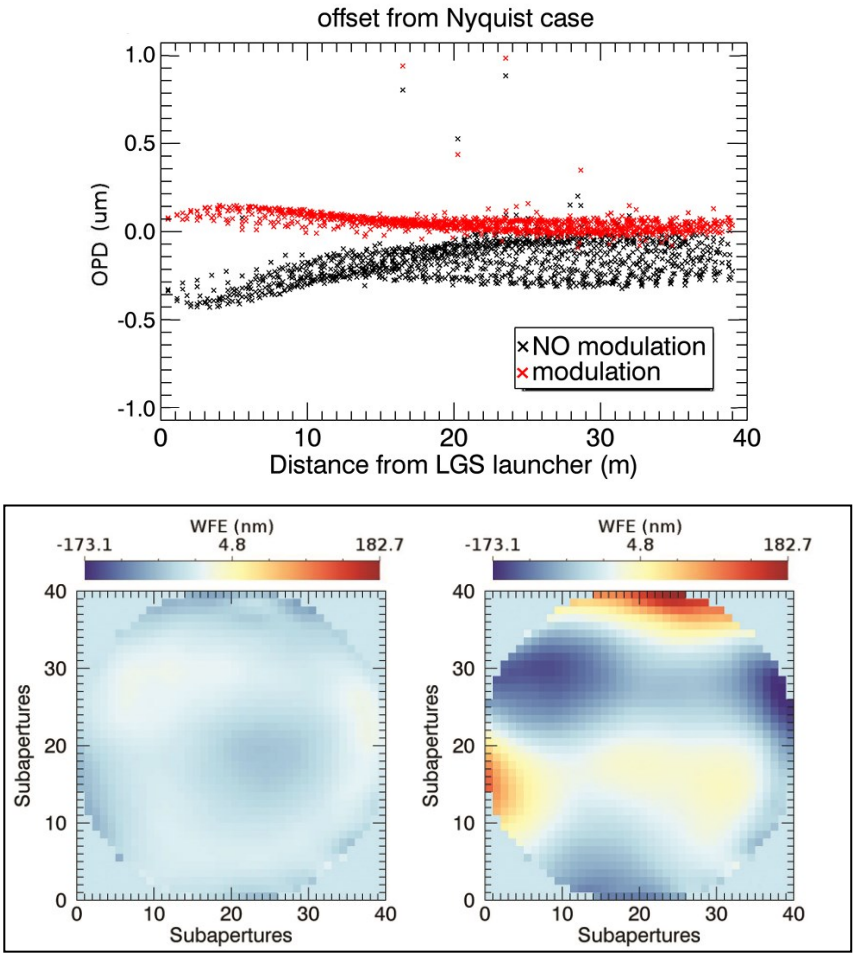

Figure 22 : Test results described in Section 4.5. The sodium profile of Figure 20 has been used. Upper plot: Centroid offset on under-sampled data, with respect to centroid measurements obtained on Nyquist-sampled data, as a function of sub-aperture distance from the laser launching position. Red points are OPDs after calibration for under-sampling; black points are OPDs without calibration. Lower plot: Residual wavefront map (nm) due to centroid offsets with calibration (left) and without calibration (right).

4.6 Effect of sodium density profile variation

Within this section, the effect of variable sodium density profile is evaluated in terms of RMS WFE.

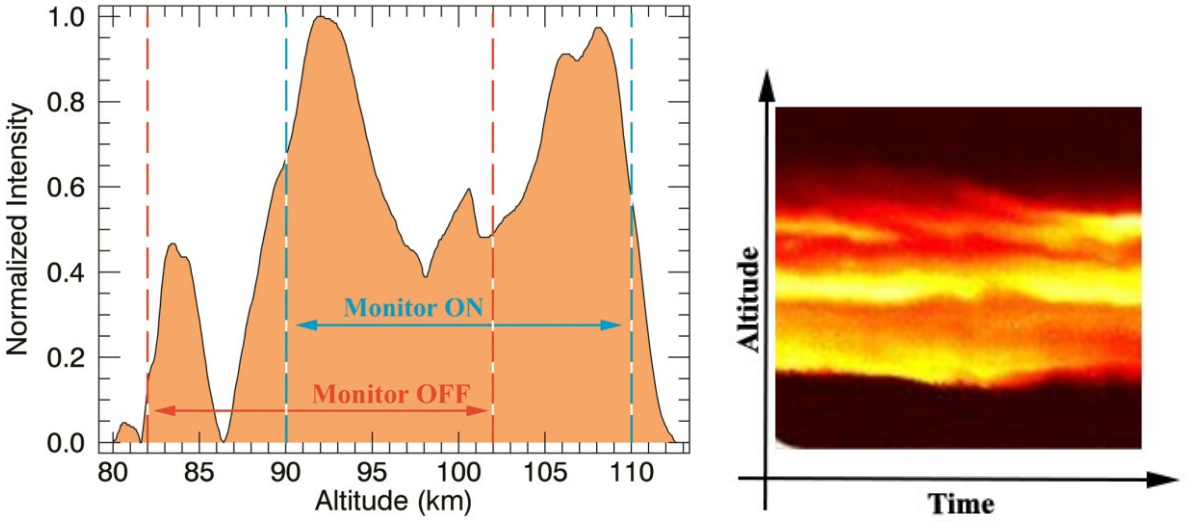

Figure 23 : Sequence of sodium density profile in function of Time and Altitude (right). One of the profile extracted from the sequence and used for test measures (left). Herein is showed an example of how the maximum sub-aperture FoV changes in the case we are monitoring (blue) or not monitoring (red) the complete sodium density distribution.

Eleven sodium density profiles have been selected within one hour of night observations, choosing extreme cases of highly structured density profiles as shown in Figure 23. The profiles are not entirely contained in the maximum sub-aperture FoV, so a spot truncation unavoidably occurs. This condition permits us to test the idea of a device which monitors the sodium temporal evolution and, talking to the AO system, changes the LGS reference altitude according to the number of significant sodium density structures. Following the criteria of keep the maximum number of density major peaks inside the sub-aperture FoV, such a tool could:

- prevent spurious aberrations, especially if a large spot truncation is foreseen.
- provide consistent statistic of sodium density profiles that might correlate with AO system performance.

Figure 24 shows the total RMS WFE related to 11 sodium density profiles in the cases where, in principle, we can (green) and cannot (red) use a real-time density monitor tool. To understand the working condition of the tests, we must refer to Figure 23. If we could know the complete sodium density profile, we would change the LGS reference altitude in order to reduce the truncation of density major peaks. This translates to an overall lower RMS WFE

but the results are comparable considering Zernike modes above Z_{54}. The profile variation still affects these high-order modes but it is less significant. The temporal evolution of sodium density profile introduces hundreds of nanometers of WFE and it is comparable to the impact of image truncation on the wavefront sensing accuracy (see Section 4.4). The mitigation of image truncation translates into smaller low-order aberrations. Profile variation coupled with spot truncation is very detrimental to LGS low-order wavefront sensing. We can say that a sodium density monitor is useful to mitigate the wavefront sensing risks (since it reduces the effect of truncation) but not sufficient to avoid a reference WFS, based on NGS, to measure the LGS spurious aberrations. The total RMS WFE related to sodium monitor data are also wavefronts with the minimum defocus term. In principle, we could avoid a large spot truncation and mitigate the wavefront sensing risks by using the focus error measured by the reference WFS. This is used as parameter to control the LGS focus mechanism in order to change the LGS reference altitude.

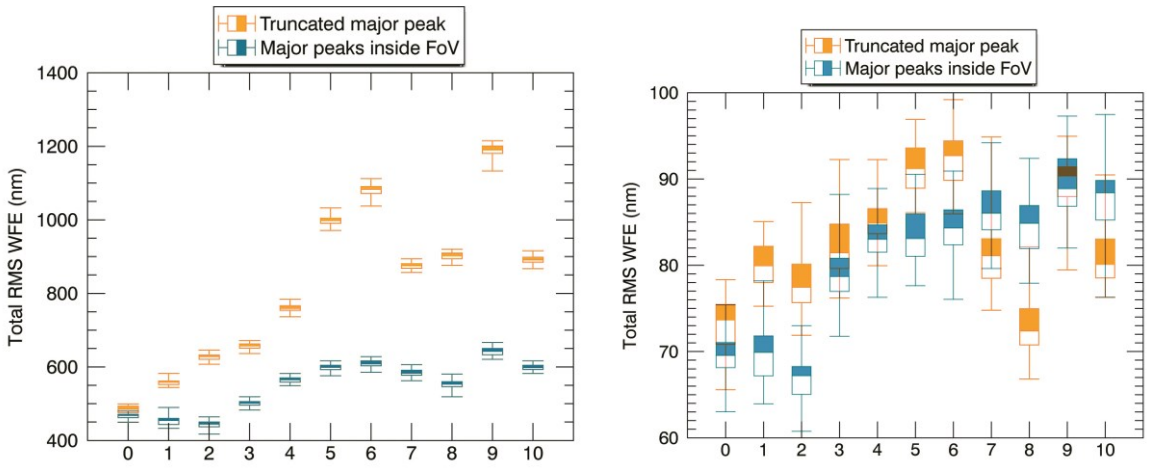

Figure 24 : WCoG algorithm results described in Section 4.6. Upper plot: Total RMS WFE above Z_4; Lower plot: Total RMS WFE above Z_{54}. Each boxplot refers to a static sodium density profile that is different for each point of the plot. In blue: Applied principle of sodium density monitor; In orange: Not applied principle of sodium density monitor that causes a large spot truncation.

4.7 Conclusions

This paper reported some laboratory experiments realised to verify the performance of LGS wavefront sensing with a SH-WFS under different working conditions. The precision of the WFS performance using WCoG centroiding was evaluated across a range of SNR representative of LGS-AO facilities with current laser technology in the case of 40m class telescopes.

Besides, three main LGS features affect the wavefront sensing as follows:

- The LGS image truncation introduces spurious aberrations whose magnitude depends on the level of spot truncation. These aberrations mainly fall within the first 60 Zernike modes and can be controlled by a reference WFS based on NGSs. To mitigate the wavefront sensing risks, the focus error, measured by the reference WFS, can be used to control the LGS reference altitude avoiding a large image truncation.
- The sodium layer temporal evolution has the same impact of image truncation on wavefront sensing accuracy. It can be controlled by the reference WFS on timescale longer than atmospheric turbulence but short enough to monitor the sodium density profile variation.
- The LGS image under-sampling is critical. It could be useful to avoid spot truncation in a SH-WFS but a mitigation error strategy has to be implemented.

The LGS WFS experiment has allowed crucial achievements, which are briefly listed here:

- Supporting the development of a numerical simulation code for modelling the MAORY instrument for ELT. The numerical code is a much more flexible tool for designing the instrument, however the support given by this experimental work has been essential.
- Supporting the definition of the architecture of the MAORY instrument and in particular, concerning the requirements for the NGS wavefront sensing sub-system supplementing the LGS WFS.
- Supporting the definition of mitigation strategies for spot truncation / under-sampling which affect the performance of LGS WFS on ELTs.

5. MAORY optical design overview

MAORY [40] will be placed on a folded focus over the ELT Nasmyth platform, after M5 reflection. The relevant main path optical parameters are listed in Table 2. Aside from fitting into the Nasmyth platform, MAORY will be integrated in a laboratory of about 18m×12m in plant and about 12m in height.

The Post-Focal Relay Optics sub-system of MAORY re-images the telescope focal plane to the exit ports. The sub-system contains the following channels:

- Main Path Optics, which relay the telescope focal plane to the exit ports for the science instruments (MICADO and 2nd instrument as yet undefined);
- LGS Objective, which creates an image plane for the LGSs, used by the LGS WFS sub-system to measure in real-time the high-order wavefront aberrations for the MCAO mode of MAORY.

Light separation between the two channels is accomplished by a LGS Dichroic Beam-Splitter, which splits the light according to wavelengths.

The layout of the Post-Focal Relay Optics is shown in Figure 25. The layout of the LGS Objective is shown in Figure 26.

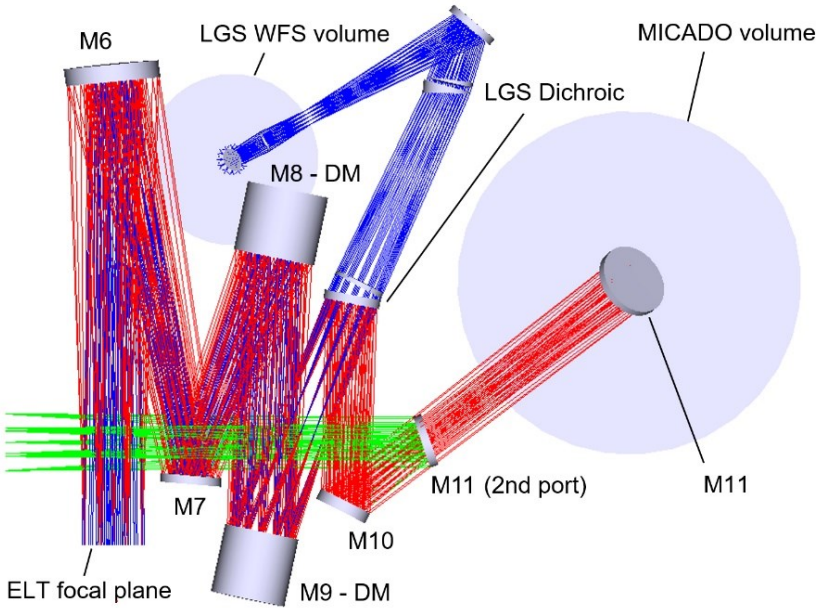

Figure 25: Post-Focal Relay Optics layout. Red rays: optical beam from telescope focal plane to exit port for MICADO. Green rays: differential path to exit port for second instrument. Blue rays: LGS path. The light-grey circles in the background are the projection of the design volumes for the LGS WFS and for MICADO.

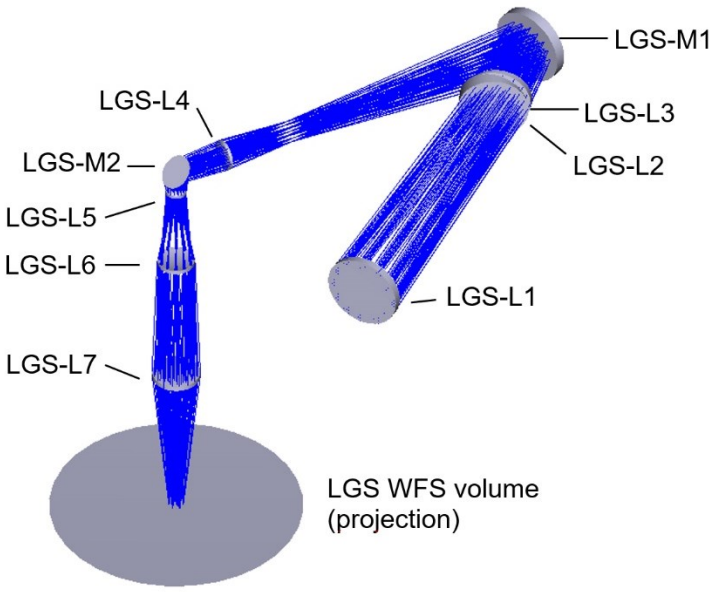

Figure 26: LGS Objective layout

Inside the optical path, two clear planes are created, optically conjugated to two different ranges from the telescope entrance pupil, allowing the insertion of up to two DMs.

The PSR optical design must also take in consideration a reasonable clearance for the mechanical mounting of the optical element.

The baseline optical design of the Main Path Optics, shown in Figure 25, consists of:

- Concave off-axis mirror (M6) and convex off-axis mirror (M7), which produce a pupil image of the appropriate size (a concave mirror alone would not be enough, given the available space between the telescope focal plane and the edge of the Nasmyth platform);
- Two concave on-axis DMs (M8 and M9), with the same optical power, optically conjugated to the required ranges from the telescope entrance pupil;
- LGS Dichroic, close to the pupil image; in the baseline design, this component is assumed to reflect the science light;
- Convex off-axis mirror (M10), which produces the exit focal plane with the required focal ratio and exit pupil distance;
- Flat 45°-tilted mirror (M11), which folds the light to the gravity-invariant port for MICADO.

The second instrument port is achieved by inserting a flat folding mirror between M10 and M11.

The combination of convex mirrors (M7 and M10) and concave mirrors (M7, M8, M9) ensures flat focal surface on the exit port.

Given all requirements and constraints, the baseline design has minimum number of optical surfaces.

Two versions of the baseline design have been studied, concerning the optical shape of mirrors M6, M7 and M10: pure conic sections and conic sections with even asphere coefficients (up to 8-th order). The latter option has significantly better performance in terms of geometric distortion. A market consultation has demonstrated that such mirrors with even asphere terms are feasible and the cost, at the present stage, is comparable to the pure conic section version. For these reasons, the design version with even asphere coefficients has been chosen as baseline.

The first order parameters of the main path optics are listed in Table 2 while the estimated performance and tolerance analysis are described in Section 6.7.

Table 2 : MAORY main path optics general specifications.

Item	**Value**
Exit focal ratio	F/17.7
Exit pupil distance	8000 mm (towards telescope)
Focal plane curvature	Flat
NGS patrol FoV (also called technical FoV)	200 arcsec diameter
MICADO science FoV	Up to 75 arcsec diameter
Transmitted wavelength range at exit port	0.6 – 2.5 µm Lower wavelength limit set by LGS Dichroic. Extension to shorter wavelengths TBC (e.g. by means of "notch" filter centred at LGS wavelength)
Post-focal DMs conjugation range	15088 m, 4411 m
Projected pitch of DMs on conjugates	2 m, with inter-actuator spacing of ≈ 30 mm

The next table shows the optical prescription data of the Main Path Optics. Concave surfaces are labelled as "cv"; convex surfaces as "cx". The sign convention for the radii of curvature is: positive if the centre of curvature is to the right from the surface vertex, negative if the centre of curvature is to the left of the surface vertex.

Mirrors M8 and M9 are described here as two rigid mirrors, but they are two DMs in the MAORY Post-Focal Relay. They have identical curvature radius and slightly different conic constant. The slight difference in optical shape, as well as the deviation from the best fit sphere, is in the order of only 2-3 µm peak-to-valley and may be probably applied by active deformation of the surface.

Table 3. Main Path Optics optical prescription data.

ID	**Diameter [mm]**	**Surface decenter [mm]**	**Curvature radius [mm]**	**Conic constant [1]**	**Aspheric terms**
M6	1200	427	+14458 (cv)	-2.3965	4^{th}: 3.007e-14 6^{th}: 5.612e-21 8^{th}: -3.579e-27
M7	750	918	+7874 (cx)	-1.3591	4^{th}: 2.924e-14 6^{th}: 3.260e-21 8^{th}: -1.039e-27
M8 – DM	945	-	+15042 (cv)	-6.7009	-
M9 – DM	860	-	-15042 (cv)	3.9175	-
LGS Dichroic	680	-	Infinity	-	-
M10	675	362	+42342 (cx)	-0.0959	4^{th}: 7.735e-13 6^{th}: -3.480e-19 8^{th}: 2.449e-25
M11	900x690	-	Infinity	-	-

The tilt angle between the DMs surfaces and the optical axis is the minimum angle to avoid interference of the next optical element with the optical beam. This tilt causes different parts of the mirrors to be conjugated at different altitudes, respect to the nominal conjugation height. Due to the range mismatch, a given DM actuator appears "out-of-focus" with respect to the layer (Figure 27). Given a de-magnification factor *m* between the ELT metapupil and MAORY DM diameter D_{dm}, the layer maximum mis-conjugation Δh depends by the DM tilt angle θ :

$$\Delta h \approx (D_{dm}/2) \cdot \text{sen}(\theta) \cdot m^2$$

This mis-conjugation generates a blur that must be smaller than the projected actuator spacing.

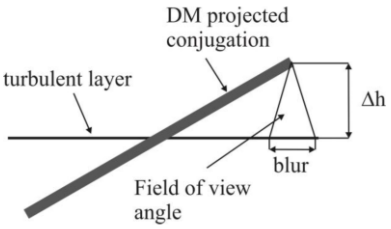

Figure 27 : The deformable mirror conjugate plane is tilted with respect to the turbulence layer.

The post-focal DMs are conjugated to these ranges from the telescope entrance pupil:

- H = 15088 m ± 226 m
- H = 4411 m ± 171 m.

An actuator at the edge of the DM, because of the quoted "errors" or "mis-conjugations", is seen from the nominal conjugated layer under an angle ≤ 200 arcsec (the NGS patrol FoV), which corresponds to a projected blur diameter of

- $9.7 \cdot 10^{-4}$ rad x 226 m ≈ 0.22 m, on the upper DM
- $9.7 \cdot 10^{-4}$ rad x 171 m ≈ 0.17 m, on the lower DM.

In any case, the blur diameter is in the order of 1/10 of projected inter-actuator spacing, which is deemed acceptable.

The following table includes the supplier requirements which directly affect the PFR Optics optical design. "Supplier" stands for the MAORY consortium or for the MICADO consortium.

Table 4. Supplier requirements for Post-Focal Relay Optics optical design.

ID	Requirement description	Rationale	Derived from
1.	Main Path Optics possibly based on all-reflective design	Avoid chromatic effects and large refractive elements, which are difficult to manufacture	MAORY System
2.	Main Path Optics to be designed with minimum number of surfaces	Maximise throughput and minimise thermal emissivity	MAORY System
3.	Post-Focal Relay Optics shall include LGS dichroic beam-splitter	Separate LGS light from science light, to feed LGS WFS sub-system	MAORY System

4.	LGS dichroic beam-splitter shall preferably reflect IR light	Avoid issues with substrate material when transmitting IR light Avoid chromatic effects on science exit port	MAORY System
5.	DMs shall have optical power	Exploiting optical power on the DMs is helpful to minimise number of surfaces	Req. 2
6.	DMs shall have same optical power	To ease manufacturing and reduce costs	MAORY System
7.	DMs shall have optical diameter in the range 750-850 mm	Smaller diameter, associated with required FoV, implies off-axis optics with short focal ratio, which shall be avoided for easiness of manufacturing. This diameter range is similar to DMs with high TRL; already used in other projects (e.g. LBT, VLT)	MAORY System
8.	DMs conjugation range	H (high DM) > 15000 m H (low DM) > 4000 m	MAORY System
9.	DMs optical conjugate tilt shall be as small as possible	Avoid affecting MCAO compensation	MAORY System
10.	DMs optical conjugate image quality 1/10 actuator spacing	Ensure good wavefront compensation	MAORY System
11.	Post-Focal Relay Optics size in plant < 8 m	Fulfil allocated design volume	MAORY System
12.	MICADO exit port position w.r.t. telescope focal plane: X = 3050 mm Y = 6000 mm	Provide convenient mounting location for MICADO	MICADO
13.	MICADO exit port shall be gravity invariant	Ensure mechanical stability of MICADO (this is particularly important to achieve required astrometric performance)	MICADO
14.	MICADO focal plane height 1800 mm below telescope optical axis	Leave enough vertical clearance for MICADO and for MAORY NGS WFS sub-system	MAORY System / MICADO
15.	Second instrument port position should be on opposite side of MAORY Bench with respect to MICADO	Ensure accessibility to both MICADO and second instrument	MAORY System / MICADO

16.	Second instrument port back-focal length shall be outside MAORY envelope	Ensure for second instrument accessibility to focal plane	MAORY System
17.	Lateral clearance (orthogonal to optical axis) for second instrument port shall be at least 4000 mm	Ensure appropriate design volume for second instrument	MAORY System
18.	Clearance around optical elements shall be > 100 mm	Ensure accessibility	Post-Focal Relay Optics
19.	Clearance around DMs shall be > 150 mm	Ensure accessibility	Post-Focal Relay Optics
20.	Clearance behind mirrors shall be > 300 mm (measured from optical surface)	Ensure accessibility	Post-Focal Relay Optics
21.	Clearance behind DMs shall be > 800 mm (measured from optical surface)	Ensure accessibility	Post-Focal Relay Optics
22.	LGS dichroic size shall be significantly smaller than 1 m	Ensure manufacturability	Post-Focal Relay Optics
23.	Focal ratio on MICADO exit port F/17.7	Same as telescope	MICADO
24.	Exit pupil position on MICADO exit port > 8000 mm toward telescope	Different from telescope exit pupil position, but acceptable for MICADO	MICADO
25.	Exit focal plane curvature radius > 9900 mm	Field curvature not larger than telescope's	MICADO
26.	NGS patrol FoV shall be ≈ 200 arcsec diameter (TBC)	Ensure large patrol FoV for sky coverage	MAORY System
27.	WFE on MICADO FoV (nominal value) < 30 nm RMS	Ensure diffraction-limited optical quality (with margin for tolerancing)	MAORY System / MICADO
28.	WFE on NGS patrol FoV < 100 nm RMS	Avoid large off-axis aberrations, which need to be calibrated	MAORY System
29.	Differential geometric distortion on MICADO entrance focal plane < 8 µm for a field rotation of 2.6°	Ensure stability of NGS image over astrometric exposure	MAORY System / MICADO
30.	Geometric distortion after transformation of n-th order (n TBD) < 20 micro-arcsec (TBC)	Ensure achievement of relative astrometric requirement	MAORY System / MICADO
31.	Tolerable NGS motion due to geometric distortion < 1.8 mas	Avoid field warping by MCAO	MAORY System / MICADO

32.	Exit pupil optical quality (ellipticity and blur) on MICADO FoV < 1/100 pupil diameter	Pupil blur shall be small to avoid unwanted thermal background through MICADO cold stop	MICADO
33.	Exit pupil optical quality (ellipticity and blur) on NGS patrol FoV < 1/400 pupil diameter	Ensure pupil quality for LOR WFS	NGS WFS Module
34.	LGS Objective focal ratio F/5	Reduce focus offset of LGS w.r.t. zenith angle	LGS WFS
35.	LGS Objective exit pupil at infinity	Avoid exit pupil diameter variation w.r.t. zenith angle	LGS WFS
36.	LGS Objective exit pupil quality (ellipticity and blur) < 1/1600 pupil diameter	Ensure pupil quality for LGS WFS	LGS WFS
37.	LGS Objective wavefront error as small as possible. Goal < 200 nm RMS (TBC).	Avoid large spot offsets in LGS WFS sub-apertures. Remove residual aberrations by means of calibrations/look-up table, with 80-90% level accuracy.	MAORY System / LGS WFS

5.1 Main path Optics geometric distortion

Geometric distortions from the Main Path Optics are asymmetric. As the imaged sky rotates with respect to the optics during an exposure, the PSF of a point-like source on the exit focal plane follows an imperfect trajectory, which may be described as an arc of a circle, with small perturbations due to the geometric distortions from the optics. Field de-rotation only compensates for the circular part of the trajectory. The residual deviations from a circular trajectory have different effects, which are described in Section 6.

5.1.1 PSF blur due to geometric distortion

On the MICADO FoV, the residual motion of the PSF, when integrated over a finite exposure time, translates into PSF blur. A technical requirement (#29 of Table 4) has been agreed with MICADO and is described in the following:

- T = Maximum integration time for narrow band astrometric observations ≈ 120 s
- A = Maximum de-rotator angular velocity ≈ 13.7 x (1/cos(80°)) ≈ 79 arcsec/s
- T x A ≈ 2.6°

- During this rotation, the FWHM of the long-exposure PSF due to the MAORY optics should not increase by more than 1/10 of its nominal value.
- For wavelength $\lambda = 1$ μm, the amount of distortion shall be < 8 μm at the MAORY exit focal plane on the MICADO FoV (F/17.7 focal ratio).

5.2 LGS Objective design

The LGS light propagated through mirrors M6, M7, M8 (DM) and M9 (DM) is transmitted by the LGS Dichroic, which is located closed to a pupil plane, and is focused by the LGS Objective to create an image of the 6 LGSs for the LGS WFS sub-system.

The general specifications of the LGS Objective are reported in the next table.

Table 5. Main Path Optics general specifications.

Item	**Value**
Operating wavelength	0.589 μm
LGS range to be re-imaged	80 – 240 km
Exit focal ratio	F/5
Exit pupil distance	Infinity
LGS constellation maximum angular diameter	120 arcsec

The LGS Objective is designed to deliver LGS images in the altitude range 80 - 240 km. The output focal ratio of F/5 allows reasonable motion of the exit image plane, as a function of Zenith distance variation during the observation.

The 6 LGSs are supposed to be launched form the edge of the primary mirror and thus they rotate as the Zenith angle of observation. Their image plane shifts along the optical axis due to the variation of the mean distance of the LGS from the telescope, as $h_{Na}/\cos(\theta)$, where $h_{Na} \approx 90$ km is the sodium layer mean altitude above the ground.

The LGS Objective, shown in Figure 26, consists of three wedged lensed (the wedge is on a plane surface so that these lenses may in principle be replaced by normal lenses plus wedges), a powered mirror, a flat mirror and four lenses. The baseline material for all refractive elements is optical glass (BK7, S-BSL7 or equivalent glass).

The LGS Objective contains an intermediate image plane and an intermediate pupil plane. The last part of the optical axis is folded by the flat mirror LGS-M2, so that the LGS WFS sub-system is mounted in gravity invariant configuration.

The next table shows the prescription data of the optical elements in the LGS Objective. Detailed performance and tolerance analysis of the LGS Objective is shown in Section 6.9.

Table 6. Prescription data of optical elements in the LGS Objective. When two values are contained inside a single row, they refer to the front and rear surface of the optical element.

ID	**Diameter [mm]**	**Thickness [mm]**	**Radius [mm]**	**Conic constant [1]**	**Wedge**
LGS-L1	660	61	Infinity (cx) 8946	- -10.000	yes
LGS-L2	600	55	Infinity (cv) 3234	- -	yes
LGS-L3	580	55	(cx) 1830 Infinity	-0.827	yes
LGS-M1	620	-	(cv) 23516	-4.605	-
LGS-L4	380	41	(cx) 1585 (cx) 641	- -4.709	-
LGS-M2	420	-	flat	-	-
LGS-L5	240	21	(cx) 109 (cv) 76	-1.258 -1.007	-
LGS-L6	340	48	(cv) 666 (cx) 331	-0.018 -0.260	-
LGS-L7	420	63	(cx) 1376 (cx) 1475	-1.625 -2.866	-

6. Tolerancing MAORY PFR

Tolerance process of optical systems is one of the most important step in the instrument design since it involves complex relationships across fabrication, assembly and alignment of the system. The tolerance analysis is intended to ensure that MAORY requested performances are satisfied when the final assembled instrument is operative. At the end, the assignment of tolerances to the various opto-mechanical parameters should be a trade-off between final cost of the system and its resulting performances.

The guiding philosophy in establishing tolerances should be to set a tolerance as large as the performance requirements of the optical system will permit.

This section describes the logic behind the tolerance analysis starting from definition of quantitative figures of merit for MAORY requirements and ending with estimation of MAORY performances perturbed by opto-mechanical tolerances.

The method used to estimate tolerances takes care of compensation of errors during assembly/alignment procedure and uses a RSS merit function to combine independent error contributions.

One possible way to establish a tolerance budget using this principle is as follows:

1. Select a preliminary tolerance budget. Table 7 can be used as a guide to appropriate tolerance values.
2. Perform the sensitivity analysis. (Described in Section 6.7).
3. Compute RSS for all the aberrations for each individual tolerance. This will indicate the relative sensitivity of each tolerance.
4. Compute RSS for all the effects calculated in step 3 combined.
5. Compare the results of step 4 with the performance required of the system.
6. Adjust the tolerance budget so that the result of step 5 is equal to the required performance. Since the larger effects dominate the RSS, tight the most sensitive tolerances. Conversely, one should be sure that the tolerances are not tightened beyond a level at which fabrication becomes impossible.
7. After one or two adjustments (steps 2 through 6) the tolerance budget should converge to one which is reasonable economically and which will produce acceptable performances. If the tolerances necessary to get acceptable performances are too tight to be fabricated economically, one way to ease the situation is to add compensators

and set allowable ranges for the compensators: they can be adjusted to minimize the aberrations. The default compensator is the back focal distance, which controls the position of the image surface.

There are two requirements that limit the allowable changes of opto-mechanical parameters. The mean RMS WFE and the optical distortion. The first one must satisfy diffraction limit performance over the MICADO FoV while the second one must satisfy high astrometric accuracy and precision.

Considering a narrowband filter, within a single exposure, MICADO can integrate for 120 seconds. Considering a zenith avoidance of 10º, the maximum field rotation is ≈79 arcsec/s at ELT site latitude. During this rotation, the FWHM of the long-exposure PSF due to the MAORY optics should not increase by more than 10% of its nominal value. This means, for wavelength $\lambda = 1$ μm, the amount of distortion shall be < 8 μm at the MAORY exit focal plane (assuming F/17.7 focal ratio).

Relative field distortion residual, over all timescales in the range of 1 hour to 5 years, shall be < 50 μas (goal <10 μas) in a 20'' FoV (goal 53'' x 53'' FoV) after n^{th} order transformation, comprehending all error sources.

Considering the RMS WFE, the objective was to maintain a maximum difference respect to the nominal design below 30%. The allowed change is a 'rule of thumbs' for the AO systems tolerance analysis and keeps the system below the diffraction limit of MICADO FoV.

Few words should be spent regarding the error sources in astrometry from a purely opto-mechanical point of view. A full discussion of the final astrometric accuracy is beyond the scope of this Thesis and is addressed at system-level.

6.1 Opto-Mechanical astrometric errors

MAORY/MICADO astrometry requires observations to be taken at different epochs in order to detect motions of astronomic sources, either with the motions of the science objects relative to each other or with respect to the sky coordinate system (or both). There are two categories of astrometric observations:

1. Intra-epoch observations are those for which the science and/or references objects can be considered stationary. If motions of science objects were detected, they would be caused by measurement errors. In general, intra-epoch observations are used to

increase the SNR and accuracy of the measurements and, potentially, to estimate the errors and uncertainties of the measurements.

2. Inter-epoch observations are those for which the science and/or reference objects cannot be considered stationary. These are the observations used to determine the motions of science objects.

Distortions due to opto-mechanics cause astrometric errors that can be major contributors to the astrometry error budget. Designing MAORY is extremely important to minimize system distortions that could have effect on the relative astrometry accuracy. Given a FoV, the term 'relative astrometry' refers to measurement of different science objects separations relative to each other or relative to other field objects. These measurements have to be converted in sky coordinates to be scientifically useful and that's the aim of 'absolute astrometry'. From an opto-mechanical point of view, in terms of calibrations, we are interested only on object separations relative to each other rather than their positions in the sky.

Considering the MAORY optical design, it is not possible to keep distortions at or below the level of accuracy required for relative astrometry. Even if the optics were perfectly built, the distortions present in the system would be orders of magnitude larger than micro-arcsec scale and a calibration procedure is required to achieve the micro-arcsec magnitude.

If distortions are either stable in time or vary in a deterministic way can be measured and calibrated before or after the science observations. This is usually done by observing a field of calibration sources, such as a pinhole mask inserted into the MAORY focal plane or a dense star field. A distortion calibration solution is then calculated from these measurements.

Errors related to this calibration solution depends on the SNR of the measurement, the number of calibration sources and the stability of the distortions. Multiple configurations of MAORY/MICADO must be taken into account and the calibration process must be repeated for each different configuration. At the time of observations, the calibration solution has to be interpolated to the observational conditions.

The residuals of this solution are:

- distortions not sensed and/or introduced by the telescope
- uncertainties and errors in the repeatability of the configuration
- variability of distortions
- uncertainties and errors due to the interpolation between different configurations

- common-path distortions of spatial or temporal frequency too high to correct for MAORY (e.g. HO irregularities of optical surfaces)
- non-common path distortions.

Residual distortions can be considered partially systematic during intra-epoch observations, while for inter-epoch observations they can be considered random realizations. Thus, they could be average out as the root square of number of inter-epoch observations.

The current MAORY optical design has distortions of up to tens milli-arcsec at the edges of the field. These distortions are calibrated using a pinhole grid that is inserted into the MAORY focal plane. We have performed detailed simulations of this process, testing a variety of grid configurations, which show that it is possible, albeit not easy, to measure these distortions to a sufficient level to fulfill the MICADO science requirements.

Results of Section 6.7 show that 12 μarcsec of static distortion residuals on average (RMS) across the MICADO field can be achieved after calibration with the grid and after removal of plate scale distortions in post-processing (see below for an explanation of the latter).

It is not necessary (nor possible, in fact) to know the positions of the pinholes on the grid to this same accuracy, which is of the order of nanometers at MAORY entrance focal plane, by measuring them with microscopes or similar instruments.

6.2 Plate scale errors due to NGS position measurement errors

In MCAO, the position of the NGSs on the NGS WFS focal plane fixes the plate scale. If the FoV is affected by optical distortion, it will introduce a differential TT (shift) of the NGS constellation respect to the nominal on-sky position. This translates into local plate scale distortions that will affect and potentially destroy the astrometry [41]. The effect, if not properly calibrated, could be the worst offender to astronomy performance when dithering or, in general, when the telescope pointing is different. Because of static optical distortion, the relative distance between the NGSs changes when the whole constellation is translated in the NGS WFS focal plane affecting the plate scale on the science image. There are a total of three plate scale modes: plate scale stretched in X and Y, respectively, and shear. Thus, if three or more reference objects are available in the field, it is possible to use them to calibrate the plate scale error. If the NGSs are used as refences, differential flexure between the probes will introduce the same kind of error as the optical distortion. These errors could be defined as positioning errors and has to be properly calibrated.

6.3 MAORY optical surface error calibration residuals

During the tolerance analysis, the irregularities and imperfections of the optical surfaces in MAORY where evaluated on the order of a few to tens of nanometers RMS. These irregularities cause distortions that are large compared to the relative astrometry error budget requirements.

Considering different field points, their beam footprints overlaps differently on each MAORY mirror surface. As the field rotates during the observations, the beam footprints cross the static errors on each mirrors surface. The lower is the overlap of different footprints, the bigger is the difference in terms of irregularities introduced in each optical trail relative to a given field point. As the optical footprint on a surface is the smaller the farther the surface is from the pupil plane, this error is largest for the surfaces with the largest conjugate ranges. For MAORY, this means that it is largest for the instrument selection mirror (M11) followed by the first mirror after the entrance focal plane (M6).

Our results show that 12 μarcsec residuals should be achievable with realistic requirements for the surface qualities and calibration time (see Section 6.7). This is not a hard limit as it can be reduced with on-sky observations of more objects and/or for longer times. The errors depend on the relevant length scales in the science field, and thus, for relative astrometry science case with a very small field, might be smaller than the 12 μarcsec assumed here.

There is an additional error due to random or systematic beam wander/translation across the static errors on each surface. Such beam wander can, for example, be caused by instrument boresighting errors and image de-rotation.

6.4 Telescope optics calibration residuals

The shapes, alignment and optical surface errors of the five telescope mirrors all cause distortions. Alignment errors are mostly low order and will be removed by MAORY. Shape and surface errors of the telescope mirrors have been investigated separately and they have qualitatively the same effect as the MAORY distortions described above. As the footprint overlap of the beams on the telescope mirrors is orders of magnitude larger than on the MAORY - M11 mirror, residual distortions from the telescope mirrors are smaller. Besides, even the footprint diameters are orders of magnitude larger than other MAORY optics and thus the effect of beam wander is much smaller.

Their residual high-order component is foreseen to be included in the calibration solution derived from on-sky calibration observations.

6.5 De-rotator errors

Rotator errors enter through two effects, the difference between the assumed and real rotator angle, and the (small, but non-negligible) misalignment error between the rotation and optical axes, which causes the beam footprint to wander on the optics.

The rotation angle error needs to be treated differently as it does not produce its own distortion but a rotation of part of the already existing distortion, and therefore an additional calibration error. This rotation can partially be eliminated, for low-order distortions, through coordinate transformations in fields with many objects, but might need to be considered for absolute astrometry and in sparse fields and its high spatial frequency distortion content needs to be investigated. Also, if the rotation error varies during an exposure, this causes image motion with all the effects that go along with it (reduction of Strehl, PSF elongation and coupling with variable effects).

6.6 MAORY Main Path Optics tolerance analysis: starting point

The sensitivity analysis on system performances considers each tolerance individually and, defined a merit function, the introduced errors are combined by RSS to find the net effect of all the tolerances on the system. In terms of WFE, the sensitivity is basically the partial derivatives of the aberrations with respect to the tolerances (curvature, asphericity, thickness, surface quality, etc.) multiplied by the individual tolerances.

In general, the estimated error by RSS is:

$$E = \sqrt{E_o^2 + \sum_i \left(\frac{\partial E_i}{\partial x_i}\Delta x_i\right)^2}$$

Where E_0 is the nominal error and the sum is taken over the sensitivity of a single parameter $\partial E_i/\partial x_i$ due to its tolerance Δx_i. This method assumes that errors introduced by each individual tolerance are statistically uncorrelated. Additionally, it does not assist in defining what the

tolerance values should be. Instead, it provides a translation between error limits and performance degradation.

The analysis allows to identify parameters which are highly sensitive to certain errors, such as surface curvature radii or decentres and it is also valuable to find the optimum number of compensators for required adjustments. The sensitivities related only to available DOF can be also used during the alignment phase of the instrument. In fact, the system requires an accurate inspection to the type of aberrations that are introduced by each DOF in order to choose the most effective DOF to be used as compensators during the alignment (Section 7).

Table 7 : Typical manufacturing tolerance chart (credit: Optimax Systems, Inc.)

Attribute	**Commercial**	**Precision**	**High Precision**
Glass Material (n_d, v_d)	±0.001, ±0.8%	±0.0005, ±0.5%	Melt Data
Diameter (mm)	±0.00/-0.10	+0.000/-0.025	+0.000/-0.015
Center Thickness (mm)	±0.150	±0.050	±0.025
SAG (mm)	±0.050	±0.025	±0.015
Clear Aperture	80%	90%	90%
Radius (larger of two)	±0.2% or 5 fr	±0.1% or 3 fr	±0.05% or 1 fr
Irregularity – Interferometer (fringes)	2	0.5	0.2
Irregularity - Profilometer (µm)	±10	±1	±0.5
Wedge Lens (ETD, mm)	0.050	0.010	0.005
Wedge Prism (TIA, arc min)	±5	±1	±0.5
Bevels (face width @ 45°, mm)	<1.0	< 0.5	< 0.5
Scratch - DIG (MIL-PRF-13830B)	80 - 50	60 - 40	20 - 10
Surface Roughness (Å rms)	50	20	10
AR Coating (R_{Ave})	MgF_2 R < 1.5%	BBAR R < 0.5%	V-coat R < 0.2%

At the time of writing, two optical design are object of study. They manly differ from having pure conical mirrors or non-zero aspherical terms for mirror surfaces. The light through the science path of MAORY is shown in Figure 25. In the alternative design, all mirrors except the two DMs (M8 and M9) and M11 are even aspheric surfaces with non-zero coefficient until the 8th order. The two DMs (M8 and M9) should be intended as rigid mirrors for the scope of this paper. In fact, in a partial implementation of the instrument, at least the DM M9 would be replaced by a rigid mirror. Moreover, it is of interest to evaluate the feasibility of mirror M8, for instrument test purposes.

Before a detailed description of tolerance analysis, the two optical design options were compared, in terms of nominal performances, by following the criteria listed here:

1. WFE in the circle containing MICADO FoV (75” diameter)
2. WFE in the NGS FoV (annular, 180” < FoV < 75”)
3. Astrometric residual error after the 3rd and 4th (5th if needed) order coordinates transformation in the circle containing the MICADO FoV (for a range of field rotations)
4. Star centroids movement after the maximum rotation for a single astrometric image in the circle containing the MICADO FoV
5. Star centroid movements due to optical distortion in the NGS FoV (for a range of field rotations)

The two designs have a very similar RMS WFE in terms of absolute values. The off-axis mirrors are decentred and tilted in one axis only, hence the WFE map is symmetric along the other axis. RMS WFE maps of MICADO FoV and NGS FoV are shown in Figure 28. They refer to MAORY design with even aspheric terms for mirror surface.

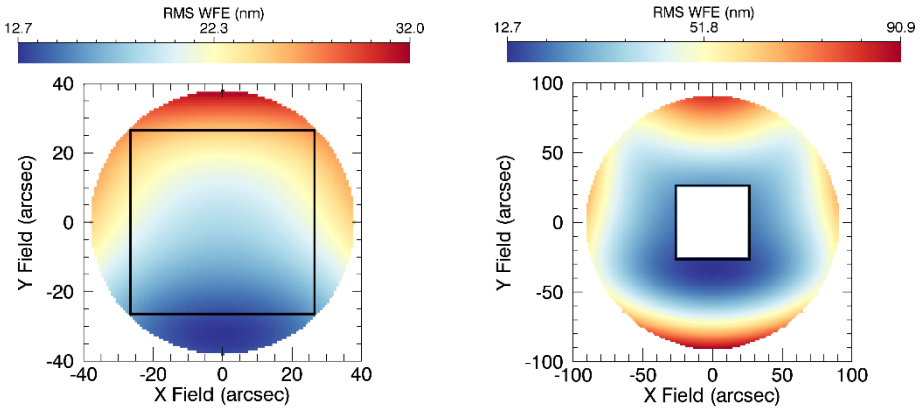

Figure 28: RMS WFE maps of MICADO FoV (left) and technical FoV (right). The black square is the 53”x53” MICADO FoV

Optical distortion is the main difference between the two designs. Figure 29 shows (for both designs) the star centroids movements in the MICADO FoV for 120 seconds of single exposure.

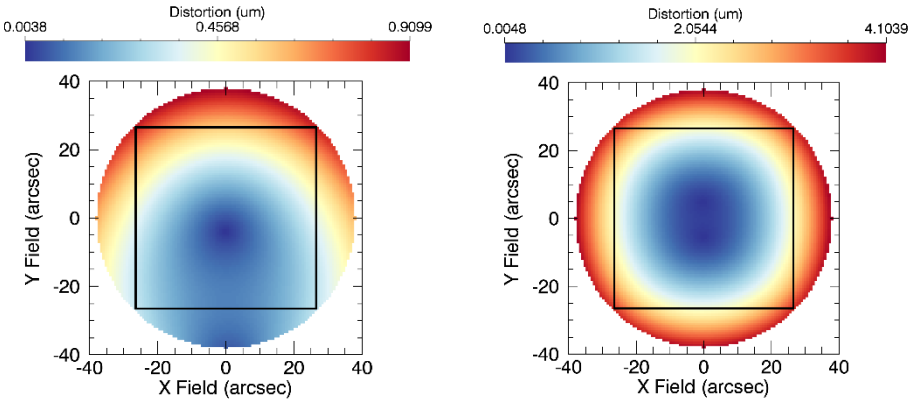

Figure 29: Star centroids movement for a single astrometric image in the circle containing the MICADO FoV (black square). Left plot refers to the design with even aspheric terms for mirror surfaces. Right plot refers to pure conical mirrors

In two different astrometric exposures, the images of a given source in the MICADO FoV are in slightly different positions, because of the non-central-symmetric distortion pattern. The typical calibration procedure adopted in astrometric observations with MICADO is that any two astrometric images are transformed onto each other by an astrometric transformation (e.g. polynomial transformation of n^{th} order, TBC), using field sources to determine the coefficients of the transformation. This implies that "low-order" distortions (of order ≤ n in the example adopted here) are corrected on the data themselves, while "high-order" distortions need to be small enough, in order to avoid complex calibration procedures based on look-up tables.

In order to analyse this effect, a regular grid of stars on the MICADO FoV has been used to evaluate the astrometric residual error. Let (X_{inp},Y_{inp}) be the initial coordinates of the stars centroids, (X_o,Y_0) the coordinates of the stars centroids for a given FoV rotation angle, (X,Y) the corrected stars centroids according to a n-th order polynomial transformation of the form:

$$X = \Sigma_{i,j}\, Kx_{i,j} \cdot X_o{}^{i} \cdot Y_o{}^{j}$$

$$Y = \Sigma_{i,j}\, Ky_{i,j} \cdot X_o{}^{i} \cdot Y_o{}^{j}$$

Typical order of transformation is n = 3, 4, 5; the order indicates the maximum of the sum of the power i and j in the equations above. $Kx_{i,j}$ and $Ky_{i,j}$ are (n+1)x(n+1) coefficients used to model the distortions introduced by the optics for a given FoV rotation angle. The corrected coordinates (X,Y) have been compared to (X_{inp}, Y_{inp}) in order to compute the standard deviation of residual errors. The final error in the position is the standard deviation computed as the quadratic sum of the X and Y error.

Figure 30 shows the residual errors vs. field rotation angles; for each angle, a single astrometric exposure has been assumed with exposure time of 120 seconds. Residual errors have been computed for an astrometric transformation of order n = 3 and n = 4. The errors are < 1 μas for all rotation angles when n = 4, well within the requirement reported in Table 4.

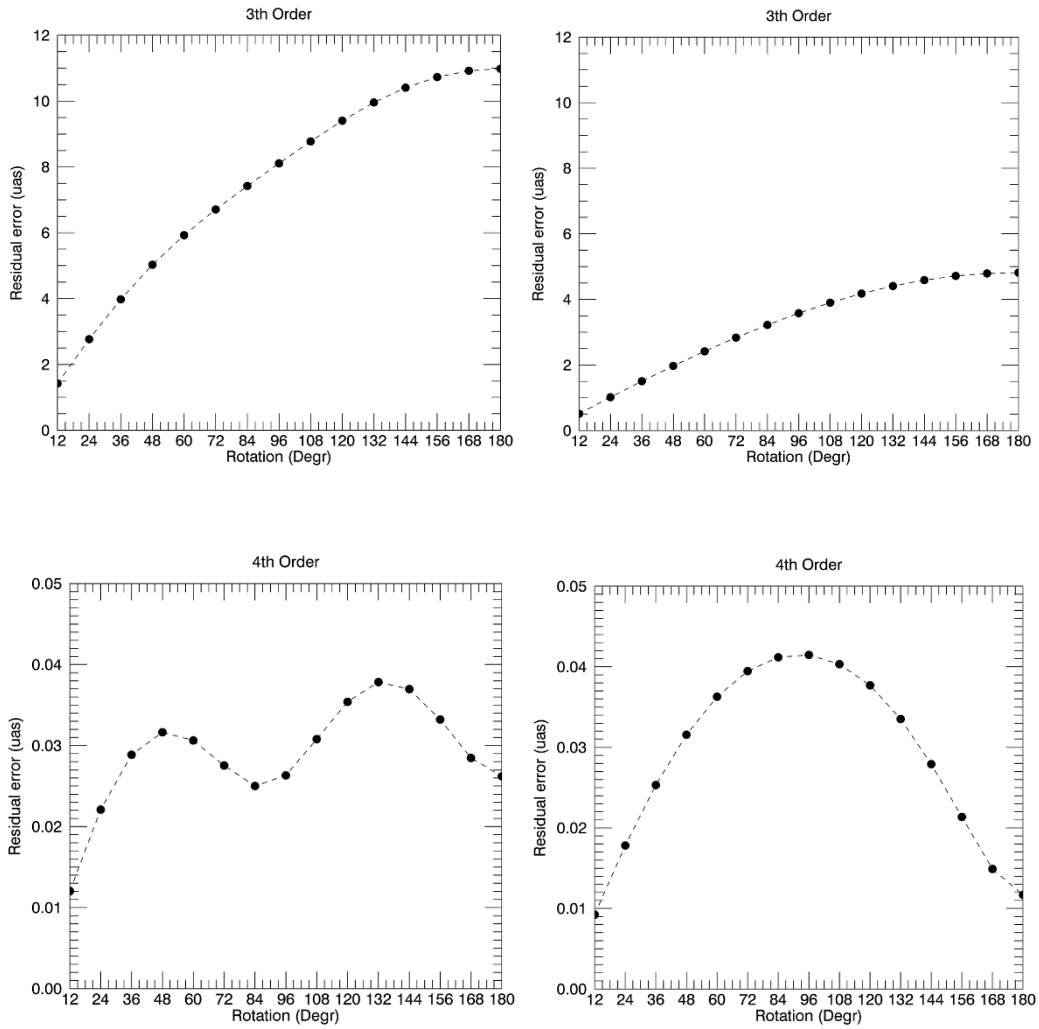

Figure 30: Astrometric residual errors for a range of field rotations in the circle containing the MICADO FoV. The error is the standard deviation computed as the quadratic sum of the X and Y error. First row: 3rd order polynomial fit. Second row: 4th order polynomial fit. First column: design with even aspheric terms for mirror surfaces. Second row: design with pure conical mirrors

Positioning errors of the NGS WFS probes are propagated by the MCAO system, producing science field warping effects. Astrometric images are calibrated according to the procedure previously described. The residual errors shall be within the requirement defined in 4.

One of the sources of positioning error of the NGS WFS probes is the geometric distortion for the Main Path Optics. If the NGS WFS probes are positioned on the respective stars at the beginning of a sequence of astrometric exposures, in the course of the sequence the stars will

drift with respect to the probes, because of the non-rotational part of the geometric distortion itself. The tolerable positioning error is < 1.8 mas (Table 4). Figure 31 shows stars centroids movements due to optical distortion in the NGS patrol FoV. Of course, no calibration is applied in this case. The analysis summarised by the plots in Figure 31 has the purpose to define under which observational conditions the NGS WFS probes have to be re-positioned according to a pre-calibrated look-up table, in order to bring the NGS drift below the required level in a sequence of astrometric exposures. The observational conditions depend of course on the NGS position in the patrol FoV and on the length (in terms of overall sky rotation) of the sequence of astrometric exposures.

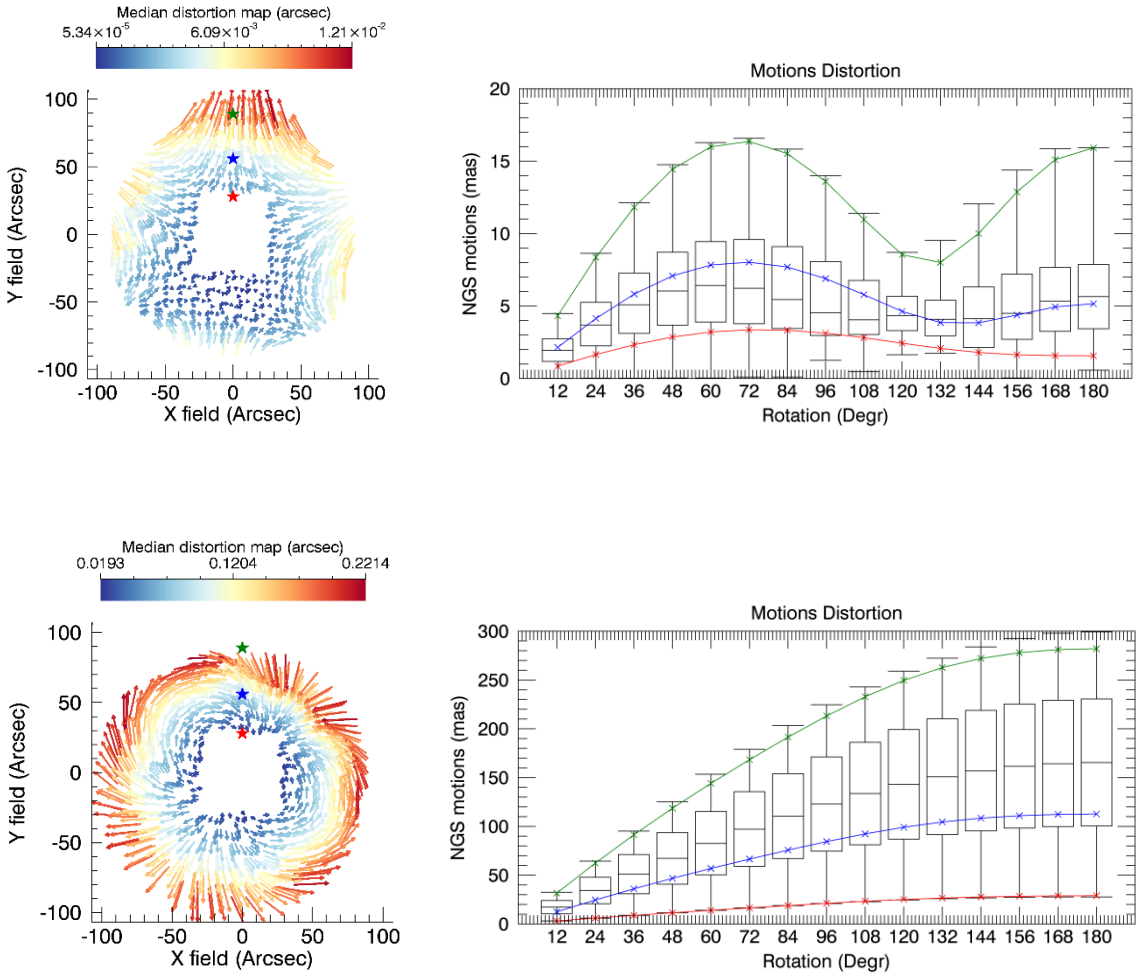

Figure 31: Star centroid movements (for a range of field rotations) due to optical distortion in the NGS FoV. First row refers to the design with even aspheric terms for mirror surfaces. Second row refers to pure conical mirrors. Distortion maps on the left are median of the considered field rotation angles. Box plots on the right show minimum and maximum values and quartiles of star centroid movements in the FoV.

6.7 Main Path Optics tolerance analysis

As criterion for tolerancing, the defined merit function considers the RMS wavefront referred to star centroid and adds boundary constraints on the compensators and geometric distortion in MICADO FoV as described in Section 5.1.1.

The tolerance analysis has been broken down into 4 blocks that consider different error sources of the optical elements:

Block 1: Curvature radii, conic constants and, if present, aspheric terms

Block 2: Low order RMS surface irregularities (from Zernike 4 to Zernike 11)

Block 3: High order RMS surface irregularities (form Zernike 12 to Zernike 120)

Block 4: Alignment errors

Each block introduces a certain amount of performance degradations despite the considered MAORY design with or without even aspheric terms for mirror surface, hence the computed tolerance values are equal for both designs.

The first two blocks listed above, are supposed to be compensated by a design re-optimization or during the instrument alignment.

Block 3 is a worst offender for astrometric requirements and needs a dedicated calibration process to fulfil desired performances.

Block 4 is strictly related to mechanical accuracy and precision of optical mounts.

To evaluate the impact of tolerances on astrometry, a Monte Carlo simulation is mandatory. This simulation generates a series of random systems which meets the specified tolerances. It is a realistic simulation of expected performance since all applicable tolerances are simultaneously and exactly considered.

For each block, a Monte Carlo simulation of 100 realization was run and the criteria listed in Section 6.7 were used to investigate the system performance degradations or variations.

The pupil image after the MAORY exit port, the focal aperture and the exit pupil distance variations have also been calculated. Their changes, for each tolerance block, are always less than 1/1000.

6.7.1 Tolerance block 1 results

These tolerances are supposed to be compensated by design re-optimization once precise measures on the considered parameters has been delivered. The companies in charge of components manufacturing should deliver the final product within the limit imposed by these tolerances. Once the optics are ready, precise measures of their final parameters can be used as nominal values and the system can be re-optimized by means of free DOF used as variables during the instrument design phase.

Computed tolerances are summarized in Table 8 together with their effect on RMS WFE and optical distortions.

Table 8: Tolerance on curvature radii, conic constants and, if present, aspheric terms. For flat mirrors, the tolerance is expressed in terms of distance on the normal from the surface to the center of the curvature ("Sagitta"). The estimated changes of WFE and distortion should be combined by RSS to their nominal values.

	Curvature radius	**Conic Constant**	**Aspheric terms (if present)**
Conical mirrors	0.08%	± 0.05%	± 0.1%
Flat mirrors	± 633 nm (ΔSag)	-	-
RMS WFE - Estimated change			≈ 10 nm (Average)
Geometric distortion in MICADO FoV - Estimated change			≈ 0.15 μm (Median)
Max geometric distortion in the NGS FoV - Estimated change			≈ 12.7 mas (Median)

Astrometry performances: Since performance degradations are independent from design, we show Monte Carlo results of MAORY with even aspheric terms for mirror surface. Monte Carlo trials follow a normal distribution for considered tolerance values and results are shown in Figure 32 and Figure 33. They should be compared to nominal values shown in Figure 30 and Figure 29. Figure 32, box plots show minimum and maximum values and quartiles of Monte Carlo trials distribution for the astrometric residual error on a range of field rotation angle. In Figure 33 is shown the median 2D map of Monte Carlo trials and its distribution of star centroids movement after the maximum rotation for a single astrometric image in the circle containing the MICADO FoV. Median values are almost equal to those of nominal design, hence the effect of this tolerance block is negligible in terms of astrometric performances.

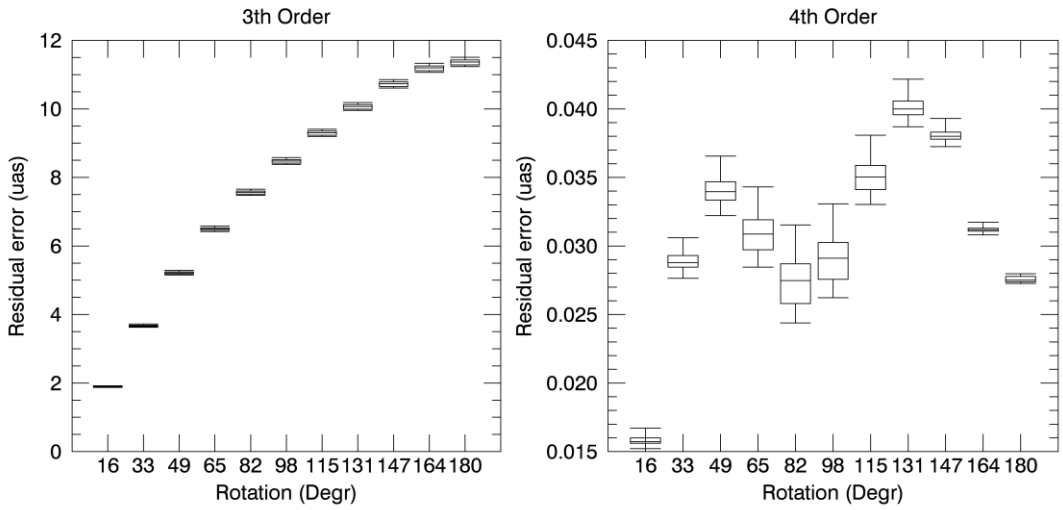

Figure 32: Astrometric residual errors for a range of field rotations in the circle containing the MICADO FoV. The error is the standard deviation computed as the quadratic sum of the X and Y error. Box plots show minimum and maximum values and quartiles of Monte Carlo trials distribution. Since the considered tolerances introduce low order distortions, the distributions width is very narrow.

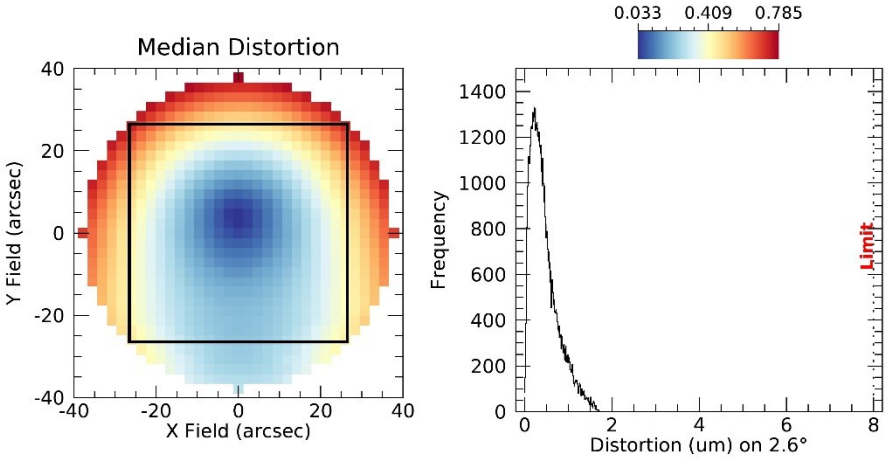

Figure 33: Star centroids movement for a single astrometric image in the circle containing the MICADO FoV (black square). Right: 2D distortion map of median values given by the Monte Carlo trials. Left: distribution of values given by the Monte Carlo trials.

6.7.2 Tolerance block 2 results

These tolerances are supposed to be compensated during the instrument alignment by means of the most sensitive DOF that have been chosen as the best set of compensators for required adjustments. Surface irregularities are modelled by means of standard Zernike coefficients whose max tolerance value is the exact RMS error of the surface. We verified that available DOF are able to compensate aberrations until Zernike coefficient 11 (the "spherical" term), hence the computed tolerances start from Zernike 4 (Z4 (the "defocus" term)) and end to

Zernike 11 (Z11). Tip and Tilt terms (Z2 - Z3) are not considered because they are part of tolerance Block 4. Z4, although is part of curvature radii tolerance (Block 1), has to be considered for off-axis mirror whose defocus term must be centered on FoV footprint instead of mirror vertex. On-axis surfaces tolerate Z4 as extra defocus (e.g. coating stress) in addition to that introduced by tolerance on curvature radii.

Computed tolerances are summarized in Table 9 together with their effect on RMS WFE and optical distortions.

Table 9: Low order RMS surface irregularities. The estimated changes of WFE and distortion should be combined by RSS to their nominal values.

	Z4 (nm)	**Z5 (nm)**	**Z6 (nm)**	**Z7 (nm)**	**Z8 (nm)**	**Z9 (nm)**	**Z10 (nm)**	**Z11 (nm)**
M6	15	7	9	9	7	6	9	5
M7	15	7	7	6	7	4	7	7
M8	25	6	6	6	7	4	7	7
M9	20	5	5	5	7	4	7	7
Dichroic	25	4	5	4	4	4	5	5
M10	15	6	6	6	7	8	9	5
M11	20	7	7	7	7	7	7	7
RMS WFE - Estimated change						≈ 20 nm (Average)		
Geometric distortion in MICADO FoV - Estimated change						≈ 0.08 µm (Median)		
Max geometric distortion in the NGS FoV - Estimated change						≈ 9 mas (Median)		

Results of the Monte Carlo trials in terms of astrometric performances are shown in Figure 34 and Figure 35. Refer to Section 6.7.1 for the meaning of the plots.

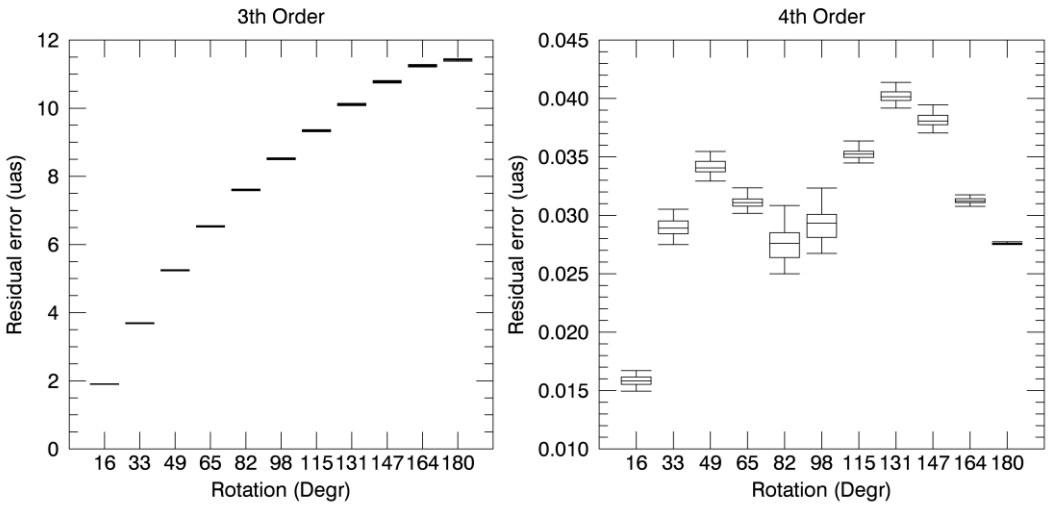

Figure 34: Astrometric residual errors for a range of field rotations in the circle containing the MICADO FoV. The error is the standard deviation computed as the quadratic sum of the X and Y error. Box plots show minimum and maximum values and quartiles of Monte Carlo trials distribution. Since the considered tolerances introduce low order distortions, the distributions width is very narrow.

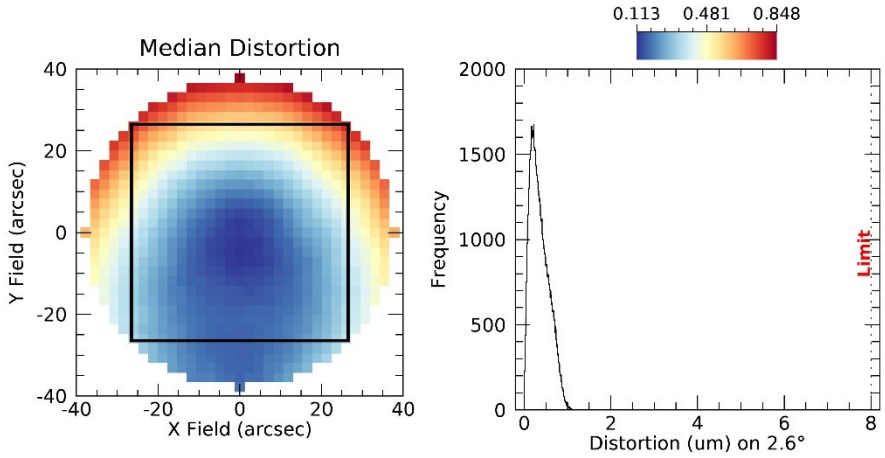

Figure 35: Star centroids movement for a single astrometric image in the circle containing the MICADO FoV (black square). Right: 2D distortion map of median values given by the Monte Carlo trials. Left: distribution of values given by the Monte Carlo trials.

6.7.3 Tolerance block 3 results

These tolerances cannot be compensated by means of components DOF. The high order surface irregularities, in addition to WFE, cause astrometric residual errors that are large compared to those introduced by other tolerances. Surface irregularities are modelled by means of standard Zernike coefficients whose max tolerance value is the exact RMS error of the surface. The Zernike terms greater than 11 (the "spherical" term) are set to a value so that the square root of the sum of the squares of the coefficients yields the specified RMS value.

Considering different field points, their beam footprints overlaps differently on each MAORY mirror surface. As the field rotates during the observations, the beam footprints cross the static errors on each mirrors surface. The lower is the overlap of different footprints, the bigger is the difference in terms of irregularities introduced in each optical trail relative to a given field point. As the optical footprint on a surface is the smaller the farther the surface is from the pupil plane, this error is largest for the surfaces with the largest conjugate ranges. For MAORY, this means that it is largest for the instrument selection mirror (M11) followed by the first mirror after the entrance focal plane (M6). Our results show that 12 μas residuals should be achievable with realistic requirements for the surface qualities and calibration time. This is not a hard limit as it can be reduced with on-sky observations of more objects and/or for longer times

Computed tolerances are summarized in Table 10 together with their effect on RMS WFE and optical distortions.

Table 10: High order RMS surface irregularities. The estimated changes of WFE and distortion should be combined by RSS to their nominal values.

	Square root of the sum from Z12 to Z120	
All surfaces	10 nm	
RMS WFE - Estimated change		≈ 12 nm (Average)
Geometric distortion in MICADO FoV - Estimated change		≈ 0.26 µm (Median)
Max geometric distortion in the NGS FoV - Estimated change		≈ 7 mas (Median)

Results of the Monte Carlo trials in terms of astrometric performances are shown in Figure 36 and Figure 37. Refer to Section 6.7.1 for the meaning of the plots. Because of high order effects previously described, in this case with need a 5th order polynomial fit to minimize the astrometric residual error. Figure 36 also reports the only contribution of M11 high order surface irregularities. M11, which is close to the MAORY focal plane, is the worst offender in terms of astrometric residuals and its contribution to the total error is about 75%.

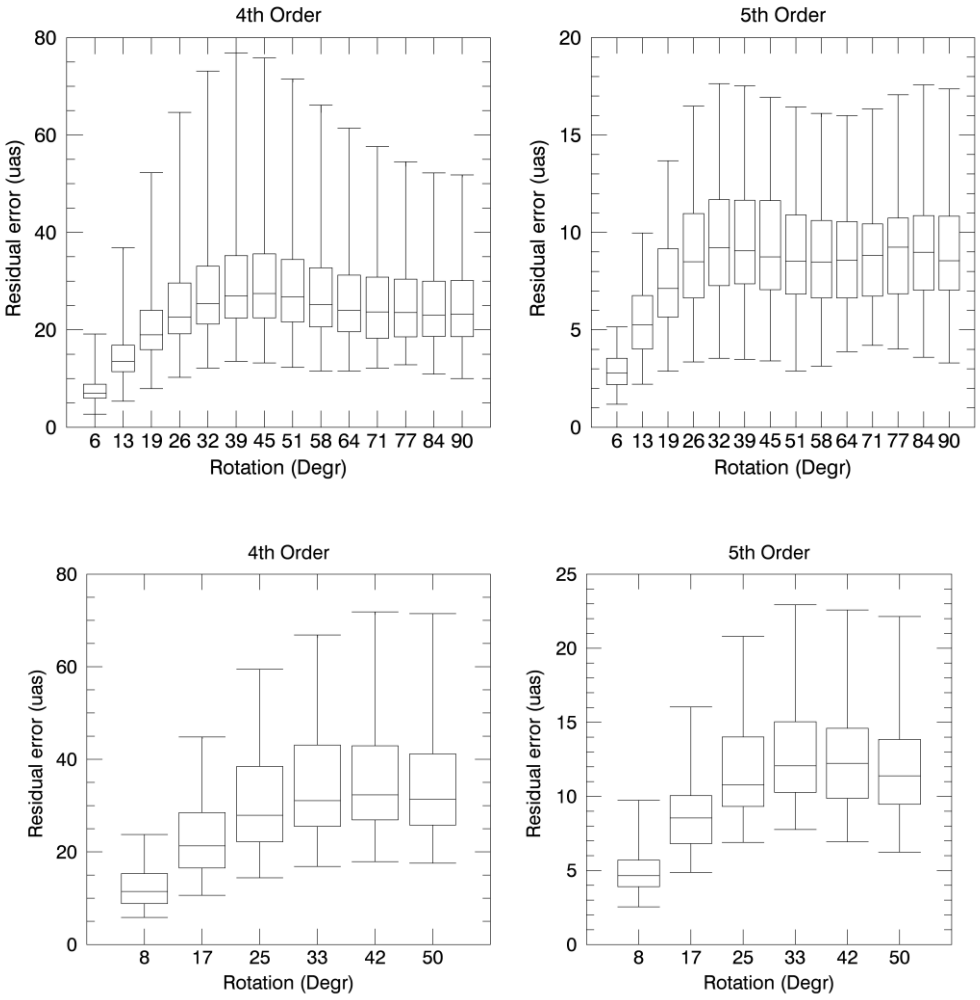

Figure 36: Astrometric residual errors for a range of field rotations in the circle containing the MICADO FoV. The error is the standard deviation computed as the quadratic sum of the X and Y error. Box plots show minimum and maximum values and quartiles of Monte Carlo trials distribution. Since the considered tolerances introduce high order distortions, the distributions width is larger than that seen in other tolerance block results. Upper plots refer to the only contribution of M11 high order surface irregularities. Lower plots refer to high order surface irregularities of all mirrors. In this case, we show values for a shorter range of field rotations since around 30 degree the residual error reach a plateau.

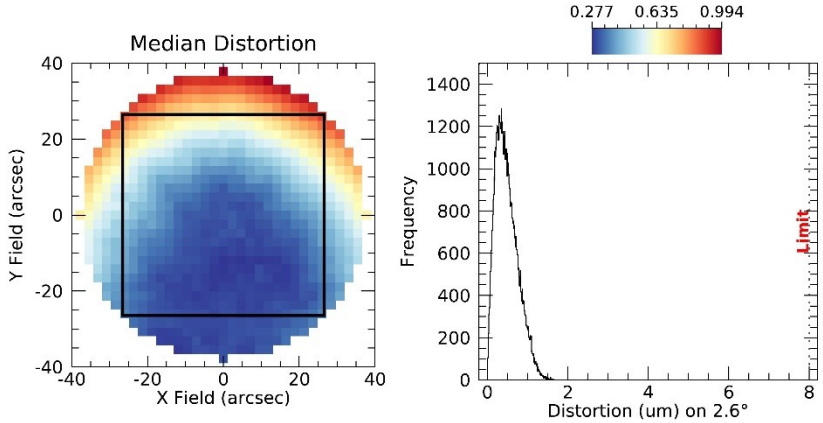

Figure 37: Star centroids movement for a single astrometric image in the circle containing the MICADO FoV (black square). Right: 2D distortion map of median values given by the Monte Carlo trials. Left: distribution of values given by the Monte Carlo trials.

6.7.4 Tolerance block 4 results

These tolerances refer to mechanical accuracy and precision of optical mounts. Sensitivity analysis on DOF tolerance of MAORY is a crucial step to understand the coupling between component misalignments and their effect on system performance. The DOF, used as compensators of misalignments, are rigid body motions of each optical surface that can be controlled by active components (i.e. hexapod or similar device) when needed. These are:

- TT about x and y axes
- Decentre in x and y axes
- Axial position,

where x and y are two axes orthogonal to the optical element axis.

The compensators shall work in combination with a metrology system or other measurement method which provides the necessary information to change the optical path according to estimated misalignments.

Computed tolerances are summarised in Table 11, together with their effect on RMS WFE and optical distortions. During the instrument alignment, available DOF have to move within these values in terms of repeatability. These tolerances also refer to the system stability during operation. Tolerances of DOF and compensation motions used during the alignment are shown in Table 12.

Table 11: Tolerance on surface DOF. The estimated changes of WFE and distortion should be combined by RSS to their nominal values.

	Tilts	**Decenters**	**Axial position**
All mirrors	± 17.5 µrad	± 50 µm	± 50 µm
RMS WFE - Estimated change			≈ 25 nm (Average)
Geometric distortion in MICADO FoV - Estimated change			≈ 1.2 µm (Median)
Max geometric distortion in the NGS FoV - Estimated change			≈ 11.7 mas (Median)

In this case, the Monte Carlo simulation considers a parabolic distribution since it yields selected values that are more likely to be at the extreme ends of the tolerance range. Results of the simulation in terms of astrometric performances are shown in Figure 38 and Figure 39. Refer to Section 6.7.1 for the meaning of the plots. We can say that, by using a polynomial

fit greater than 2nd order, the astrometric residual error is independent from misalignments since the distributions width of Monte Carlo trials is close to zero (see Figure 38).

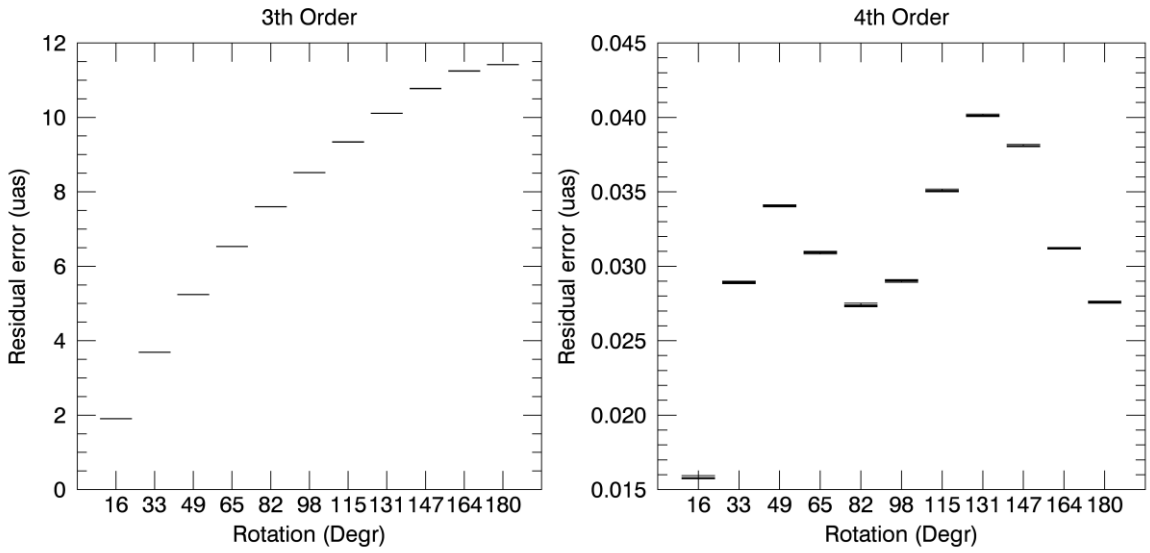

Figure 38: Astrometric residual errors for a range of field rotations in the circle containing the MICADO FoV. The error is the standard deviation computed as the quadratic sum of the X and Y error. Since the considered tolerances introduce very low order distortions, the distributions width of Monte Carlo trials is close to zero. This means the astrometric residual error is independent from misalignments.

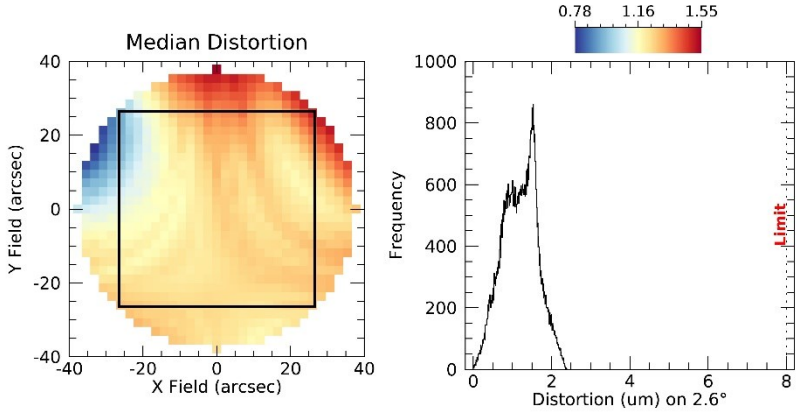

Figure 39: Star centroids movement for a single astrometric image in the circle containing the MICADO FoV (black square). Right: 2D distrortion map of median values given by the Monte Carlo trials. Left: distribution of values given by the Monte Carlo trials.

Through sensitivity analysis and SVD of the sensitivity matrix (a method described in Section 7), eighteen DOF are chosen as compensators to establish tolerances of the remaining DOF. Results are summarized in Table 12 together with the motion range of each compensator necessary to correct misalignments introduced by tolerance values. These numbers are results of Monte Carlo trials used to simulate the system alignment that is the subject of Section 7.

Table 12 : DOF used as compensators to system misalignments introduced by the remaining DOF tolerances

DOF to compensate misalignments	**Motion range**
X-Y Tilts (M6 - M7 – M8 – M9 – M10)*	± 5 mrad
Axial position (all Mirrors)	± 50 mm
Tolerances of remaining DOF	
X-Y Decenters	± 1 mm
X-Y Tilts (Dichroic)	± 0.5 mrad
Mirrors clock (off-axis rotation around optical axis)**	± 1 mrad
** M6 worst offender * M11 is free to move in TT to align MAORY and MICADO optical axes at telescope site	

6.8 MAORY LGS objective tolerance analysis: starting point

The performance of the LGS Objective is shown in the next figures.

Figure 40 shows the WFE map over the possible range of LGS constellation angular diameter, for three different cases of Zenith angle.

Figure 41 shows the WFE vs. Zenith angle (after removal of tip-tilt and focus). The variation of wavefront with Zenith angle is very slow. The calibration procedure to remove these quasi-static aberrations from the LGS measurements might be based on temporal filtering of the LGS WFS measurements. Figure 42 shows the variation of residual WFE vs. Zenith angle (after removal of tip-tilt and focus), assuming that the average wavefront computed over the last 4 minutes in time is subtracted from the wavefront at a given Zenith angle. The residual WFE is indeed very small, 10 nm for all possible Zenith angles.

Figure 42 shows the differential focus shift among the 6 LGS vs. Zenith angle, giving an indication of the required amount of differential re-focussing among different LGS probes.

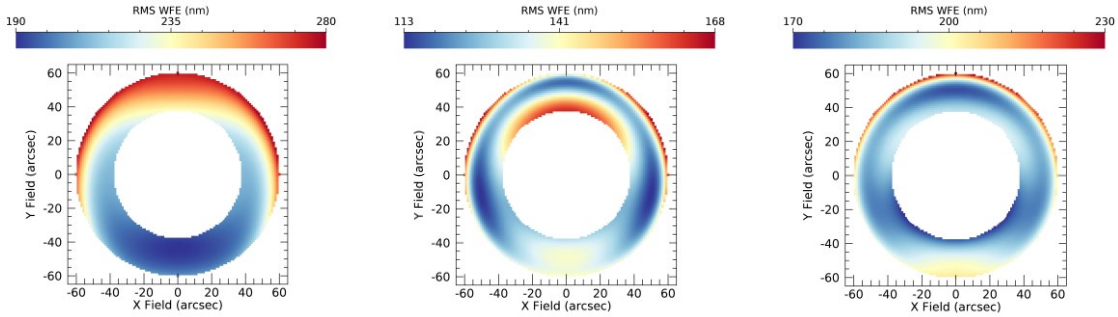

Figure 40. WFE maps at three different ranges of the LGS from the telescope. From left to right: 80km – 160km – 240Km. The WFE map is enclosed in a ring of inner diameter 45 arcsec and outer diameter of 60 arcsec: these are the two possible cases of LGS asterism.

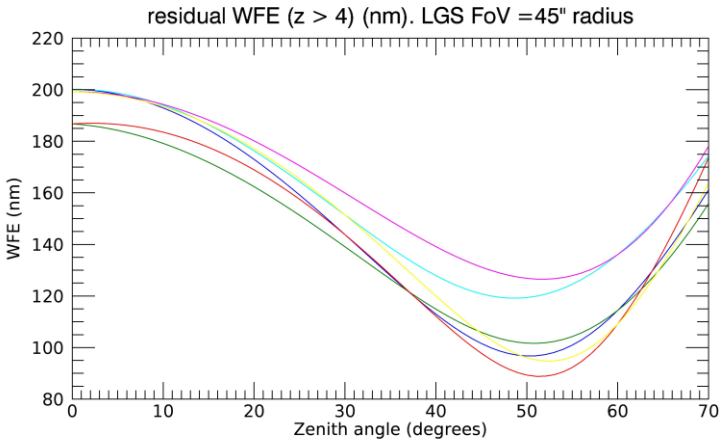

Figure 41. Residual WFE at the LGS Objective image plane (after removal of tip-tilt and focus) as a function of Zenith angle. The 6 curves correspond to an equal number of LGS, symmetrically arranged over a 45 arcsec radius FoV.

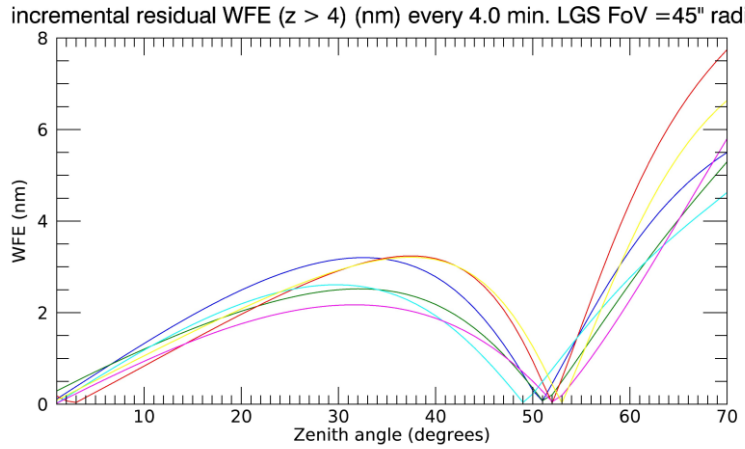

Figure 42. Variation of the residual WFE at the LGS Objective image plane (after removal of tip-tilt and focus) as a function of Zenith angle. The temporal average of the last 4 minutes is removed from the wavefront at each Zenith angle. The telescope tracks one degree every 4 minutes. The 6 curves correspond to an equal number of LGS, symmetrically arranged over a 45 arcsec radius FoV.

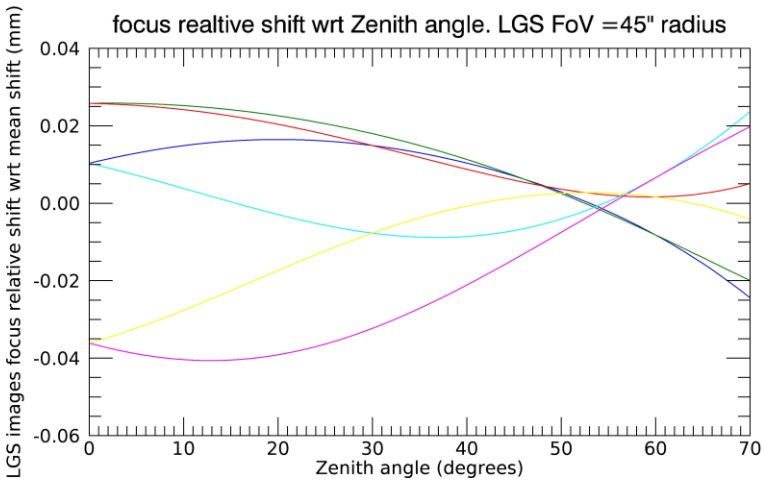

Figure 43. Differential focus position. LGS relative focus shift at the LGS Objective image plane as a function of Zenith angle. The 6 curves correspond to an equal number of LGS, symmetrically arranged over a 45 arcsec radius FoV.

6.9 LGS Objective tolerance analysis

The same approach which has been applied to the Main Path Optics has also been used to tolerance the LGS Objective. The tolerance analysis has been performed with a limit of WFE degradation of about 30% and a pupil blur degradation of 1/10 of sub-aperture (considering 80 sub-apertures along the diameter). The analysis has been split into three blocks:

- Block 1: Manufacturing errors;
- Block 2: Surface irregularities;
- Block 3: Alignment repeatability.

In the tolerance analysis, the main differences between the LGS Objective and the Main Path Optics are:

- The LGS Objective contains lenses in the optical path;
- The RMS WFE of the LGS Objective shall exclude the TT and defocus terms;
- Geometric distortion is not an issue for the LGS Objective;
- LGSs are not focused at infinity but in a range of finite altitudes.

The next tables show the optical tolerances of the refractive elements in the LGS Objective.

Table 13. LGS Objective refractive elements general tolerances.

Parameter	**Tolerance**
Curvature radius	± 0.1 %
Conic constant	± 0.05 %
Sag of flat surfaces (residual curvature)	± 316 nm
Wedge	± 50 micro-rad
Centring	± 0.05 mm
Surface irregularity RMS	30 nm

Table 14. LGS Objective refractive elements material tolerances.

Parameter	**Tolerance**
Glass refractive index	± 5e-4
Glass Abbe number	± 1%

Mirror tolerances inside the LGS Objective are the same as for the mirrors in the Main Path Optics: the only exception is surface irregularity, which, in the case of the mirrors in the LGS Objective, is 30 nm RMS for all orders.

The sensitivities related to available DOF can be used during the alignment phase of the instrument since the worst offenders to system performance are also the best set of compensators for required adjustments. Motion ranges to compensate the tolerances of DOF and repeatability of chosen compensators are shown in Table 15.

Tolerance analysis results are shown through Monte Carlo simulations, where the figure of merit is the RMS WFE (without tip-tilt and defocus). 100 Monte Carlo trials were generated assuming Normal statistical distribution. The displayed values are for 6 LGSs at a radius of 45 arcsec, for 15 sampled Zenith angles.

Figure 44, Figure 45 and Figure 46 show the increment in WFE due to the computed tolerances for Block 1, Block 2 and Block 3 respectively. The results regarding the pupil blur degradation are compliant with the requirement, as showed in Figure 47.

Table 15. LGS Objective refractive elements DOF tolerances. Some DOF (first 2 rows) are used as compensators to system misalignments. The tolerated misalignments are reported in the last 3 rows. The compensators must satisfy the repeatability requirements reported in the table.

DOF used as compensators	**Motion range to compensate tolerances of remaining DOF**
Axial position (Lenses 3 - 4 - 5 - 6)	± 30 mm
X-Y Decentres (Lenses 2 - 3 - 5 - 6)	± 2 mm
Tolerances of compensators (repeatability)	
Axial position	± 50 µm
X-Y Decentres	± 30 µm
Tolerances of DOF	
X-Y Decentres	± 0.5 mm
X-Y Tilts	± 0.5 mrad
Axial Position	± 0.5 mm

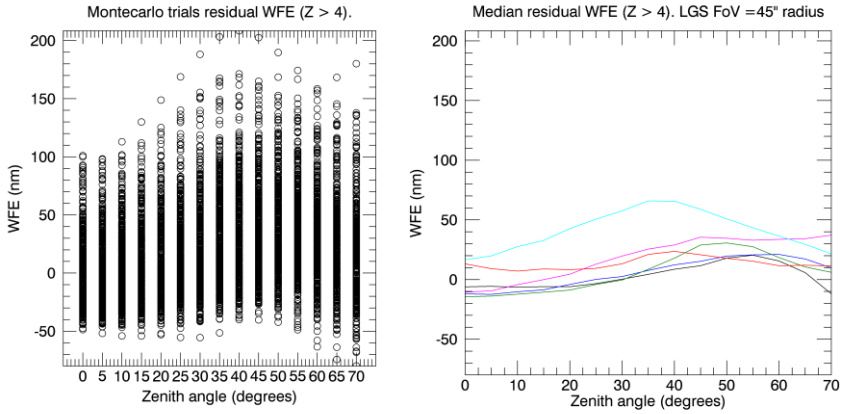

Figure 44. Monte Carlo trials for manufacturing errors of the LGS Objective optics. Left: variation of WFE at the LGS Objective image plane with respect to the nominal value as a function of Zenith angle. Right: median values of the left plot, different colours correspond to different positions around the 45 arcsec circle FoV of the LGSs.

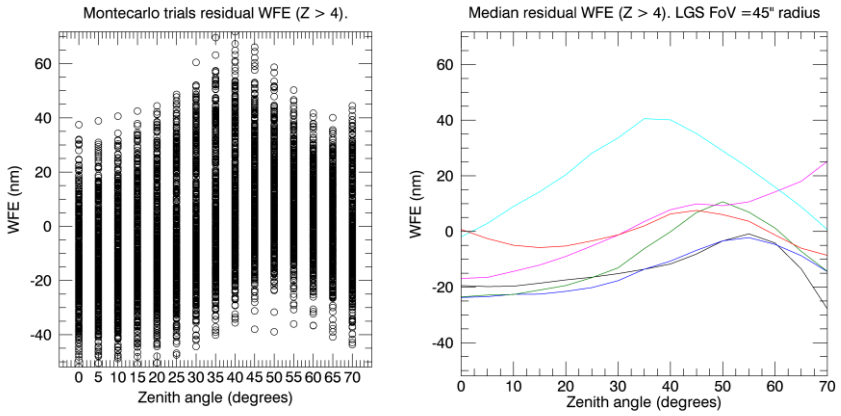

Figure 45. Monte Carlo trials surface irregularities of the LGS Objective optics. Left: variation of WFE at the LGS Objective image plane with respect to the nominal value as a function of Zenith angle. Right: Median values of the left plot, different colours correspond to different positions around the 45 arcsec circle FoV of the LGSs.

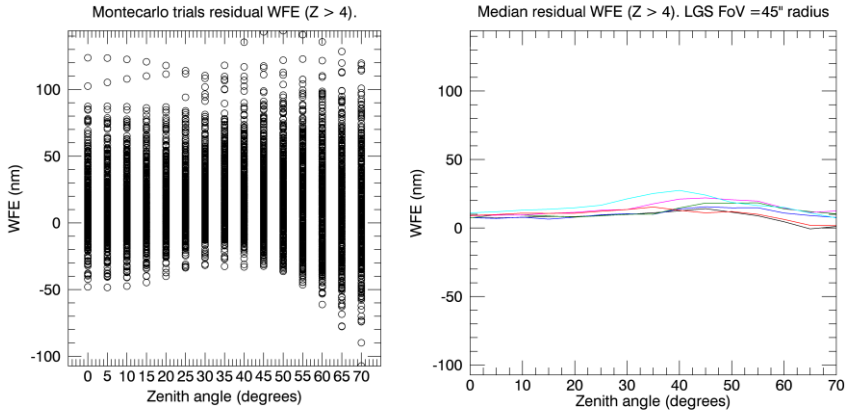

Figure 46. Monte Carlo trials for DOF tolerances. Left: variation of WFE at the LGS Objective image plane with respect to the nominal value as a function of Zenith angle. Right: Median values of the left plot, different colors correspond to different positions around the 45 arcsec circle FoV of the LGSs.

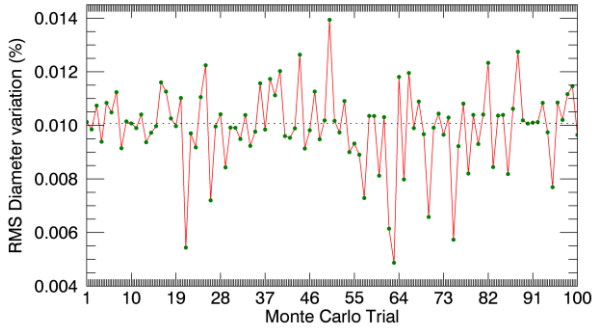

Figure 47. RMS of pupil image diameter variation (%) inside the LGS Objective FoV due to the optical tolerances.

7. MAORY optical alignment concept

The sensitivity analysis on opto-mechanical tolerance of MAORY is a crucial step to plan the alignment concept that would be required in the AIV phase of the instrument. In this Section, the logic behind the science path alignment as well as the criteria in choosing compensators are described.

The science path optical alignment plan is based on roughly positioning the optics within the precision of a laser tracker, then using TT and axial adjustments to refine the alignment. It is important, as first step, to define a local and global coordinate system origin. Then, coordinate metrology can be used to align each optic (or subsystem) in XYZ with respect to the MAORY global coordinate system origin. Each optical element is installed on the main structure by means of the optical mount and an interface plate. A kinematic interface between the interface plate and the optical mount is foreseen with a repeatability of tens of microns.

The main steps for the PFR alignment are the following:

1. The optics are pre-aligned in their mounts prior to installation on the optical bench structure.
2. Retro-spheres are installed on the optic and their coordinates are known with respect to the optic local coordinate system. These local coordinates will then be transferred into the MAORY global coordinate system.
3. The laser tracker system reads the retro-sphere locations once the interface plate is installed on the optical bench. Then it is shimmed and settled into position according to the laser tracker measure.
4. Once the optics are properly located on the bench, they have to be aligned with the optical axis. A laser beam defines the incoming optical axis and a sources simulator is used to align the rest of the system.

The DOF, used as compensators of misalignments, are rigid body motions of each optical surface that can be controlled by active components (e.g. a hexapod structure or other automatic adjustment) during operations. These are:

- Tilt in x and y axes
- Decentre in x and y axes
- Axial position

The active compensators should work in combination with the metrology system that provides the necessary information to change the optical path according to estimate misalignments. The idea is to analyse all the available DOF and select the best set of compensators that can control the system performances to required accuracy. This method is based on SVD and regularization of the sensitivity matrix.

The DOF sensitivities are measured in terms of Zernike coefficients across the field. By perturbing each of the individual DOF for each optical surface, the change of each Zernike coefficient is recorded in a matrix whose rows and columns are respectively the total number of Zernike values per field point and the total number of DOF. This sensitivity matrix includes all the necessary information to simulate alignment using the best set of compensators. It is defined as:

$$S_{ij} = \partial Z_i / \partial x_j$$

Where the WFE is decomposed into n Zernike polynomials (z_i ; i=0, n) and the RSS of z_i is the total WFE. $\partial Z_i / \partial x_j$ is measured from the nominal configuration as:

$$(Z_{perturbed,i} - Z_{nominal,i}) \,/\, (\, j^{th} \text{ DOF perturbation})$$

During the alignment phase, the Zernike coefficients are measured for different field points by means of a SH-WFS and once the coupling between DOF and their effect on Zernike coefficients is understood, a solution on misalignments could be found.

Let's consider the Zernike coefficients as a metric to evaluate the system performances (MF) and all the available DOF listed in a vector (x_{dof}). The relation between the two can be written:

$$MF = f(x_{dof})$$

The goal is to find the best x_{dof} that minimize MF. This relation could be non-linear and interdependences between DOF could occur. The method followed to solve the problem is based on the one described by Chapman et al. [42] where, through the SVD of sensitivity matrix, the Eigen vector define the best set of DOF used to compensate for misalignments.

The sensitivity matrix is decomposed as follow:

$$S=UMV^T$$

Where U and V are column orthogonal matrices and M is a diagonal matrix containing the singular values listed in decreasing order along the diagonal. They are always positive numbers and define the strength of the type of aberration that result from changes in the DOF. The most sensitive aberration due to a set of DOF misalignment has the largest singular value. Columns of U are Zernike coefficients introduced by changes in DOF listed in columns of V and whose strength is given by the M singular values. The goal is to find the most linearly independent set of compensators within the sensitive subspace of aberrations. This is done by truncating the sensitivity matrix until the sum of residuals of the new singular values are below a given threshold.

The truncated sensitivity matrix S' contains less singular values close to zero and it is well conditioned. The converging solutions in terms of changes in DOF that minimize the WFE is the following:

$$\partial X = -V' \cdot W'^{-1} \cdot U'^T \cdot Z$$

Where $(V' \cdot W'^{-1} \cdot U'^T)$ is the pseudo-inverse SVD of S' and Z is the matrix of Zernike aberrations.

This method gives accurate solutions only when the misalignments of optical components are located within the linear regime of sensitivities (i.e. perturbations around the nominal positions). In cases of large misalignments, a new algorithm for minimization process must be used.

The method implemented for MAORY is based on damped least squares algorithm of Zemax® ray-tracing software. Once a merit function for system performances is defined, the goal is to minimize the function:

$$MF^2 = \frac{\sum W_i (V_i - T_i)^2}{\sum W_i}$$

Where V_i is the current values of each Zernike coefficients, T_i the target values, and W_i the weight. The best set of compensators is defined by the method previously described and their perturbations, that should be corrected to align the system, are found by minimizing MF.

The developed algorithm is based on ZPL macros and operates as follow:

- Read the Zernike values from the SH-WFS located at different field points.
- Allocate the Zernike values to target column in merit function editor.
- Optimize the system using the Zemax damped least squared algorithm.
- Read the perturbed compensator DOF. These are the misalignments that generated the measured Zernike values and that should be compensated.

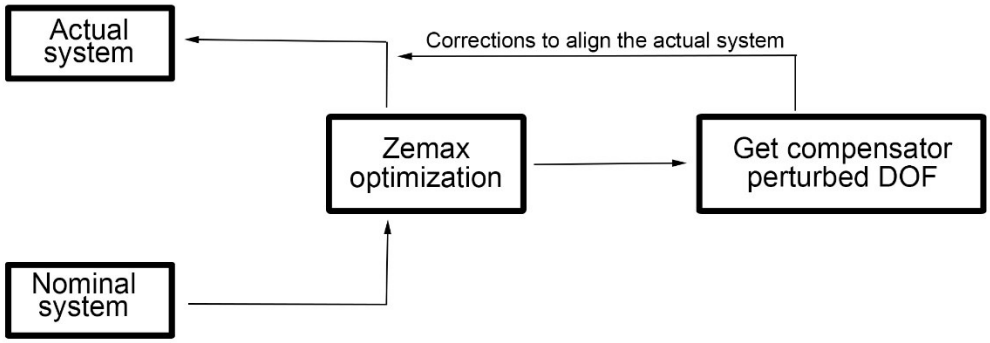

Figure 48 : Flow diagram to give a syntetich view of the alignment process

7.1 Ray-Tracing simulations of MAORY main path alignment

The MAORY FoV has to re-image the ELT focal plane with diffraction limited optical quality and low geometric distortion. To keep track of optical distortion during the alignment, a set of artificial sources are placed at the entrance focal plane to simulate a re-imaged star field by ELT. To exactly reproduce the ELT focal plane, the sources must be fixed with a proper chief ray angle in order to reproduce the ELT exit pupil position and should deliver 'diffraction limited' images. It is possible to test the amount of optical distortion by measuring PSF centroids of two sources that are at the same distance from the FoV centre. In the real case, the FoV rotates at different speeds as the telescope tracks and a de-rotator is used to counter-rotate the field. During rotation, imaged sources don't follow a circle arc due to optical distortions. This introduces an error that propagates in the counter-rotation and translates in PSF elongation.

Analytical description of how we test distortion is shown in Figure 49. A source of coordinates h_x , h_y , keeps the same radial distance R_1 from the FoV center when the optics are distortion free. If we measure the coordinates h_{xM}^r , h_{yM}^r that are different from analytical expectation of rigid body rotation (h_x^r , h_y^r), these deviations are values used to quantify optical distortions. For a given rotational angle ϑ, the differences $(R_2 - R_1)$ are additional target values of the merit function.

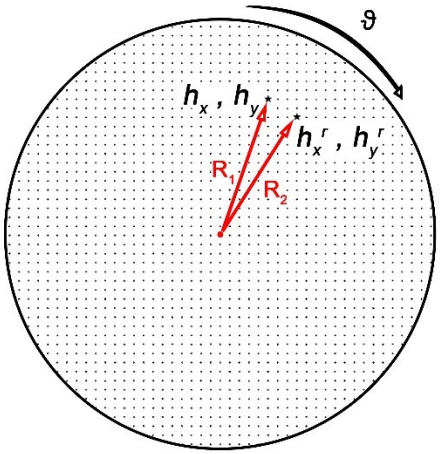

$$R_1 = \sqrt{(h_x\ )^2 + (h_y\ )^2}$$

$$h_x^r = h_x \cos\vartheta + h_y \sin\vartheta$$

$$h_y^r = h_y \cos\vartheta - h_x \sin\vartheta$$

$$R_2 = \sqrt{(h_x^r\ )^2 + (h_y^r\ )^2}$$

$$Distortion = R_2 - R_1$$

Figure 49 : Pinhole mask concept and analytical evaluation of field distortions

In addition to intrinsic optical distortion, mirrors misalignments related to environment effects, shift the optical axis in a way that it is no more aligned with the field de-rotator mechanical axis. The mismatch generates star trails as shown in Figure 50 and can be compensated by tilting M11. That's the reason to add M11-tilts as additional compensators for geometric distortion.

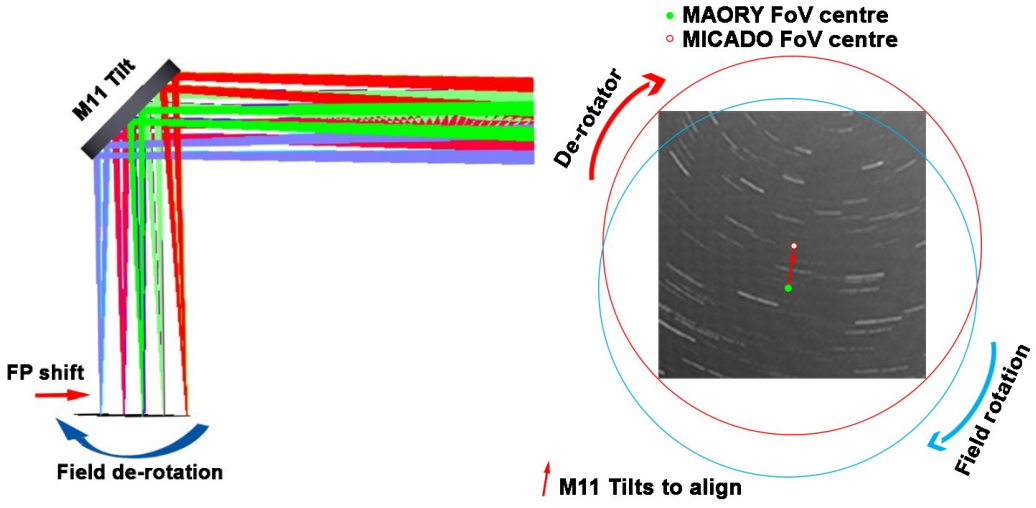

Figure 50: Geometric distortion due to rotator errors. Focal plane shift w.r.t. rotational axis.

Considering distortion, the developed algorithm operates as follow:

- Measure the Zernike coefficients from the SHWFSs located at different field points.
- Measure the distortions as defined in Figure 49.
- Allocate the Zernike coefficients to target column of the merit function.
- Optimize the system using the damped least squared algorithm and the compensators as variables.
- Allocate the distortion values to target column of the merit function.
- Optimize the system using the damped least squared algorithm and add M11-tilts as variables if necessary.
- Read the perturbed degree of freedom of compensators. These are the misalignments that generated the measured Zernike coefficients and distortion values and that should be compensated.

To test the accuracy of the Zemax-based algorithm, 500 Monte Carlo trials were run simulating random misalignments of different magnitudes. Monte Carlo trials follow a normal distribution for considered DOF misalignments. The maximum amount of misalignments assigned to DOF are as follow:

- Decentres = ± 1.1 mm
- Tilts = ± 4.5 mrad
- Axial position = ± 1.1 mm

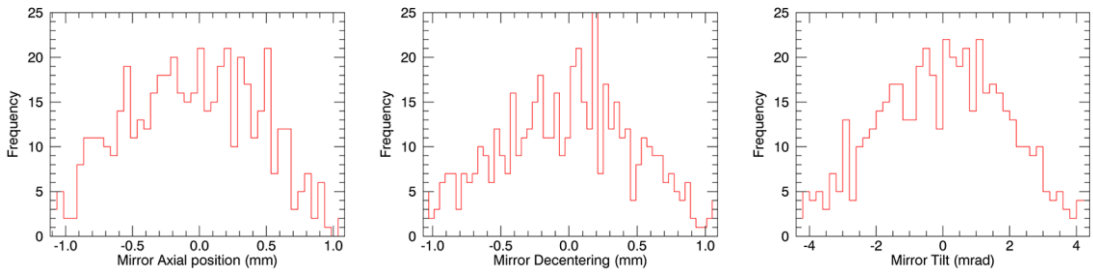

Figure 51 : From left to right : distribution of DOF perturbations given by Montecarlo Trials for mirrors axial positions, decenters and Tilts

The sensitivity analysis identified eleven DOF as best set of compensators for WFE. A schematic view of necessary compensators is shown in Figure 52. X-Y Tilts of five mirrors plus one mirror axial distance are enough to compensate WFEs but, in addition to that, M11 tilts must be controlled to avoid misalignments between the optical axis and the rotational axis of field de-rotator.

Given the same set of 500 Monte Carlo trials, the alignment simulation was run several time varying different parameters. This approach was adopted to analyse all possible error sources that could affect the measurements and the accuracy of the algorithm. The variable parameters among different alignment simulations are the following:

- Field sampling: related to the number and geometry of the sources.
- Errors on artificial sources position w.r.t. the nominal stars positions on sky.
- Mirror surfaces irregularities: related to uncertainties in the measured WFE data of mirror surface.

To give an idea of the effectiveness in correction of misalignments, Figure 54 and Figure 55 show the starting point in terms of WFE and geometric distortion of the system through the Monte Carlo trials. Considering 9 Field sources on a regular grid, sampling the entire FoV, the median results of the alignment procedure are very close to the nominal system performances showed in Figure 28 and Figure 29 (left).

Figure 53 shows the distributions of movements, as result of the algorithm output, that DOF compensators had to apply through the Monte Carlo trials. The extremes of each distributions are almost the same even in presence of different sources of error which are described in the following Sections.

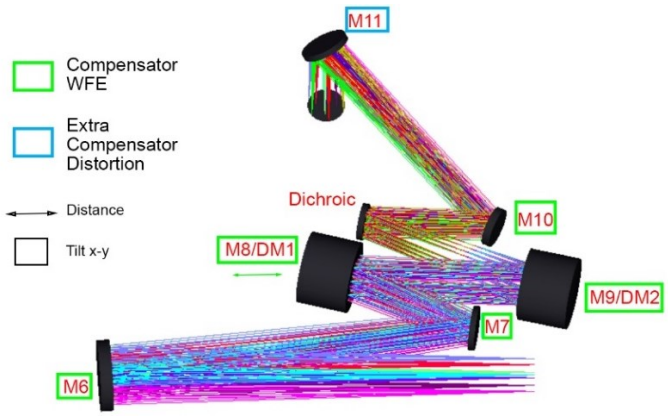

WFE	Distortion
X-Y Tilts compensators	
M6 - M7 - M8 - M9 - M10	M6 - M7 - M8 - M9 - M10 - M11
Axial position compensators	
M7 – M8	M7 – M8

Figure 52 : MAORY science path optics and their DOF compensators. Boxes and green color indicates compensators necessary to achieve diffraction limited optical quality during the alignment. Cyan color indicates additional compensator motions to achieve the requested optical distortion.

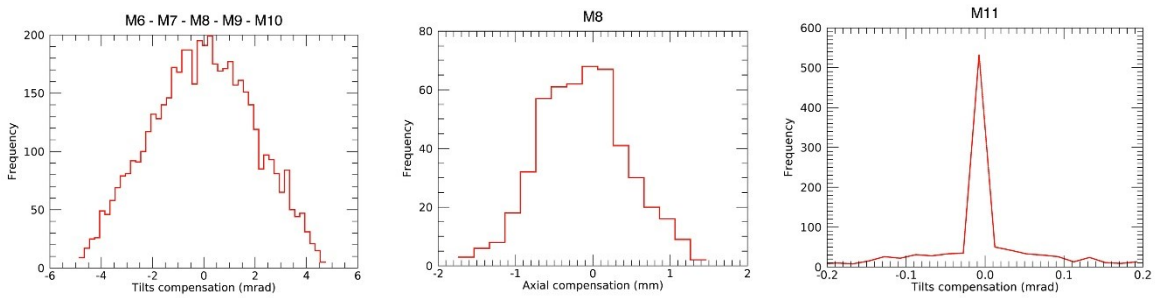

Figure 53 : From left to right : distribution of DOF motions to compensate misalignments given by Montecarlo Trials for mirrors tilts, axial positions and M11 Tilts

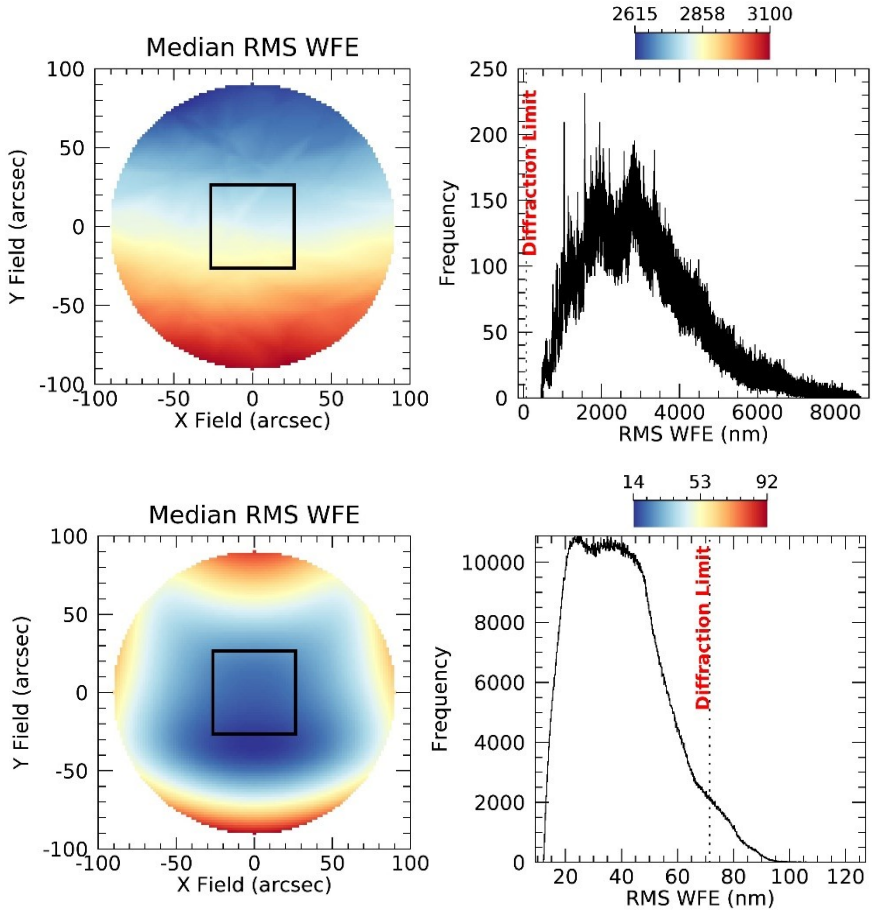

Figure 54: Black square is the MICADO 53"x53" FoV. (Top row) Right: 2D RMS WFE map of median values given by the Monte Carlo trials that simulate system misalignments. Left: distribution of values given by the Monte Carlo trials. Every field point is above the diffraction limit due to misalignments. (Bottom row) Right: 2D RMS WFE map of median values given by the Monte Carlo trials after the alignment procedure. Left: distribution of values given by the Monte Carlo trials. Values are very close to nominal design.

By using the reverse optimization on compensators and applying the computed DOF movements, the system performances reach values that are very close to nominal. Results from Monte Carlo trials reveal that 90% of aligned systems, following the algorithm

previously described, are within 4 nm of residual WFE and within the limits for optical distortions (see Section 5.1.1).

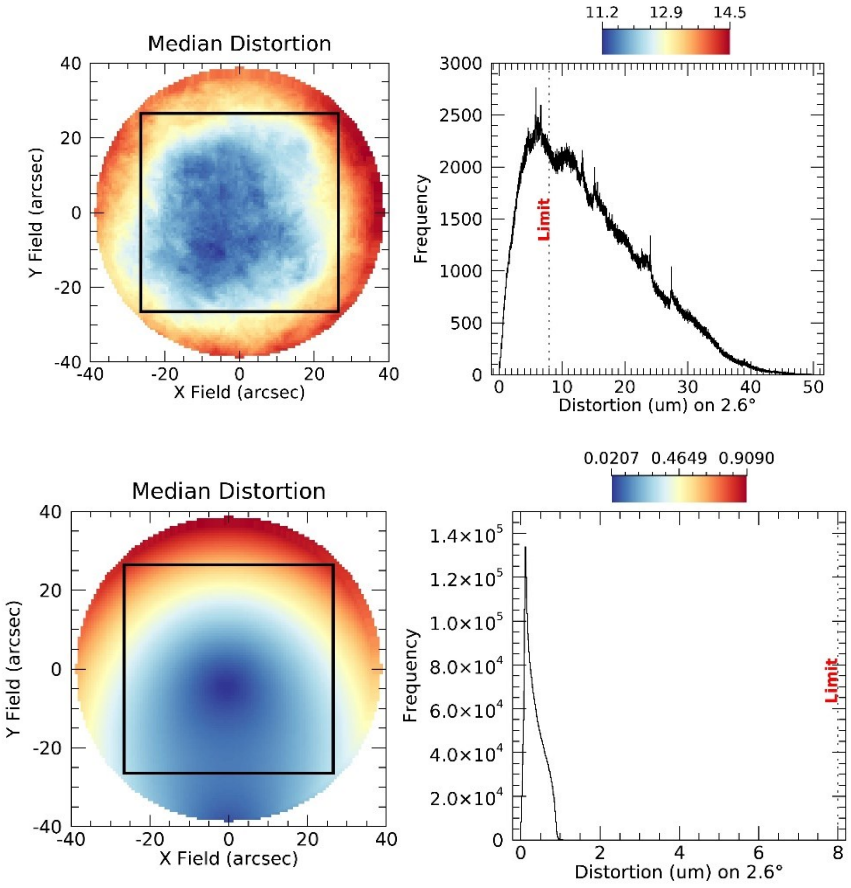

Figure 55: Black square is the MICADO 53"x53" FoV. (Top row) Right: 2D distortion map of median values given by the Monte Carlo trials that simulate system misalignments. Left: distribution of values given by the Monte Carlo trials. Median values are above the performance limit due to misalignments. (Bottom row) Right: 2D distortion map of median values given by the Monte Carlo trials after the alignment procedure. Left: distribution of values given by the Monte Carlo trials. Values are very close to nominal design.

7.1.1 Field sampling

Field sampling should be considered to address the best ratio of alignment performance and number of sources. Since the artificial source, as further discussed in Section 7.4, must reproduce the ELT focal plane with the right exit pupil position, different geometries of sources were investigated to find the most reliable in terms of mechanical manufacturing. ELT is not telecentric and the chief ray angle of a star changes along the pupil radius (see Figure 66). Thus, at the focal plane, if the sources will be fixed on a circumference, they would have the same chief ray angle reducing the complexity in terms of mechanical manufacturing. The considered sources number and geometry are shown in Figure 56.

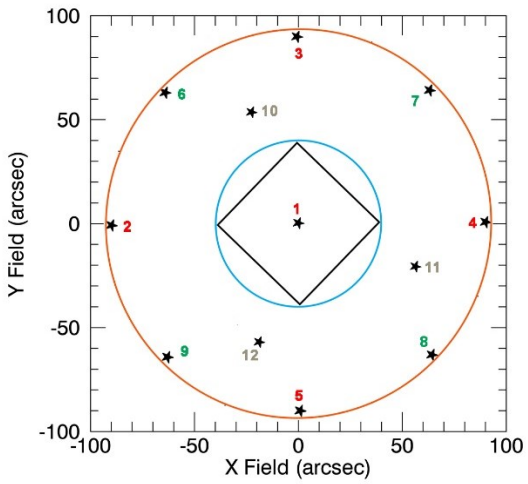

Figure 56: Artificial sources numbers and geometry. The black square is the MICADO detector FoV.

The simulation was run considering three different set of 5, 9 and 12 sources. The results are summarized in Figure 57 in terms of mean residual WFE. It is the difference between the mean RMS WFE, across the entire FoV, between the nominal value and the measured value after the alignment procedure. Boxplots are the distributions of values across the 500 Monte Carlo trials. To highlight the stability of the algorithm, Figure 57 also shows the outlier values of the simulation. Except for the 5 sources case, the maximum geometric distortion of each realization is lower than 1.5 µm (within the MICADO FoV).

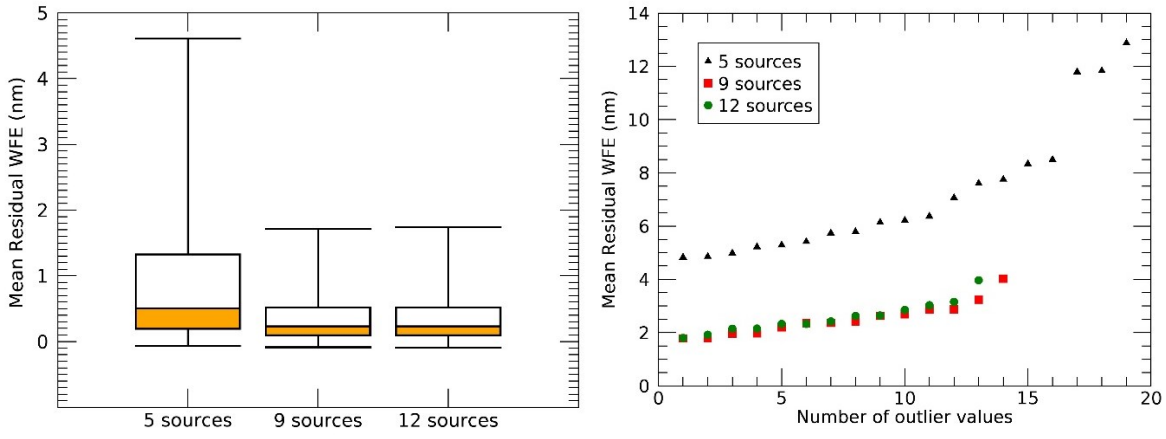

*Figure 57: Residual RMS WFE. It is the difference between the nominal WFE and the measured WFE (mean across the entire FoV) after the alignment procedure. Box plots show minimum and maximum values and quartiles of Monte Carlo trials distribution. On the right, the values of outliers are shown: outliers are those values that are either less than Q1 - 3 * IQR or greater than Q3 + 3 * IQR where Q1 is the lower quartile, Q3 is the upper quartile and IQR is the inner quartile range (Q3 - Q1).*

The case of 5 sources, placed on a cross geometry, is more critical for the algorithm accuracy especially in terms of geometric distortion. Results are shown in Figure 58 and they are anyway below the requested limit.

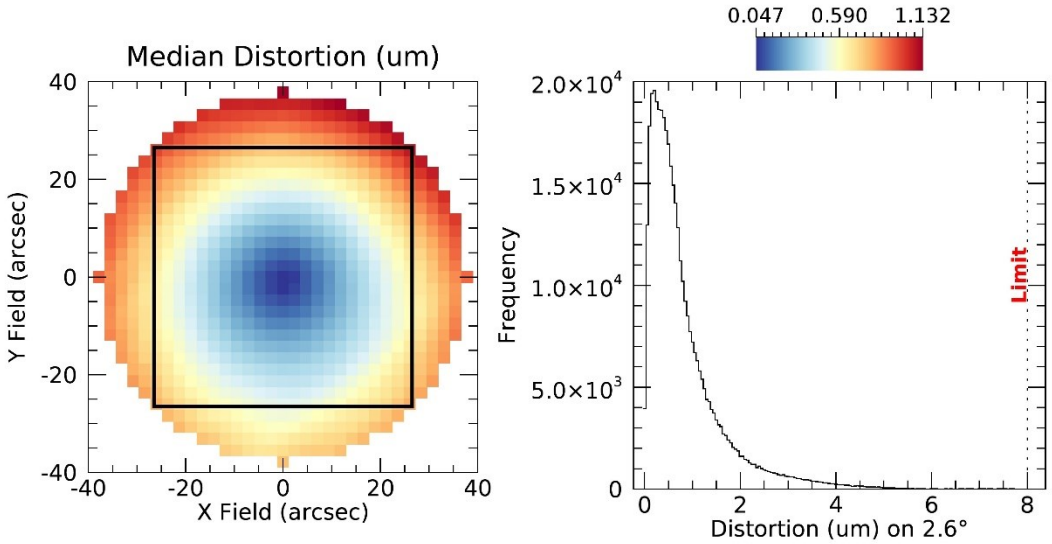

Figure 58: Black square is the MICADO 53"x53" FoV. Right: 2D distortion map of median values given by the Monte Carlo trials after the alignment procedure. Left: distribution of all values given by the Monte Carlo trials.

Going from 9 to 12 sources there are no significant improvements in the algorithm accuracy and stability, thus 9 sources are the best compromise unless there are no errors in positioning the sources. This is the topic of the next Section.

7.1.2 Source positions errors

Field errors should be considered as part of tolerance in mechanical manufacturing of the mask that simulates the ELT focal plane. They also can be related to alignment errors during the assembly and integration phase.

The source position errors are simulated considering random values with a Gaussian distribution, zero mean, and the standard deviation of 3% of the nominal value. This means that the maximum value of the error for a source at the edge of the FoV is about 9mm.

To take care of these errors, during the reverse optimization, the nominal sources positions are considered as variables in addition to the DOF compensators.

The simulation has been run considering 9 and 12 sources following the geometry of Figure 56 and results are shown in Figure 59.

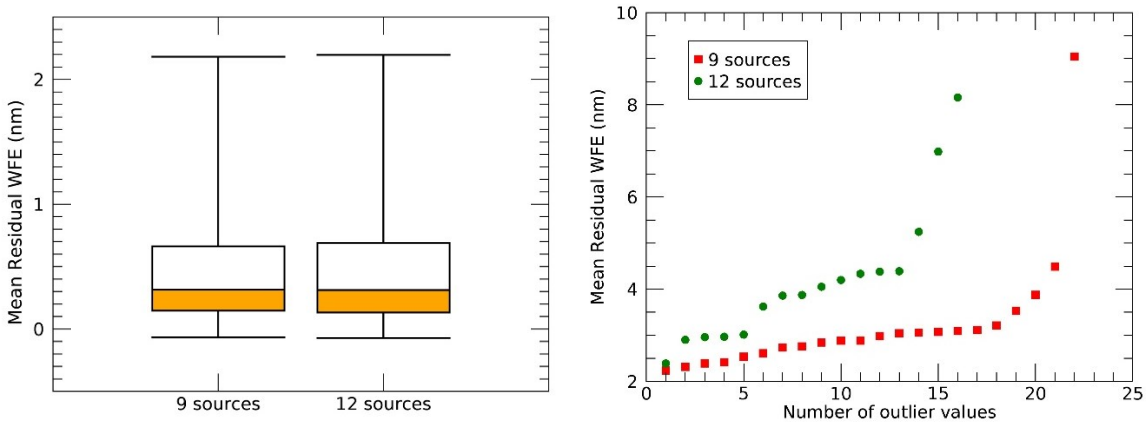

*Figure 59: Residual RMS WFE. It is the difference between the nominal WFE and the measured WFE (mean across the entire FoV) after the alignment procedure. Box plots show minimum and maximum values and quartiles of Monte Carlo trials distribution. On the right, the values of outliers are shown: outliers are those values that are either less than Q1 - 3 * IQR or greater than Q3 + 3 * IQR where Q1 is the lower quartile, Q3 is the upper quartile and IQR is the inner quartile range (Q3 - Q1).*

There is no significant difference between the two cases except for the outlier values that are greater considering 12 sources. The small loss of stability is probably related to a greater number of variables in the computation.

Even in presence of source position errors, the maximum geometric distortion is lower than 1.5 µm (within the MICADO FoV).

7.1.3 Mirror surfaces irregularities

MAORY mirrors are planned to be delivered by the companies with a full characterization of mirror surfaces. In principle, we can use the measured values of surface irregularities and add these information to the nominal design. In case we miss these information, or they are not accurate, the impact of surface irregularities on the effectiveness of the algorithm is shown in Figure 60.

The irregularities are divided into LO and HO following the logic behind the tolerance analysis of Section 6.7. The RMS values of surface irregularities used in the simulation, are the same defined by the tolerances.

LO irregularities are partially absorbed during the alignment, while HO irregularities are very critical for the algorithm accuracy. In both cases the mean residual WFE is greater than what is accepted by the tolerance analysis meaning that a good characterization of mirror surfaces is required for a successful MAORY alignment.

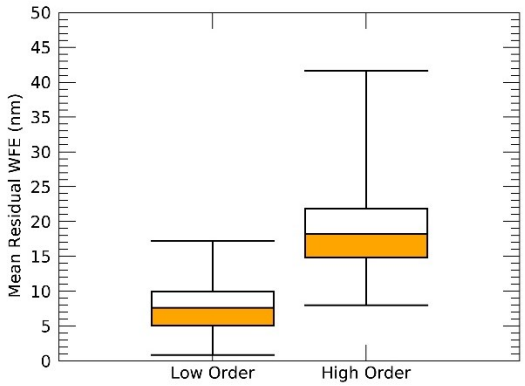

Figure 60: Residual RMS WFE. It is the difference between the nominal WFE and the measured WFE (mean across the entire FoV) after the alignment procedure. Box plots show minimum and maximum values and quartiles of Monte Carlo trials distribution. In this case there are no outlier values.

Even in presence of mirror surface irregularities, the maximum geometric distortion is lower than 1.5 µm (within the MICADO FoV).

7.2 DMs stroke analysis to correct optical misalignments

This analysis is focused only on the impact of alignment errors to the RMS WFE. The allowed change has to keep the RMS WFE below the diffraction limited optical quality within the MICADO FoV. Table 16 summarizes the alignment errors that, combined with other tolerances (Section 6.7), push the system to the limit of allowed RMS WFE change. They are a factor 2 greater than DOF tolerances reported in Section 6.7.4.

Table 16: Tolerance on surface DOF. The estimated changes of WFE and distortion should be combined by RSS to their nominal values

	Tilts	**Decenters**	**Axial position**
Worst case mirror misalignments	± 35 µrad	± 0.1 mm	± 0.1 mm

The analysis on the DMs actuators stroke, necessary to correct the specified alignment errors, is based on Monte Carlo simulation. One hundred system realizations are generated which meets the specified tolerances following a parabolic distribution. The considered statistic yields selected values that are more likely to be at the extreme ends of the tolerance range.

For each realization, the DMs are modelled by means of standard Zernike coefficients and the system is optimized to minimize the RMS WFE. The considered range of Zernike coefficients goes from Z4 (the "defocus" term) to Z11 (the "spherical" term).

The analysis has been done considering the cases of a single DM, optically conjugated to ~15km, and two DMs optically conjugated to ~ 4km and ~15km.

Results are shown in Figure 1 where the RMS WFE is measured on grid of field points through the Monte Carlo trials. The distribution of these values is plotted on the right.

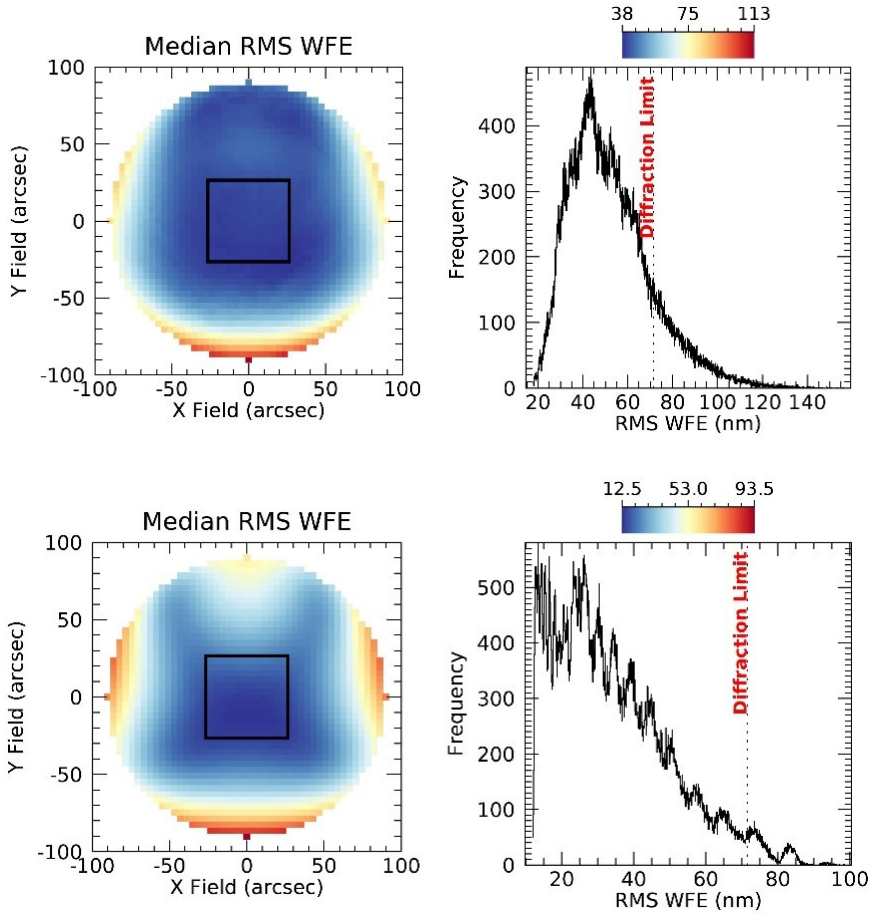

Figure 61: Black square is the MICADO 53"x53" FoV. Left: 2D RMS WFE map of median values given by the Monte Carlo trials that simulate system misalignments. Right: distribution of values given by the Monte Carlo trials considering a grid of field points. The first row shows the impact of alignment errors to the RMS WFE. The second row shows the results after a single DM correction.

A single DM is able to recover the nominal RMS WFE reported in Section 6.6. Two DMs perform better and even improve the nominal optical quality. In both cases the geometric distortion requirements are within the specifications.

The DMs strokes, necessary to achieve these results, are shown in Figure 62 in terms of Zernike coefficients. The defocus term (Z4) requires the biggest dynamical range and, in terms of Peak-to-Valley Surface Sag, is ≈ (2√3) Z4.

Coma and higher order term are very close to zero.

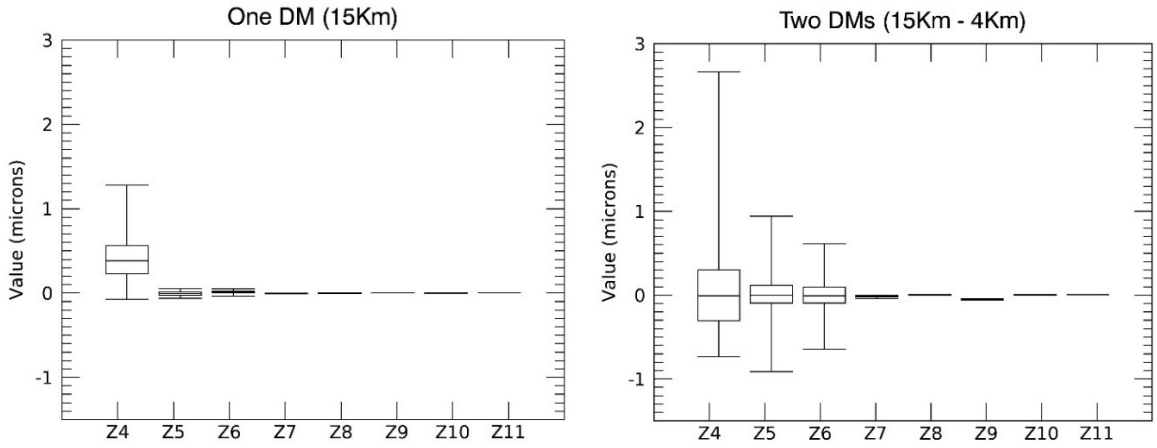

Figure 62: Distributions of Zernike coefficients used to correct the system misalignments. Box plots show minimum and maximum values and quartiles of each Zernike term distribution among the Monte Carlo trials. Left: Single DM considered. Right: Two DMs considered

7.3 MAORY-MICADO optical alignment

This Section describes the concept of MICADO-MAORY alignment at telescope site.

The same procedure is foreseen at the beginning of MAORY PFR alignment since it will materialize the optical axis of the system. This axis has to be coincident with the rotation axis of a dummy de-rotator which simulates the MICADO field de-rotator.

The idea is to use TT adjustment by MAORY M11 mirror and centring adjustment by MICADO with the assumption that the MAORY NGS WFS module is pre-assembled and aligned to MICADO cryostat/de-rotator.

Two mechanical references are used to achieve the alignment:

1. Entrance port references to materialise telescope optical axis. This is also the MAORY global coordinate system
2. Exit port mechanical axis of MICADO field de-rotator

The main tools used to perform the alignment are:

- Laser beam
- Commercial lenses

- Beam splitter
- Corner cube
- Test camera
- Reference flat mirror with cross-mark or other target on it.

The most confident approach is to materialize the de-rotator mechanical axis thanks to the laser beam. The flat mirror is implemented as a reference inside the de-rotator bearing and equipped with TT regulations.

A beam expander and a variable diaphragm allow, respectively, to adjust collimation and to select a small central portion of the laser beam to minimize aberrations. Referring to Figure 66, the beam splitter separates the light into the corner cube and the MAORY PFR direction. The beam coming from the reference mirror and the corner cube are re-combined and reflected into the lenses and test camera. The lenses role is to produce an imaging system for 2 configurations:

1. TT correction (focused to infinity)
2. Decentering correction (focused to plane of reference mirror with cross-mark)

The first phase of the alignment is leveling MICADO field de-rotator with respect to gravity and mount the reference flat mirror. With the camera in the first configuration, the corner cube reflects the incident laser beam in the same direction and produce a spot which is stationary during the field rotation. The reference mirror, if not properly co-planar with MICADO field de-rotator, produces a spot with elliptical trajectory whose axes are proportional to the mirror inclination respect to the rotation axis (see left Figure 63).

In this configuration, by adjusting the reference mirror TT, it is possible to detect a stationary spot when the mirror surface is perpendicular with the rotation axis. Then, by acting on the TT correction of MAORY M11, it is possible to overlap the two spots. One reflected back by the reference mirror and the other (which is stationary) reflected back by the corner cube. Now, the optical axis of MAORY is perpendicular with MICADO field de-rotator plane.

Switching to the second configuration of the camera, it is possible to adjust lateral centering of laser beam to centre it on cross-mark (see right Figure 63).

At this point, the MAORY PFR optical axis is defined.

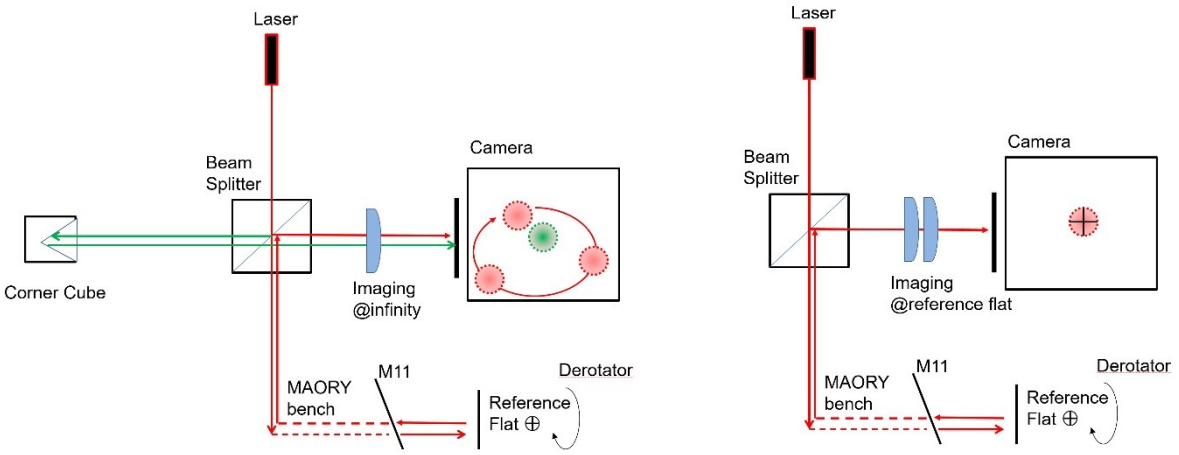

Figure 63: Left. First Camera configuration to remove spot rotation (adjust tip-tilt of reference flat) and to achieve the two spots overlapping (adjust TT of M11). Right. Second camera configuration to center cross-mark (move laser beam on MAORY bench)

7.4 MAORY Calibration Unit

A dedicated unit for calibration purposes is mandatory to simulate the ELT optical train in a 2 arcminutes FoV at Nasmyth focus of the Telescope where MAORY is planned to be placed.

During the instrument AIV phase, some tests with multiple simulated stars in the laboratory is necessary to ensure the MCAO performances, calibrations and test the required control software. A feasibility study has been done about a TS optical design that preserves the ELT optical parameters (focal ratio, exit pupil position and size, field curvature). The TS should emulate different atmospheric turbulence altitudes by means of two rotating PSs which generate realistic time varying aberrated WFs for various stars configurations. The TS should create a 2 arcminutes FoV beam as seen at the F/17.7 Nasmyth focus of the ELT where MAORY will be placed.

The goal of a TS is to simulate realistic ELT operation conditions in the laboratory by means of rotating transmitting plates set inside the instrument before the AS at the planes conjugated to the turbulent atmospheric layers.

The concept is to use an arbitrary finite number of visible-IR single mode fibers as diffraction limited point sources and submit phase disturbances to their WFs similar to the foreseen atmospheric ones, in terms of equivalent structure function and geometry of the ELT. In order to minimizing the complexity of the system, the studied optical design neglects the reproduction of LGS cone effect and perspective elongation which otherwise would have required a dedicated optical channel for each source [43], increasing the number of

components and the assembly/alignment of the optics. The strategy is to use an all reflective solution because of its chromatic correction over broad spectral ranges and to keep the instrument as compact as possible. MAORY uses a dichroic to split the science light channel from the LGS beams that are focused on the WFS by means of an objective. Due to the variation of the mean distance of the LGS from the telescope and the differential laser launcher jitter, the LGS objective has to compensate for these effects and could work up to infinite conjugate focal plane. The TS uses this unrealistic but still valid configuration to test the LGS WFS performances missing all the features regarding sodium layer thickness and finite distance. At the MAORY entrance focal plane, the images position, field curvature, exit pupil position and size are preserved.

The system design shall mainly consist of point sources, a collimated space where the PSs and a pupil mask can be situated, and a focal plane. The parameters scaling with respect to the ELT of the turbulent layers altitudes and off-axis sources chief ray angle are calculated by means of the following formulas:

$$1)\quad \alpha = \tan^{-1}\left(\frac{D}{d}\tan A\right)$$

$$2)\quad h = \frac{\tan A}{\tan \alpha}\frac{d}{D}H$$

where *D, A, H* are respectively the diameter, ray chief angle and turbulence layer altitude relative to the ELT while *d, α, h* are respectively the diameter, ray chief angle and turbulence layer altitude relative to the TS. Equation (1) implies optics with a large FoV to simulate the new generation of extremely large telescopes by means of relatively small built-in laboratory systems.

Considering the already build PSs [44] [45] [46], the simulated atmospheric turbulence achieves a range of Fried's parameters r_o of about 0.15 - 0.9mm at $\lambda = 500nm$. In the ELT case with r_o≈15cm the ratio D/r_o is ≈ 260 leading to a scaled AS size less then ≈ 250mm for a TS. Following a trade-off between optical quality, system compactness and numbers of optical surfaces, the AS has been chosen to have a diameter $\cong 200mm$. Historically, TMA [20] and four-mirror anastigmat (4MA) [47] designs have been the best systems for high-quality, wide FoV, all-reflective optical system. Most of them are relayed optics and, since we need an intermediate telescope pupil to be created by collimated light beams of point sources, these multi-mirrors unobscured systems are a possible starting point design for our

purposes. Besides, the MAORY input focal plane has a diameter of about 600mm requiring an unfeasible big monolithic lens in the case of refractive optics. The concept of the TS is shown in Figure 64 while Figure 65 shows a solid view of its optical design where the mirrors are arranged in power as +/+/-/+. The first mirror collimates the beams for the proper footprint on the PSs. The footprint diameters are set by a real AS followed by a second group of mirrors that focuses the disturbed WF on the MAORY input focal plane.

TS relevant optical parameters shall comply with the values given in the Table below.

Table 17 : TS main optical parameters

Parameter	**Value**
Focal ratio	≈ 17.7
Field curvature radius	≈ 9884 mm (concave)
Exit pupil distance	≈ 37868 mm (before the focal plane)
Exit pupil diameter	≈ 2134 mm
Minimum focal plane diameter	≈ 600 mm

The design considers 12 field points symmetrically set on a spherical surface (convex toward the first mirror). The most off-axis source is 168mm away from the center and simulates a NGS\LGS source on 60 arcsec FoV angular radius. Each source is collimated by an on-axis conical mirror which reflect the beams through the AS and the following PS with the correct chief ray angle respect to the optical axis. The re-imaging optics is a non-relayed TMA which delivers diffraction limited size images on the entire FoV considering a wavelength greater than 0.8µm. Given an AS of $d \cong 200mm$, the TMA has to cover a circular FoV of about 6.5º of angular diameter and generate a pupil magnification of about 10.6. The spot blur on the DM conjugation altitude is < 1/10 of actuator pitch, considering 29mm as distance between actuator centres (see Section 5).

The TS is required to have at least two PSs optically conjugate with the MAORY DMs whose optical conjugation is at 4km and 15.5Km altitude. Special attention has to be taken when selecting the beam footprints and the size of the PSs. In order to keep the differential speed, due to rotation, as small as possible, the footprint diameter has to be small compared to that of the PS. However, large PSs are difficult to manufacture and the established fabrication technique showed successful results with diameters up to 20cm [48]. In our case, for a fixed

reproduced turbulence, the PSs should have a diameter of about 60cm to keep the differential speed smaller than ±50%, revealing to be a critical component of the system. An alternative solution, keeping the PSs diameter within 20cm, is to use their mechanical structure to reproduce the pupil obscuration mask as projected onto the AS and scaled respect to the E-ELT case. Thus, the rotational axis of the PSs emulates the central obscuration and it is sustained by radial six-fold symmetrical obscuration which emulates the telescope spiders. The width of each spider leg shall be not greater than ~2mm at the AS while the central obscuration is required to be no greater than ~ 4.3 cm. Finally, to overcome the differential speed disturbance, the reproduced turbulence shall increase toward the PS centre (e.g. smaller Fried parameter).

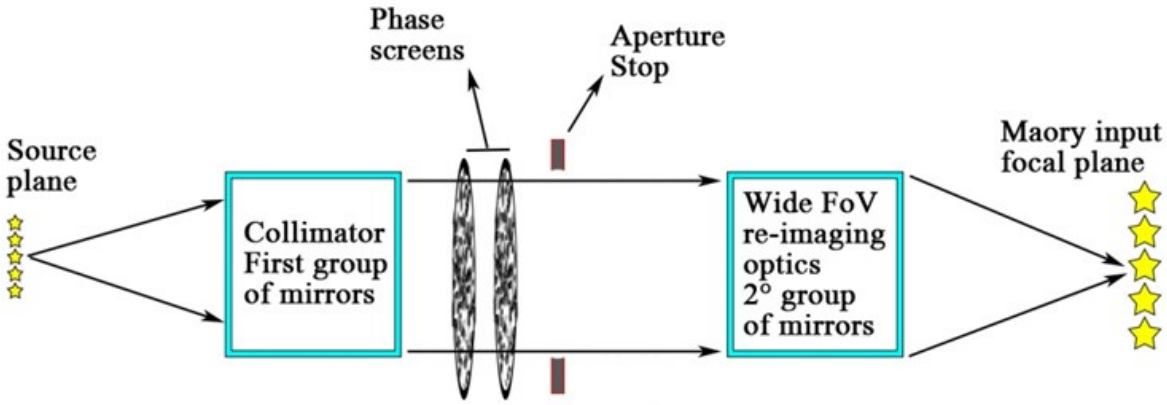

Figure 64 : TS concept. The sources are simulated by optical fibers (4µm core). The PSs are placed where the source rays have been collimated with the proper chief ray angle. The MAORY input focal plane has a diameter of ≈520mm, thus a certain magnification is expected.

Table 18 : TS optical features

	Aperture	**Diameter (mm)**	**Shape**
Mirror 1	Concave	610	Prolate ellipsoid
Mirror 2	Concave	340	Hyperboloid (off-axis)
Mirror 3	Convex	350	Hyperboloid (off-axis)
Mirror 4	Concave	620	Prolate ellipsoid (off-axis)

The presented design of a full MCAO TS could be the simpler in terms of compactness, number of elements and diffraction limited optics able to simulate the parameters of an extremely large class telescope. The overall dimensions (5.2m x 1.6m x 0.7m) of this TS are still huge for a built-in laboratory system but a smaller design would require more optical elements increasing the cost and complexity. The monolithic design, respect to a dedicated optical channel, lost the possibility to simulate the LGS features but reduced the complexity of the system making even simpler its future alignment and integration. Since such a tool for MAORY calibrations and tests would be unsuitable in terms of cost and risks, a simpler solution is to get rid of a TS and directly use an ELT focal plane simulator by accurately placing the sources at the MAORY entrance focal plane.

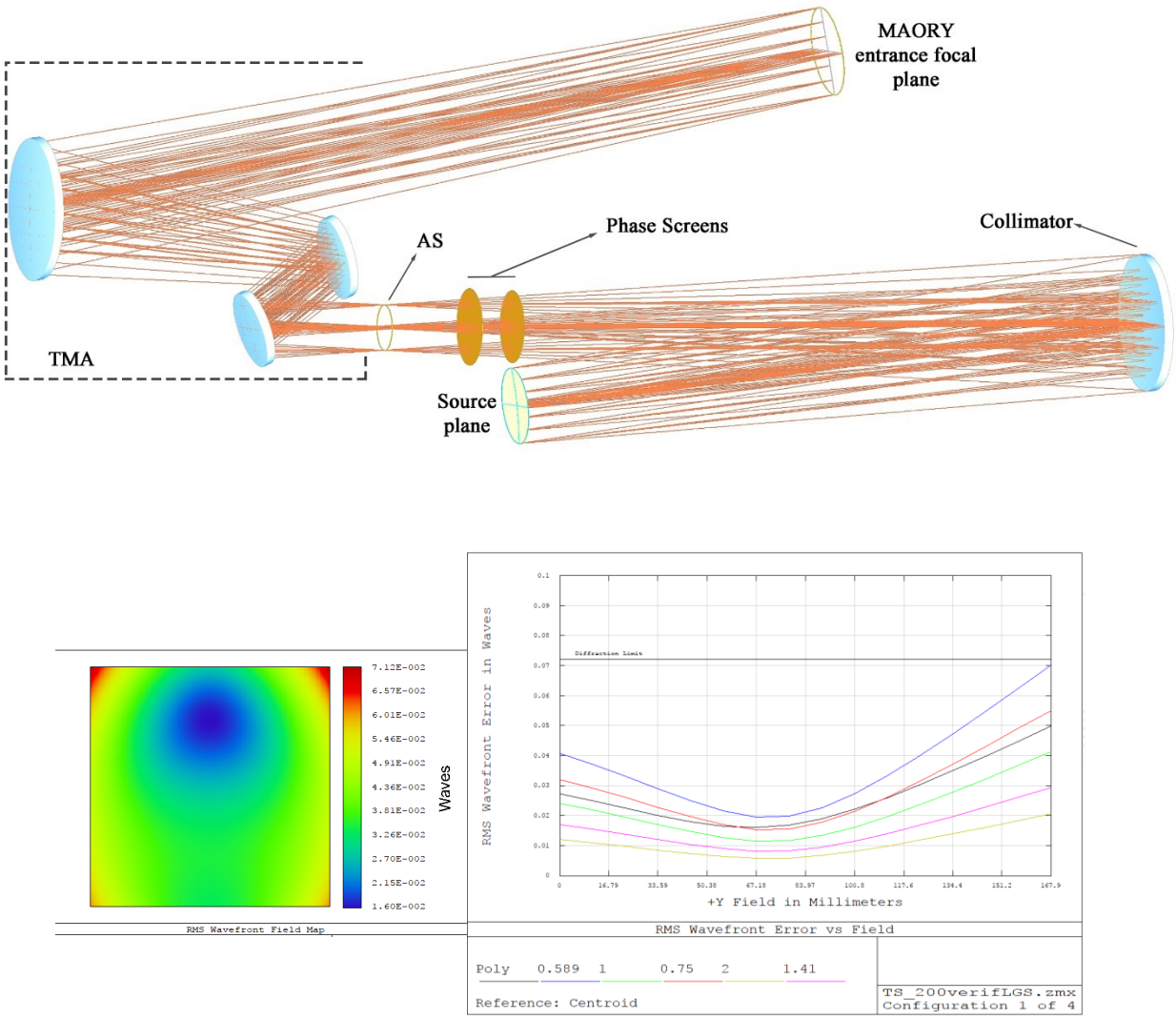

Figure 65 : (Up row) TS optical design. (Bottom row) RMS WFE field map and RMS WFE vs sources position.

Collecting all the information from analysis studies presented in this Chapter, a preliminary list of basic CU characteristics can be derived.

The CU has to allow the system alignment as discussed in the Section 7. In addition, it has to provide all the feasible and necessary tools to system calibrations. At the time of writing, a complete definition of the calibration plan is still under discussion.

Calibration modes. WFS and astrometric modes. WFS modes include calibrations regarding NGS and LGS WFS, DMs calibrations and NCPA. The entire MAORY FoV is used to measure the WFE, to calibrate the WFSs and DMs, while the circle containing the MICADO FoV is used to measure and calibrate optical distortions.

Operational wavelength. 0.6 to 2.4 μm. This matches the operating range for the NGS WFSs and that for the science camera of MICADO.

NGS point source type. Resolved and unresolved. (i.e. seeing limited and diffraction limited broadband NGS sources). The diffraction limited sources will be used to measure low-order Zernike terms as well as for various WFS registration and calibration tasks (i.e. DM to lenslet registration). The resolved sources will be used for calibrations where the source size is a critical factor such as centroid gain measurements.

LGS point source type. Unresolved at wavelength of ≈ 589,2 nm. They differ from NGS sources in terms of numbers and locations

NGS Point source numbers and locations. At least 20 sources of which 17 unresolved. The alignment simulations demonstrate that 9 unresolved (diffraction-limited) sources are enough to align the main path optics but WFS calibrations usually require resolved sources as well.

Seeing limited sources are placed in the NGS FoV. At least 3 resolved sources for calibrations where the source size is a critical factor for the NGS WFSs. At the edge of the NGS FoV, at least 8 unresolved sources are placed in a circle. The same applies at the edge of the MICADO FoV and a single unresolved source is on axis. A larger number of sources across the entire FoV is not excluded to be able to test a range of NGS configurations.

The sources at the MAORY entrance focal plane, are mounted at fixed locations across the field. They can be generated by single-mode optical fibers with ≈ 4 μm core for the unresolved sources and multi-mode optical fibers with ≈ 400 μm core to provide seeing limited sources.

This pattern should be able to rotate (at least in the range of ± 2.6º) to access more field points and to test geometric distortion. A trade-off study of a such focal plane mask for the MAORY CU has been done considering 4 different cases of what the mask is able to reproduce:

1. Flat mask – telecentric rays (Exit pupil at infinity)
2. Flat mask – ELT exit pupil (≈ 37,8 m)
3. Curved mask – telecentric rays (Exit pupil at infinity)
4. Curved mask – ELT exit pupil (≈ 37,8 m)

The analysis of the 4 designs showed that cases 1 and 3 are optically excluded because a different exit pupil position respect to the ELT will cause a change in DM conjugates and a certain amount of vignetting in the NGS FoV. Designs 2 and 4 mainly differ in terms of WFE since a flat mask introduce a field curvature aberration. They produce same results when testing optical distortions as defined in Section 5.1.

To exactly reproduce the ELT focal plane, the optical fibers must be fixed with a proper chief ray angle in order to reproduce the ELT exit pupil position. The surface connecting the fibers must be spherical with a curvature radius of 9,88 m. Figure 66 shows a conceptual layout for the sources in the image plane.

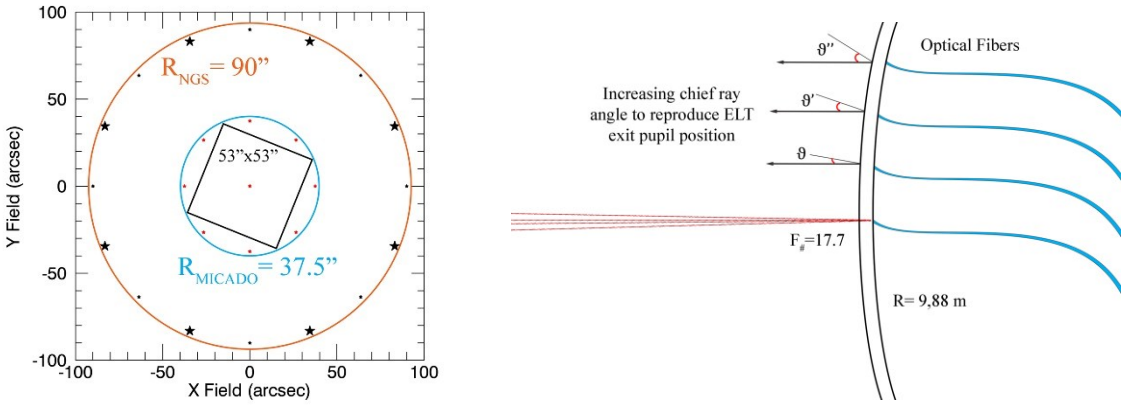

Figure 66 : Conceptual layout for the sources at the MAORY entrance focal plate to exactly reproduce the ELT focal plane.

LGS Point source numbers and locations. The six LGSs ‘seeing-limited’ sources are placed in a hexagon configuration to simulate the LGS constellation. The same mask concept has to be used for the LGS sources. The LGS Objective is designed to deliver LGS images in the altitude range 80 - 240 km. The ELT focal plane conjugate at 240 km is about 2 meters after the MAORY entrance focal plane (inside the MAORY bench) and this position increases as the LGS altitude decreases. Besides, the F-number and chief ray angle of an imaged LGS source changes as well as its altitude (See Figure 67).

If the CU has to deliver calibration modes considering at least two LGS altitudes, then two solutions could be adopted:

1. Two masks placed at different positions on the MAORY bench.
2. A single mask with a doubled number of sources for LGS that can move along the MAORY optical axis.

Light diffusers could be used during the AIV operations to align each probe with the LGS Objective. The light diffuser diameter has to be large enough to cover the WFS FoV allowing to detect a WFS flat field.

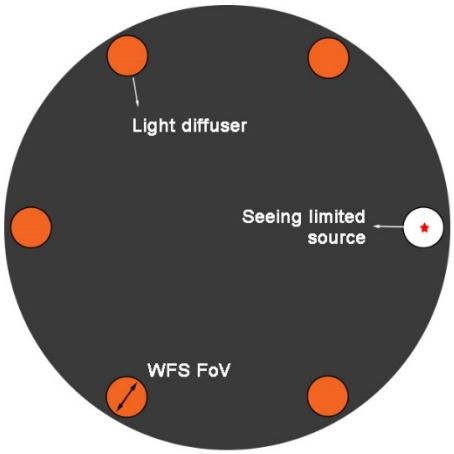

	Chief ray angle (deg)	F#
240 Km conjugate	**0.6**	**16.88**
80 Km conjugate	**0.52**	**15.38**

Figure 67: LGS mask conceptual layout. Chief ray angle and F-number to reproduce the ELT focal plane w.r.t. LGS altitudes

The LGS WFS alignment is made by centring the LGS WFS probes. That means the rotation axis of the probes has to be coincident with the LGS Objective FoV centre.

If a single probe is not centred to its respective LGS Objective image, some of the SH-WFS sub-aperture will vignette. Translational DOF are used to obtain a uniform and unvignetted illumination of the SH-WFS.

This operation must be repeated for each probe and for different rotation angles of the LGS WFS Sub-System.

Once the rotational axis is aligned to the LGS Objective FoV centre, the diffusers mask has to be removed and a fine-tuning alignment of the probes could be done by using the SH-WFSs. Any Tip-Tilt and defocus signal can be compensated by the probe hexapods.

8. Conclusions

At the present stage of the MAORY project phase B, the optical design is compliant with the requirements.

The Prototype experiment of LGS WFS has been important to have a precise idea, based on real data, on the low order modes inherent to the sodium profile shape and variation. The support given to the MAORY numerical simulation code has been essential and the results have confirmed the chosen design of the NGS Reference WFS as supplement to the LGS WFS.

The presented MAORY performances through tolerance analysis has been essential to define the opto-mechanical requirements to be used in the procurement process. The analysis results will be refined during the MAORY project phase C (e.g. relaxing some tolerances) considering also the preliminary cost breakdown provided by external companies.

The main path optics is expected to undergo very minor changes (e.g. FoV and thus, mirror diameters) in the final design phase while a major change could interest the LGS Objective. Its baseline design has been developed with a tight requirement on the residual quasi-static WFE. The main aspect to be considered, from the technical point of view, is the level of residual WFE and the effectiveness of the calibration procedures to remove it from the LGS measurements. If larger WFE is confirmed to be acceptable, the design could be simplified, allowing significant cost reduction and possible easier AIV procedures. A trade-off between two designs is in progress.

The alignment method, presented for the main path optics, is independent from the optical design and it is a powerful tool to reduce the amount of time allocated to some activities during the AIV phase.

The raytracing simulations that have been run to validate the alignment method, have a crucial role to define the minimum requirements on the geometry and number of sources for the calibration unit.

Calibration and AIV plans are under definition. The design studies of the ELT turbulence simulator demonstrate that such a tool for MAORY calibrations and tests would be unsuitable in terms of cost and risks. This is the main reason to choose a focal plane mask as hardware for AIV and calibration activities.

9. Bibliography

[1] R. K. Tyson e B. W. Frazier, Field guide to adaptive optics, vol. 2, SPIE Press, 2004.

[2] A. N. Kolmogorov, «A refinement of previous hypotheses concerning the local structure of turbulence in a viscous incompressible fluid at high Reynolds number,» *Journal of Fluid Mechanics,* vol. 13, pp. 82-85, 1962.

[3] E. F. Bradley, R. A. Antonia e A. J. Chambers, «Turbulence Reynolds number and the turbulent kinetic energy balance in the atmospheric surface layer,» *Boundary-Layer Meteorology,* vol. 21, pp. 183-197, 1981.

[4] F. Roddier, «V the effects of atmospheric turbulence in optical astronomy,» *Progress in optics,* vol. 19, pp. 281-376, 1981.

[5] J. W. Hardy, Adaptive optics for astronomical telescopes, vol. 16, Oxford University Press on Demand, 1998.

[6] D. L. Fried, «Limiting resolution looking down through the atmosphere,» *JOSA,* vol. 56, pp. 1380-1384, 1966.

[7] H. W. Babcock, «The possibility of compensating astronomical seeing,» *Publications of the Astronomical Society of the Pacific,* vol. 65, pp. 229-236, 1953.

[8] B. C. Platt e R. Shack, «History and principles of Shack-Hartmann wavefront sensing,» *Journal of Refractive Surgery,* vol. 17, pp. S573--S577, 2001.

[9] R. Ragazzoni, «Pupil plane wavefront sensing with an oscillating prism,» *Journal of modern optics,* vol. 43, pp. 289-293, 1996.

[10] F. Roddier, «Curvature sensing and compensation: a new concept in adaptive optics,» *Applied Optics,* vol. 27, pp. 1223-1225, 1988.

[11] J. M. Beckers, «Adaptive optics for astronomy: principles, performance, and applications,» *Annual review of astronomy and astrophysics,* vol. 31, pp. 13-62, 1993.

[12] S. Esposito, A. Riccardi, L. Fini, A. T. Puglisi, E. Pinna, M. Xompero, R. Briguglio, F. Quirós-Pacheco, P. Stefanini, J. C. Guerra e others, «First light AO (FLAO) system for

LBT: final integration, acceptance test in Europe, and preliminary on-sky commissioning results,» in *SPIE Astronomical Telescopes+ Instrumentation*, 2010.

[13] E. Pinna, F. Pedichini, S. Esposito, M. Centrone, A. Puglisi, J. Farinato, L. Carbonaro, G. Agapito, M. Stangalini, A. Riccardi e others, «XAO at LBT: current performances in the visible and upcoming upgrade,» in *Adaptive Optics for Extremely Large Telescopes 4--Conference Proceedings*, 2015.

[14] V. P. Bailey, L. A. Poyneer, B. A. Macintosh, D. Savransky, J. J. Wang, D. a. R. J. Rosa, K. B. Follette, S. M. Ammons, T. Hayward, P. Ingraham e others, «Status and performance of the Gemini Planet Imager adaptive optics system,» in *SPIE Astronomical Telescopes+ Instrumentation*, 2016.

[15] P. L. Wizinowich, D. S. Acton, O. Lai, J. Gathright, W. Lupton, P. J. Stomski e others, «Performance of the WM Keck observatory natural guide star adaptive optic facility: The first year at the telescope,» in *proc. SPIE*, 2000.

[16] R. Foy e A. Labeyrie, «Feasibility of adaptive telescope with laser probe,» *Astronomy and Astrophysics,* vol. 152, pp. L29--L31, 1985.

[17] J. M. Beckers, «Increasing the size of the isoplanatic patch with multiconjugate adaptive optics,» in *European Southern Observatory Conference and Workshop Proceedings*, 1988.

[18] E. Diolaiti e others, «MAORY: a multi-conjugate adaptive optics relay for the E-ELT,» *The Messenger,* vol. 140, pp. 28-29, 2010.

[19] R. Gilmozzi e J. Spyromilio, «The 42m european elt: status,» in *SPIE Astronomical Telescopes+Instrumentation*, 2008.

[20] L. G. Cook, *Three mirror anastigmatic optical system,* Google Patents, 1981.

[21] ESO, *E-ELT OPTICS, https://www.eso.org/sci/facilities/eelt/telescope/mirrors/,* 2017.

[22] R. Davies e M. I. C. A. D. O. Team, «MICADO: the E-ELT adaptive optics imaging camera,» *arXiv preprint arXiv:1005.5009,* 2010.

[23] S. Esposito, G. Agapito, J. Antichi, A. Bonanno, L. Carbonaro, C. Giordano e P. Spano, «NGS WFSs module for MAORY at E-ELT,» *Memorie della Societa Astronomica Italiana,* vol. 86, p. 446, 2015.

[24] F. Vidal, E. Gendron, Y. Clénet, D. Gratadour, G. Rousset e R. Davies, «Adaptive optics simulations for the MICADO SCAO system,» in *SPIE Astronomical Telescopes+ Instrumentation*, 2014.

[25] F. Rigaut e E. Gendron, «Laser guide star in adaptive optics-The tilt determination problem,» *Astronomy and Astrophysics,* vol. 261, pp. 677-684, 1992.

[26] J. Drummond, J. Telle, C. Denman, P. Hillman, G. Moore, S. Novotny, R. Fugate e M. Eichoff, «Sodium guidestar radiometry results from the SORś 50W fasor,» in *The Advanced Maui Optical and Space Surveillance Technologies Conference*, 2006.

[27] N. Ageorges e C. Dainty, Laser guide star adaptive optics for astronomy, vol. 551, Springer Science & Business Media, 2013.

[28] T. Pfrommer e P. Hickson, «High-resolution mesospheric sodium observations for extremely large telescopes,» in *SPIE Astronomical Telescopes+ Instrumentation*, 2010.

[29] R. J. Noll, «Zernike polynomials and atmospheric turbulence,» *JOsA,* vol. 66, pp. 207-211, 1976.

[30] L. Schreiber, E. Diolaiti, C. Arcidiacono, T. Pfrommer, R. Holzlöhner, M. Lombini e P. Hickson, «Impact of sodium layer variations on the performance of the E-ELT MCAO module,» in *SPIE Astronomical Telescopes+ Instrumentation*, 2014.

[31] M. Lombini, G. Bregoli, G. Cosentino, L. Schreiber, E. Diolaiti e I. Foppiani, «Prototype of a laser guide stars wavefront sensor for E-ELT: design and integration,» in *SPIE Astronomical Telescopes+ Instrumentation*, 2010.

[32] M. Patti, M. Lombini, L. Schreiber, G. Bregoli, C. Arcidiacono, G. Cosentino, E. Diolaiti e I. Foppiani, «Laboratory prototype for the demonstration of sodium laser guide star wavefront sensing on the E-ELT,» *Memorie della Societa Astronomica Italiana,* vol. 86, p. 441, 2015.

[33] M. Patti, L. Schreiber, C. Arcidiacono, G. Bregoli, P. Ciliegi, E. Diolaiti, S. Esposito, P. Feautrier e M. Lombini, «Accurate laser guide star wavefront sensor simulation for the E-ELT first light adaptive optics module,» in *SPIE Astronomical Telescopes+ Instrumentation*, 2016.

[34] T. Fusco, M. Nicolle, G. Rousset, V. Michau, J.-L. Beuzit e D. Mouillet, «Optimization of a Shack-Hartmann-based wavefront sensor for XAO systems,» in *Proceedings of SPIE*, 2004.

[35] L. Schreiber, M. Lombini, E. Diolaiti, C. Robert, I. Foppiani, G. Cosentino, G. Bregoli e E. Marchetti, «The laser guide stars wavefront sensor prototype for the E-ELT: test results,» in *Proc. SPIE*, 2010.

[36] C. Arcidiacono, L. Schreiber, G. Bregoli, E. Diolaiti, I. Foppiani, G. Cosentino, M. Lombini, R. C. Butler e P. Ciliegi, «End to end numerical simulations of the MAORY multiconjugate adaptive optics system,» in *SPIE Astronomical Telescopes+ Instrumentation*, 2014.

[37] C. Arcidiacono, L. Schreiber, G. Bregoli, E. Diolaiti, I. Foppiani, G. Agapito, A. Puglisi, M. Xompero, S. Oberti, G. Cosentino e others, «The numerical simulation tool for the MAORY multiconjugate adaptive optics system,» in *SPIE Astronomical Telescopes+ Instrumentation*, 2016.

[38] L. Schreiber, E. Diolaiti, C. Arcidiacono, A. Baruffolo, G. Bregoli, E. Cascone, G. Cosentino, S. Esposito, C. Felini, I. Foppiani e others, «Dimensioning the MAORY real time computer,» in *This Proc. SPIE*, 2016.

[39] S. J. Thomas, D. Gavel e R. Kibrick, «Analysis of on-sky sodium profile data from Lick Observatory,» *Applied optics,* vol. 49, pp. 394-402, 2010.

[40] M. Lombini, A. De Rosa, P. Ciliegi, F. Cortecchia, E. Diolaiti, M. Patti, M. Bonaglia, L. Busoni, V. De Caprio, S. Esposito e others, «Optical design of the post-focal relay of MAORY,» in *SPIE Astronomical Telescopes+ Instrumentation*, 2016.

[41] B. Neichel, F. Rigaut, A. Serio, G. Arriagada, M. Boccas, C. dÓrgeville, V. Fesquet, C. Trujillo, W. N. Rambold, R. L. Galvez e others, «Science readiness of the Gemini MCAO system: GeMS,» in *SPIE Astronomical Telescopes+ Instrumentation*, 2012.

[42] H. N. Chapman e D. W. Sweeney, «A rigorous method for compensation selection and alignment of microlithographic optical systems,» in *Proc. SPIE*, 1998.

[43] M. Lombini, E. Diolaiti, C. Arcidiacono, G. Bregoli, G. Cosentino, A. De Rosa, I. Foppiani e L. Schreiber, «Optical design of MAORY turbulence simulator,» in *Proceedings of the Third AO4ELT Conference*, 2013.

[44] S. Hippler, F. Hormuth, D. J. Butler, W. Brandner e T. Henning, «Atmosphere-like turbulence generation with surface-etched phase-screens,» *Optics express,* vol. 14, pp. 10139-10148, 2006.

[45] T. A. Rhoadarmer e J. R. P. Angel, «Low-cost, broadband static phase plate for generating atmosphericlike turbulence,» *Applied optics,* vol. 40, pp. 2946-2955, 2001.

[46] S. Thomas, «A simple turbulence simulator for adaptive optics,» in *Proc. of SPIE Vol*, 2004.

[47] L. G. Cook, *Compact four-mirror anastigmat telescope,* Google Patents, 2004.

[48] R. Rampy, D. Gavel, D. Dillon e S. Thomas, «Production of phase screens for simulation of atmospheric turbulence,» *Applied optics,* vol. 51, pp. 8769-8778, 2012.

[49] L. Schreiber, I. Foppiani, C. Robert, E. Diolaiti, J.-M. Conan e M. Lombini, «Laser guide stars for extremely large telescopes: efficient Shack--Hartmann wavefront sensor design using the weighted centre-of-gravity algorithm,» *Monthly Notices of the Royal Astronomical Society,* vol. 396, pp. 1513-1521, 2009.